

Research on Collision Safety for Self-Driving and Electric Cars

メタデータ	言語: eng 出版者: 公開日: 2018-07-31 キーワード (Ja): キーワード (En): 作成者: YANG, YANG メールアドレス: 所属:
URL	http://hdl.handle.net/10291/19581

明治大学大学院先端数理科学研究科
2017 年度
博士学位論文

Research on Collision Safety for Self-Driving and Electric Cars

自動運転車と電気自動車の衝突安全に関する研究

学位請求者 現象数理学専攻

楊 陽

Research on Collision Safety for Self-Driving and Electric Cars

自動運転車と電気自動車の衝突安全に関する研究

A Dissertation

Submitted to the Graduate School of Advanced Mathematical Sciences

Meiji University

by

Yang Yang

Supervisor: Professor Dr. Kokichi Sugihara

January 2018

Abstract

With the concern of environment issues and the rapid development of artificial intelligence (AI) technology, conventional fossil fuel vehicles will gradually lose the market-leading position, and electric vehicles, self-driving vehicles, and self-driving electric vehicles are taking over. No matter how the vehicle's mechanical control or body structure changes, the vehicle safety is always a top concern for users. A common design approach to enhance the crashworthiness of a vehicle is to make the energy absorption device absorb kinetic energy as much as possible for improving the safety of the driver or passengers when a crash occurs. This approach is also considered to be applied for the energy absorption structure's development in daily necessities. Another approach to enhance the vehicle safety is to prevent collision by judging the driver's status through driver's facial expression based on AI technology when the situation of driver is bad for driving.

Firstly, the absorbing-energy structure is designed by using origami engineering. Imagine if the mechanical power transmission systems are removed from the front of electric vehicles, the floor structure is weak for absorbing crash energy, and against this background, space filling core panel is applied to the development of the vehicle floor structure because of the high stiffness. On the other hand, if the existing box-type section structure is still used as energy absorption device, because its box-type section is hollow, it is easy to bending, though it has ideal collapse mode without Euler buckling, it cannot be collapsed more than 70% of its length because of its bulk and its initial peak load is sometimes too high. Two pairing origami structures are compared to apply to absorbing-energy structure. In the study process, the mathematical geometry model is developed to express origami structure for structural parameterization. The response surface methodology (RSM) as an optimization method is utilized to improve the structural optimization of achieving the goal of maximization crash absorption energy. The dynamic finite element method (FEM) simulation is used to analyze the crash mechanical characteristics of origami structure. The resulting collision characteristics of the proposed origami structure are compared with the existing structure or widely used structure to review the superiority of the proposed origami structure.

Secondly, as a feedback of the vehicle collision researches, the origami engineering is applied to a daily necessity safety helmet, because the safety helmet attempt to protect the user's head by absorbing mechanical energy as much as possible which is similar to the energy absorption

device of vehicle. The safety helmet structure is designed by using origami structures based on the experience gained from vehicle structural design method. Considering the storage space and the Ministry of Health, Labor and Welfare (MHLW) helmet standards, three origami structures: accordion cover, reversed spiral cylindrical (RSC) and origami-honeycomb are introduced to the structural design and the low-priced energy absorption material corrugated cardboard is proposed as the helmet material. The impact FEM analyses are done to investigate the mechanical characteristics of the designed origami safety helmet and the numerical analysis results are compared with the experimental results. As a result, the designed origami safety helmet satisfies the goals of being saved in a small box and meeting the safety helmet standards.

Finally, from another perspective to view the collision safety for vehicles, ADAS is also important part for helping and early warning driver. In it, the driver monitoring system (DMS) is to monitor driver attentiveness. The deep learning convolutional neural network (CNN) technology is utilized to replace the facial feature points extraction in the driver's facial recognition. The image data augmentation is used to increase image data for improving the accuracy of facial expression recognition.

Acknowledgements

This dissertation has received zealous support and cooperation of many people. I am like to express my best sincerely respect and honorable thanks.

Foremost, I would like to express my sincere gratitude to my advisor Professor Ichiro Hagiwara for the continuous support of my PhD study and research, for his patience, motivation, enthusiasm, and immense knowledge. His guidance helped me in all the time of research and writing of this thesis.

Besides my advisor, I would like to thank my thesis committee: Professor Kokichi Sugihara, Professor Kazuyuki Nakamura and Professor Xilu Zhao, for their encouragement, insightful comments. And I am grateful to all MIMS members for their kind assistance and MIMS for their financial support throughout my PhD years.

Moreover, I would like to give thanks for people in Hagiwara laboratory; Doctor Maria Savchenko and Professor Chie Nara who gave me guidance and suggestions to my research; Doctor Thai Thao, Doctor Sunao Tokura, Associate Professor Sachiko Ishida, Xiaoshi Chen, Aya Abe and Yuko Adachi who all supported me for many fruitful discussions; Emiko Kuroda, Tomoko Ichikawa and Eri Nakayama who gave me support for my daily life with my limit Japanese.

Last but not least, I express my gratitude to my parents, my husband, and all other family member for their support and understanding. I would like to give my special thanks to my son Orange, who is giving me energy all the time, which made me refresh and concentrate on my research. I was not able to complete my PhD dissertation without them.

Contents

Chapter 1 Introduction	1
1.1 Background.....	1
1.1.1 Energy-absorbing structures	1
1.1.2 Origami engineering	4
1.1.3 Collision avoidance system	10
1.2 Previous collision researches and problem statement	11
1.3 The goal of the thesis	15
1.4 Structure of the thesis.....	16
Chapter 2 Crash energy absorbing members of the lightweight electrical vehicles by using truss core panel.....	17
2.1 The proposal of TCP structure	18
2.2 Crash analysis of the structure based on TCP	20
2.3 Study on the improvement of crash energy absorption	23
2.3.1 Optimum design method	23
2.3.2 Model's settings of optimization	33
2.3.3 Optimized result	34
2.4 Comparison results between the proposed structure on TCP and the structure based on HCP	36
2.5 A study on the optimal structure based on TCP	41
2.6 Summary	44
Chapter 3 Crash energy absorbing members of the electrical vehicles by using pairing origami structure.....	45
3.1 Pairing origami structures	45
3.2 Impact analysis by finite element method (FEM)	51
3.2.1 Analysis method	51
3.2.2 Simulation method.....	52
3.3 Optimization of the structure geometry.....	53

3.3.1	The relationship between configuration and parameters in NP	54
3.3.2	The relationship between configuration and parameters in TMP	56
3.4	Optimization results and discussion	58
3.5	Comparison with the existing rectangular cross section structure and RSC structure	63
3.6	Summary	63
Chapter 4	Application of vehicle crash technology and origami structures to daily necessities	64
4.1	Previous researches	64
4.2	Newly developed safety foldable helmet	67
4.2.1	The origami structure of the cover part	67
4.2.2	The origami structure of the reverse spiral cylindrical structure (RSC)	69
4.2.3	The origami structure of honeycomb	71
4.3	Numerical simulation for helmet	72
4.3.1	Analysis method of impact	72
4.3.2	Model's setting of optimization	76
4.3.3	Characteristic discussions of proposed helmet based on optimal RSC structure	77
4.4	Experimental results	80
4.5	Summary	85
Chapter 5	Preventive safety for the self-driving vehicles by deep learning	87
5.1	Self-driving vehicles and convolutional neural network	87
5.2	Analysis method of facial expression recognition	91
5.2.1	Analysis system	91
5.2.2	Analysis database	92
5.2.3	Analysis method of data augmentation	93
5.2.4	Learning convergence time	95
5.3	Analysis results	95
5.4	Summary	97
Chapter 6	Conclusions and future works	98
6.1	Conclusions	98
6.2	Future works	100
6.2.1	Improvement of the foldable safety helmet	100
6.2.2	Improvement of the image recognition for automatic driving	102

Bibliography	105
<i>Chapter 1</i>	105
<i>Chapter 2</i>	112
<i>Chapter 3</i>	113
<i>Chapter 4</i>	114
<i>Chapter 5</i>	115
<i>Chapter 6</i>	117

Chapter 1 Introduction

Global warming is primarily a problem of too much carbon dioxide (CO₂) in atmosphere, and about 15% of manmade carbon dioxide comes from cars. Electric cars, which burn no gasoline and have no tailpipe emissions, hold a lot of promise for a healthy environment. As the effects of global warming become more of a concern to people, the use of these cars could become more popular in the years ahead. On the other hand, over 90% of all car accidents are due to human error. With the development of science technology and artificial intelligence technology, self-driving cars, which only a few year ago was still considered science fiction, is beginning to sweep the automotive industry, not only because of saving life from safety points, but also because of saving time/fuel/space etc. from comfortability points. Moreover, due to the regulatory reasons, namely gas mileage requirements and engineering reasons – electric cars are easier for computers to drive, a self-driving car likely be an eclectic one. Nevertheless, the collision energy absorption characteristics is extremely important for the realization of the self-driving cars and the electric cars.

1.1 Background

1.1.1 Energy-absorbing structures

The energy absorption behaviors of structures play a critical role in the safety of the structures after collision. In aerospace, cars, highway fence and other practical engineering, due to the needs of security measure, the designers are very strict with the energy absorption performance of structures. In the packaging designs of electronic products or valuables, the packaging structures should be considered that they can absorb enough energy to reduce the damage to the packaging object in the case of impacting or falling. In addition, in the field of human protection

and sports safety, it also has similar problems.

Since the 1970s, people have come to realize the importance of structural energy absorption and have done a lot of researches. Now, a large number of research results have been used in practice.

Used to improve cars' crashworthiness. According to a recent survey, more than 75% collision accidents are frontal collisions, which are the most common accident form comparing with the side collision, so the safety performance at frontal collision is one of the most important tasks in vehicle design development.

The most important task of vehicle design development is that the crushed buckling deformation of the vehicle member absorbs the crush energy as much as possible. And the front side members installed on the both sides of the front of vehicles as shown in Figure.1.1 are the most important vehicle members for energy absorption in collision to protect driver and passengers.

Used for highway fence. In order to reduce the damage caused by vehicle collisions, various types of hardware have been developed to install along the highway. When a vehicle collides with the fence system installed alongside a highway, the kinetic energy of the vehicle is dissipated mostly on the deformation of the W-beam and the pillar as shown in Figure.1.2, which reduces the severity of the accident, as well as saves more lives.

Used for personal safety. Various auxiliary protective devices, such as safety helmets, bicycle helmets and bulletproof vests as shown in Figure.1.3, are required to have high energy absorption capacity. The earthquakes occur frequently in recent years and bring not only great financial loss, but also the death and the injury. In the earthquakes, the helmet plays an important role in protecting the head of people. The bicycle helmet is another example; it protects the user's head when user falls from the bicycle and the head collides with the road.

In the game and sports, such as American football, boxing, skiing, horse racing and auto racing, energy absorption for crashworthiness is also very important, so the energy-absorbing structures are applied for human body.

Used for packaging. Packaging as an important way to preserve and distribute goods has become an indispensable part of our lives. One of the basic functions of packaging of course is to protect the goods from external damage caused by transportation and storage. For example, during stem cell transportation, it needs to protect it from damage and to consider some conditions, such as sterility assurance, temperature maintenance and so on. One cell packaging box is shown in Figure.1.4.

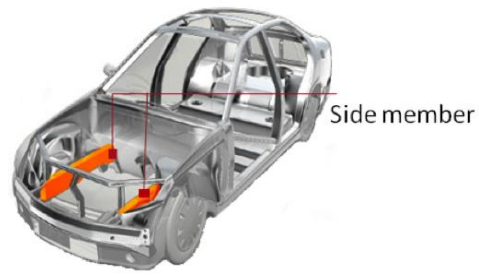


Figure.1.1 The collision structure of car.



Figure.1.2 The W-beam and the pillar structures of highway fence.



Figure.1.3 The structures of safety devices.

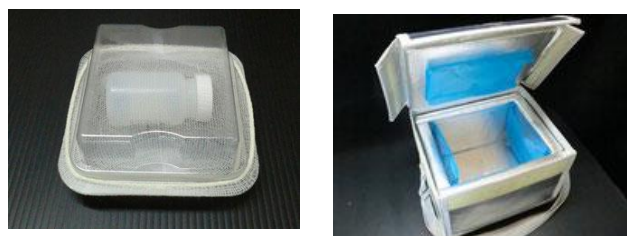


Figure.1.4 The shockproof structures of packaging.

1.1.2 Origami engineering

Origami is an art of paper folding that transforms a flat sheet of paper into various shapes. The development of paper art has a long history. When the paper was really made, paper art was born along with the progress of human civilization. The paper art is generally believed to originate from China, however, Japanese really carried it forward. In 1797, Japanese priest Ichien Gido published “Hidden Senbazuru Orikata” which is the first known book on origami and recorded a large number of origami patterns (shown in Figure.1.5) that were known at that time. After the 1920’s, people started to realize that origami has its technical complexity, the scientific application and the research values. The Japanese origamist Akira Yoshizawa was considered to be the grandmaster of origami and he widely popularized paper art into the Japanese name “origami” [1.1]. By the 1980’s, people had begun to notice that origami can be studied as a mathematical problem. Ultimately, once an origami is expanded, it is a number of folds on a sheet of paper that satisfy certain mathematical properties. In the 1990’s, American scientist Robert Lang wrote a program called “treemaker”, which allows people to input any shape, and figures out the crease pattern for the shape [1.2].

In the 2002, Taketoshi Nojima proposed the scientific study of the techniques of origami as origami engineering. In the 2003, Ichiro Hagiwara advanced origami engineering and launched a research group on origami engineering in the Japan Society for Industrial and Applied Mathematics [1.3]. Until now, origami is to be developed from a simple art into the engineering. Origami structures have roughly 2 kinds of properties. One property is foldable and deployable function, and another is the function to strengthen the structure. These properties have attracted many attentions of scientists, researchers and engineers. The present researches of origami engineering and industrial applications are mentioned as below.

Folding/unfolding mechanism. Inspired by the grow movements of physical phenomena and plate shapes in nature, many origami pattern are developed. For example, from simulating the spiral shapes of plant as shown in Figure.1.6 (a), Nojima et al. designed many kinds of physical origami model as shown in Figure.1.6 (b). Figure.1.6 (c) shows the corresponding fold origami pattern [1.4]. Ishida et al. created the developed pattern for foldable structures by mathematical approach based on those spiral models [1.5]. Saito investigated the unfolding/folding mechanism of ladybug wings as shown in Figure.1.7 (a), and the studies shew that the origami-like crease patterns as shown in Figure.1.7 (b) on the wings play an important role in the folding process [1.6]. A wide range of applications have been coming into sight because origami has this folding/unfolding feature that is able to produce 3D shape from a flat sheet. For example, a designer in Japan created clothes hinted from animation based on

Nojima’s origami [1.7] as shown in Figure.1.8. Even in the daily life, origami structures are applied for beer/cafe can or jewelry displace as shown in Figure.1.9 and so on.

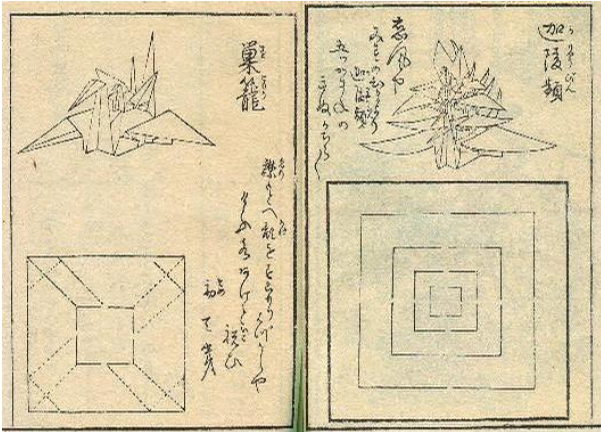


Figure.1.5 An origami pattern in book “Hidden Senbazuru Orikata”.

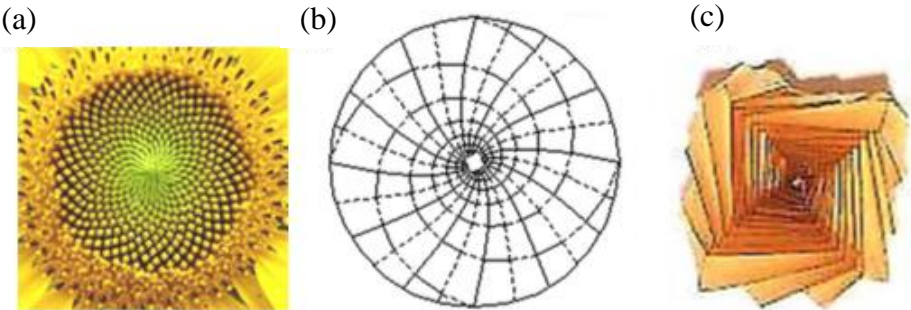


Figure.1.6 The relationship between flower shape and origami model [1.4].

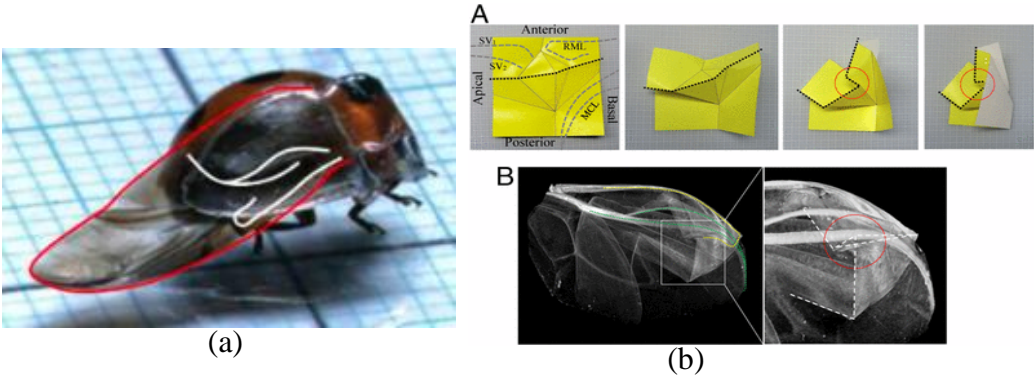


Figure.1.7 The relationship between ladybug wing and origami model [1.6].

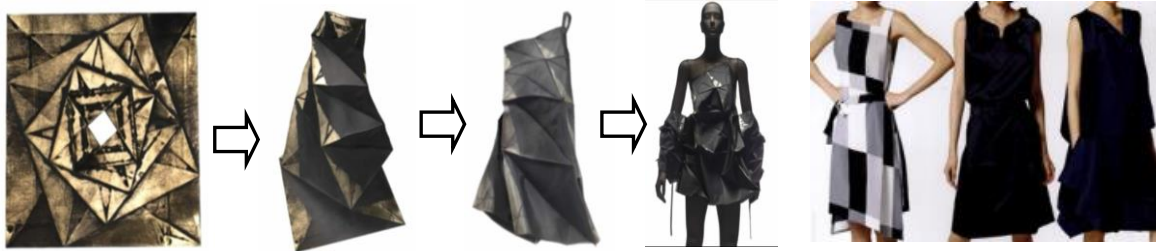
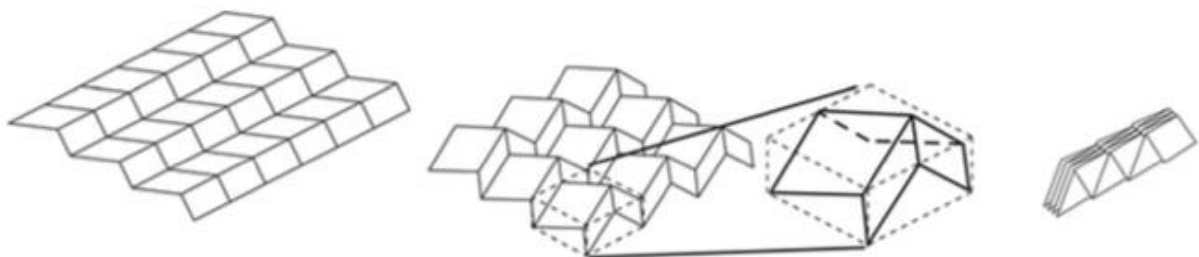


Figure.1.8 Fashion clothes designed from origami.



Figure.1.9 Origami structures used in daily life.



(a) Unfolded or developed state (b) Partially-folded state and repeated unit (c) Flat-folded state

Figure.1.10 The folding sequence of a Miura pattern [1.9,1.10].



Figure.1.11 A map designed by rigid miura-ori pattern.

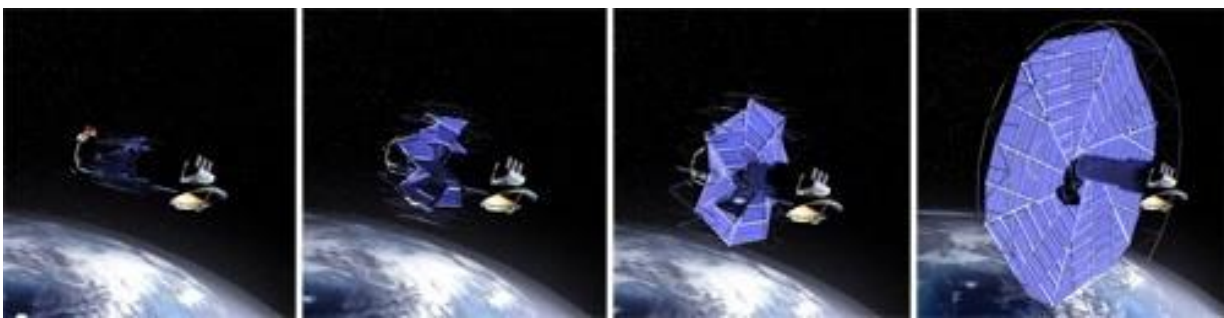


Figure.1.12 Rigid miura-ori pattern used for solar panel.

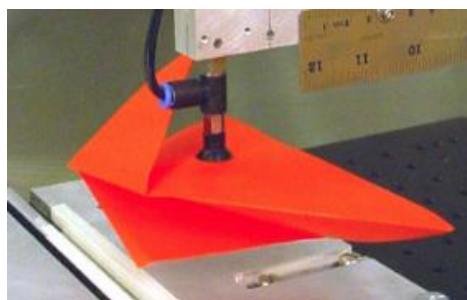


Figure.1.13 The first origami robot.

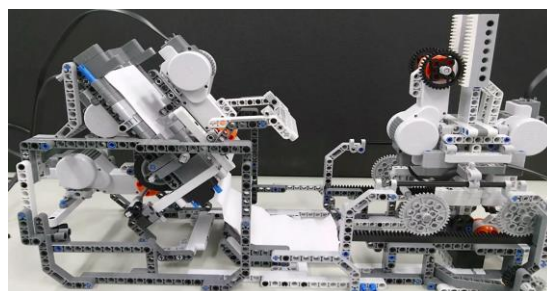


Figure.1.14 Folding machine.

Rigid origami pattern. Rigid folding is a branch of origami for which foldability is kept even when its faces and crease lines are replaced by rigid panels and hinges. Therefore, the folding process of the rigid origami pattern is, in fact, the motion of mechanisms. The Miura pattern is a fundamental rigid pattern [1.8] that is commonly used for engineering, architectural, and design applications as shown in Figure.1.10 [1.8,1.10]. This provides a one-DOF mechanism from a developed state to a flat-folded state. To explore novel deployable origami structures with rigid pattern and simple motion, intensive research has been carried out in the field of rigid origami. Hull expanded that a flat foldable single-vertex pattern was also rigidly foldable or not judged by spherical trigonometry [1.11]. Sreinu et al. investigated that the single-vertex rigid origami was linked to spherical polygonal linkages, and some single-vertex origami could be rigidly folded into other configurations continuously by spherical motions [1.12]. Belestro et al. proposed a matrix method for modelling origami configurations initially folded from flat [1.13]. Tachi developed a variety of cylindrical deployable structures with rigid quadrilateral panels [1.14,1.15]. Wang et al. proposed a mobile assembly of spherical 4R linkages to study the Kokotsakis type of the rigid origami patterns [1.16].

The study of rigid origami is not only a mathematical challenge, but also behind many real engineering applications. The rigidly foldable Miura-Ori pattern has been used to a map which can be unfolded in one action and refolded with minimal hassle as shown in Figure.1.11. as far as astronautical engineering through the construction of solar panels used by NASA as shown in Figure.1.12. A first origami folding robot was designed to fold some simple rigid origami patterns [1.17] as shown in Figure.1.13 and one folding machine, which is similar to printer machine, can create the fold's scratches in a sheet of paper [1.18] as shown in Figure.1.14. A temporary tent is developed from the prismatic structures [1.19] as shown in Figure.1.15. These examples have demonstrated the great potentials of rigid origami in a wide range of fields. A rigid origami stent as shown in Figure.1.16 is used to enlarge clogged arteries and veins. To facilitate more applications, more properties of rigid origami need to be further investigated.

Thickness origami. Mathematically, origami panels are generally assumed to be planar with zero thickness. Having thickness in the material has disabled some fundamentals of origami in rigid origami. The techniques for thickness accommodation in origami-inspired mechanism design are studied. For example, origami models can be viewed as kinematic mechanisms where folds are revolute joints and panels are links. The origami-inspired mechanism can achieve the same kinematic motion as the paper origami source model. Trautz et al. carried out that the hinge translations occurred, when the structure with the thickness [1.20]. Guest et al. presented a modeling technique for wrapping thin membranes around a central hub [1.21]. Moreover, some innovative applications of thickness origami have been appearing. Nara et al.

developed a flat-foldable box of thick panels by using the Benette linkage [1.22] as shown in Figure.1.17. Tachi gave a realized example design of constant thickness rigid origami composed of quadrilateral panels [1.23] is shown in Figure.1.18.



Figure.1.15 The origami tents [1.19].

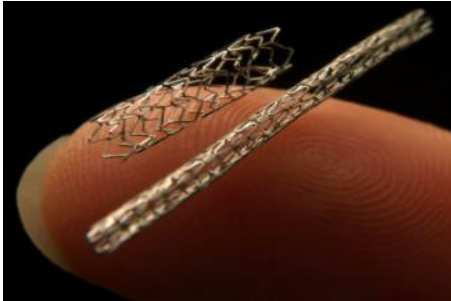


Figure.1.16 The origami stent.



Figure.1.17 A model of a box with thickness which was made of cardboard.

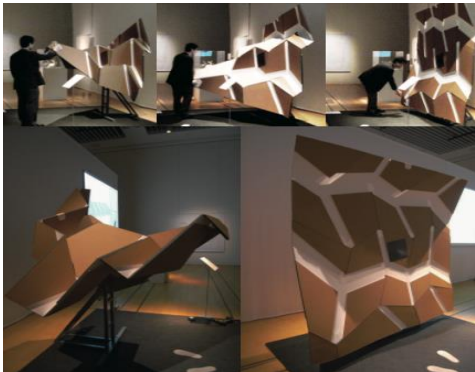


Figure.1.18 An design of rigid foldable origami materialized with cloth and cardboards [1.23].

1.1.3 Collision avoidance system

Self-driving cars could dramatically reduce the traffic accidents, which effectively avoid crash accidents, so self-driving cars have the potential to improve safety and increase quality of life. Advanced Driver Assistance System (ADAS) technology have helped to bring self-driving cars to the forefront of public interest and discussion recently. ADAS includes many functions that enable a safer driving environment for drivers, passengers and pedestrians. Some safety related to ADAS applications already generally used in self-driving car are enumerated as following. Besides, there are many other ADAS applications or will be used in self-driving car.

Adaptive cruise control (ACC). An automatic control of adjusting the speed to maintain a safe distance from the car ahead based on sensor information as shown in Figure.1.19. The information is provided by a combination of sensors, radar and computer-connected cameras [1.25]. This technology has been widely used regarding as a key component of self-driving car.

Automatic parking (AP). An automatic control of moving the car from a traffic lane into a parking spot as shown in Figure.1.20. This technology uses a variety of sensors to determine the approximate size of the parking space [1.26].

Forward collision avoidance (FCA). An automatic control of warning drivers to reduce the severity of a collision by using radars, lasers, cameras and GPS sensors to detect an imminent crash as shown in Figure.1.21. Collision avoidance by braking is appropriate at low vehicle speeds, while collision avoidance by steering is appropriate at higher vehicle speeds [1.27].

Driver monitoring system (DMS). An automatic control of monitoring driver's driving statuses and warning the driver under abnormal driving conditions by catching driver's face situation as shown in Figure.1.22. This technology is to alert the driver when signs of drowsiness or distraction are detected.



Figure.1.19 Schematic sample of ACC [1.25].

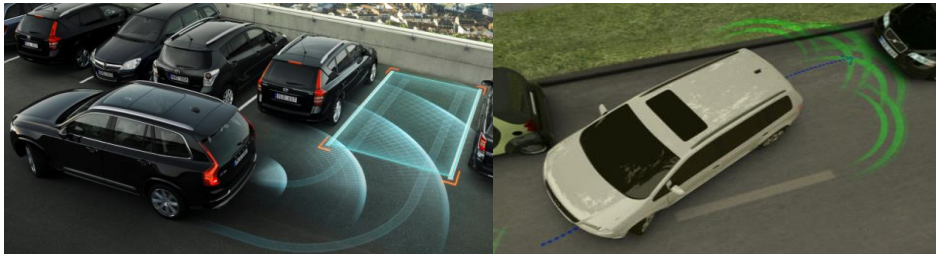


Figure.1.20 Schematic sample of AP.

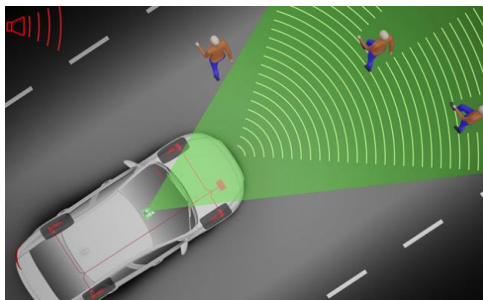


Figure.1.21 Schematic sample of FCA.

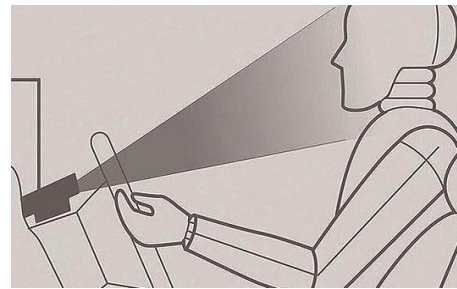


Figure.1.22 Schematic sample of DMS.

1.2 Previous collision researches and problem statement

Studying the behaviors of energy-absorbing structures usually starts with quasi-static analysis and testing. Yamashita et al., Ujibashi et al. and Kim et al studied the characteristics, such as buckling mode, crush load and energy-absorbing, of a strength member through the falling weight type impact testing [1.28~1.32]. These research results provided important basic data and technology for the energy-absorbing structure designs of vehicles.

In the 1970's, a crash analysis model called "Mass-Spring" was developed in accordance with the collision safety standard established by Federal Motor-Vehicle Safety Standard (FMVSS) [1.33~1.34]. In this model, the part which doesn't deform was modeled as the mass, and energy-absorbing part was modeled as the spring. After about ten years, the collision researches have been centered on the "Mass-Spring" model analysis. In addition, the beam model based on the finite element method (FEM) and finite difference method (FDM) was continuing to be used for the collision analysis.

From the latter half of 1980's, the collision analysis was popularly studied by shell FEM

method instead of “Mass-Spring” and beam. Hagiwara and Kitagawa et al. studied the collision analysis of thin-walled columns with arbitrary section geometry by using FEM [1.35~1.36]. In these studies, the collapse deformation process was summarized in four deformation steps -wall buckling, corner stress concentration, ridge section yield, next wall buckling (as shown in Figure.1.23), and accordion-like crush deformation mechanism was analyzed in detail by repeating these four steps [1.37~1.39]. Hagiwara et al, Y.Toi, W.Abramowicz, K.Mori, Yamashita and Yasai et al analyzed the crush characteristic of box-shape or polygonal cross section or tapered strength member respectively, and published many research results on crush deformation, load and energy absorption [1.40~1.49]. Takatori et al carried out detailed crush analysis by repeatedly changing the FEM models and discussed the influence on energy absorption from the vehicle members’ characteristics in detail [1.50~1.54]. Furthermore, Kitagawa et al used a sensitivity analysis method for dynamic nonlinear problem to discuss the buckling strength and structural response after changing design parameters and proposed an approach to decrease the maximum load which were important for energy absorption [1.55~1.56].

Since the latter half of the 1990’s, as an extension of collision simulation technology by FEM, optimization technology has been applied to the vehicle structural design and a number of research results have been published [1.57~1.61]. For example, Yamazaki and Han maximized the impact energy absorption of cylinders and prisms by changing some parameters like the cross section dimension, plate thickness, bending angle, etc. to obtain the optimal structure [1.62~1.66]. Yumingu et al., Tsuknazawa and Nakazato et al discussed the optimization problem of collision thin-walled structural members and published the topology and optimal shape results [1.67~1.69]. Moreover, Kashiwamura et al., and Yu et al. used the optimization methodology of the statistical response surface to discuss some multiobjective function issues such as shape optimization of structural members by controlling the buckling, multiobjective optimization of reinforcement members subjected to collision load, robustness optimization by statistical support system and so on [1.70~1.80].

On the other hand, while the academic research is promoting, the researches on application technology that improves the performance of vehicles by applying the research results directly to the design and development of actual vehicles are on the road. From the viewpoint of engineering, the design goal of the side member structure of the vehicle is to lengthen the collapsed length and maximize the energy absorption amount as much as possible without bending during the collision process. But for the currently used thin-walled rectangular cross-section side member structure, it is difficult to crush as designed due to some initial irregularities.

In order to solve this problem, Hagiwara et al. seek the buckling wave length of the strength member such as the side member as shown in Figure.1.23 and Figure.1.24, and put the beads into member at the mountain and valley nodes of buckling wave to ensure the strength member crushed in the accordion type shape as shown in Figure.1.25 [1.81~1.82]. This specification was adopted by not only automobile manufactures in Japan but also global automobile manufacturers. However, even using this specification, it is not easy to obtain a collapsed length more than 70% of the member's own length. Therefore, Hagiwara et al. and Zhao et al. applied the revered spiral cylinder (RSC) origami structure to the strength side member, and received a collapsed length more than 90% of the member's own length [1.83~1.90].

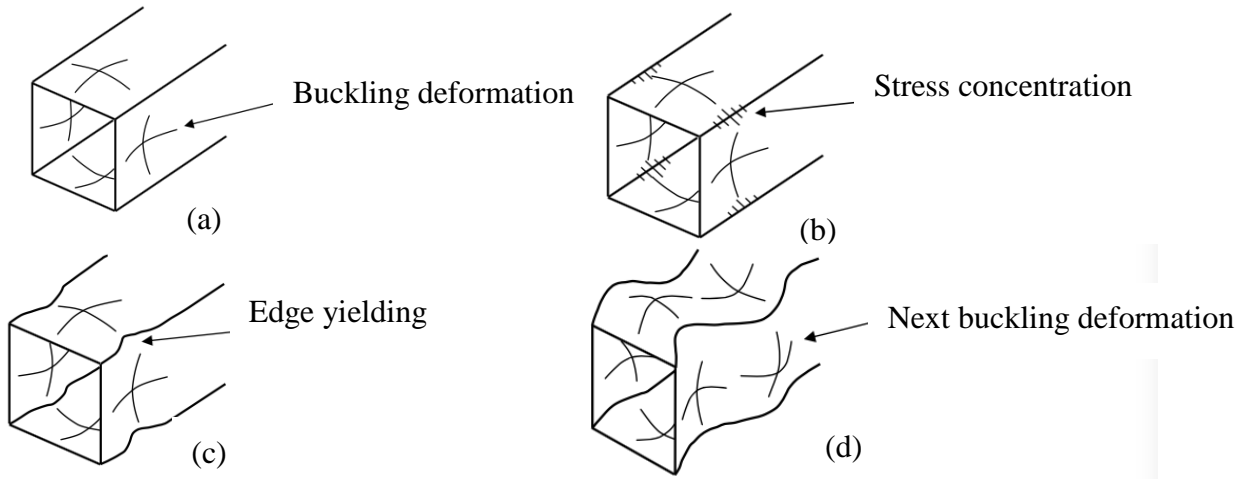


Figure.1.23 The collapse mode of side member.

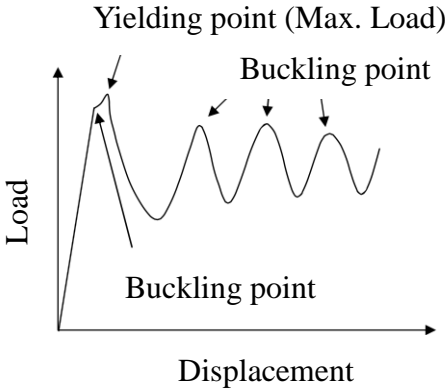


Figure.1.24 The load-displacement curve of the side member collapse mode.

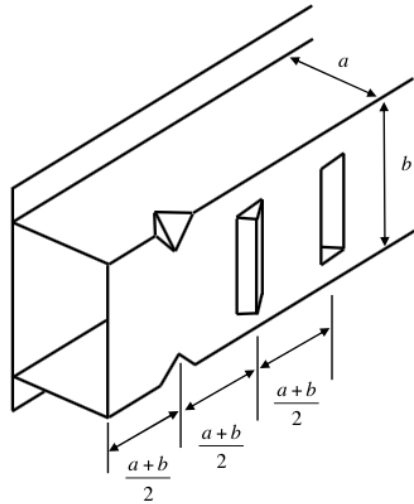


Figure.1.25 The pitch length of the collapse beading.

However, with the rapid development of electric vehicles and self-driving vehicles, the structure of the vehicle body has dramatic changed. Such changes in the structure of the vehicle body also affect the design method in the collision safety performance. So far there are no studies that apply the technology to the strength member fitting the body changes of electric vehicles and also no studies of using the origami structures to maximize their potential. So, it is a very promising research subject that a new type of the strength member with superior energy absorption efficiency by comprehensively utilizing the origami engineering, collision simulation and optimization design, even in the development of a commodity of safety helmet.

On the other hand, in the ADAS applications, many DMS have also been developed to reduce the chance of traffic crashes by grasping the driver's situation from the facial expression. However, traditional approaches require learning the facial expression through extracting and calculating the facial feature points, which is large consumption. So, it is a necessary research subject that before collision happened, the driver's statue recognition by more efficient method.

1.3 The goal of the thesis

3D origami structure inspired by origami engineering is thought to be used for energy-absorbing members, but it has not been studied sufficiently yet. As an energy-absorbing mechanism, for example, there are bellows-shaped structures, but it is not easy to control the crushing load, etc. In particular, in consideration of safety performance for body changes of electrical vehicles and self-driving vehicles, the collision characteristic of the energy-absorbing structure is unknown. And on the basis of studying the collision characteristics of electrical vehicles and self-driving vehicles and proposing new type energy-absorbing structures from origami engineering to be fit for the electrical vehicles and self-driving vehicles, a safety helmet, which requests energy-absorbing and peak force decrement same to the strength member of electrical vehicles and self-driving vehicles, is challenged to be invented also by using origami engineering and collision simulation. In addition, for the electrical vehicles and self-driving vehicles, the collision characteristic is studied not only from the design of the energy-absorbing structure but also from facial expression recognition of driver to recognize the driver's situation with deep learning technology.

The main goals of this thesis are the following three points.

(1) The energy-absorbing members are studied to increase the energy absorption and decrease the peak force as much as possible for the electrical vehicles and self-driving vehicles by combining origami engineering, collision simulation and structural optimization design technology.

(2) A new type of the foldable safety helmet is proposed by the design method established from the new designed energy-absorbing members of the electrical vehicles and self-driving vehicles.

(3) Except the improvement of collision performance the electrical vehicles and self-driving vehicles by proposed new energy-absorbing members, to avoid the collision caused from the driver attentiveness during the automatic operation of self-driving vehicles, it is necessary to catch driver's status. The status of driver can be grasped by driver's facial expression. The driver's facial expression is studied to be recognized by deep learning and the limited number of driver's facial expression image data is proposed to be increased by image augmentation methods of generating image translation and altering image intensity.

1.4 Structure of the thesis

This thesis is concerned with the modelling, analysis and simulation of collision characteristics, in addition, deep learning of facial expression recognition for the development of the electrical vehicles and self-driving vehicles. The structure of this thesis is divided into 6 chapters.

Chapter 1 is the introduction of existing energy-absorbing member, the origami engineering, and collision avoidance system. This chapter describes the current status and issues of related researches, and clarifies the goal of this thesis.

Chapter 2 presents a new energy-absorbing panel member of the electrical vehicles using lightweight structure truss core panel designed. The structural geometrical parameters are optimized by optimization methodology, and the energy absorption performance is discussed by collision simulation comparing with the common honeycomb panel structure.

Chapter 3 presents a new energy-absorbing cylinder member of the electrical vehicles using pairing origami structures. The structural geometrical characteristics of two pairing origami structures (Nojima polyhedron and Tachi-Miura polyhedron) are investigated to discuss the collision characteristics of energy absorption and peak force by simulation. Comparing with the existing rectangular cross section structure and reversed spiral cylindrical structure and taking the advantage of manufacture cost, the applications of the pairing origami structures are mentioned.

Chapter 4 presents a challenge to invent a foldable safety helmet by using origami structures borrowing ideas from the experience of energy-absorbing member design of vehicles. In this chapter, the proposed safety helmet structures are introduced, and numerical analysis results and experimental results are compared to discuss the irregularities in the experiments and the validity of the analysis model.

Chapter 5 is the extension investigation of collision characteristics of the self-driving vehicles from the viewpoint of the artificial intelligence. In the automatic level 2, automatic operation can switch from human operation when driver loses awareness suddenly. The driver's statue is effectively grasped from the driver's facial expression. In this chapter, the driver's facial expression is learned by deep learning method instead of the traditional machine learning method. And the image augmentation method is investigated to increase the limited number of driver's facial images.

Chapter 6 presents summarizing all the calculation and simulation results, contributions, and the future works.

Chapter 2 Crash energy absorbing members of the lightweight electrical vehicles by using truss core panel

The lightweight structures have been widely used for aircrafts, trains and vehicles because it is possible to reduce the materials usage, reduce the amount of gas and improve the fuel economy which are good for the environment in addition to their performance of stiffness and strength. Developing a lightweight structure, which meets performance requirements of strength, stiffness, vibration, and crash energy absorption is becoming a big research challenge [2.1~2.5].

On the hand, the truss core panel is a structure invented based on the research work of space filling feature for regular tetrahedrons and octahedrons at the same time because neither tetrahedrons nor octahedrons can fill up space without gaps by itself regardless of the simplicity in their shapes [2.6~2.10]. They have better aspects in bending stiffness and in shear strength. The relation between the geometrical pattern of truss core panel and mechanical characteristic was investigated. It was shown that geometrical parameters have obvious effected on the bending stiffness and on the in-plane shear strength [2.11]. The formability of truss core panel employing a simple press method of nonlinear analytical simulation and using multi-purpose dynamic analysis software LS-DYNA was confirmed [2.12]. Also the results of the core shape optimization to improve impact energy absorption ability of the truss core panel by using LS-DYNA were presented [2.13]. However, when the truss core panel structure receives an impact load from the lateral direction, the structure easily has longitudinal bending, so it is a major obstacle of using the structure based on the truss core panel structure as the collision strength member.

In order to solve this problem, we propose a new lightweight structure which consists of truss core panel (hereafter referred to as TCP) and reinforced part (hereafter, this part is called insert member) with optimized geometric parameters to seek the maximum crash energy absorption

amount under weight control condition. The geometric parameters of the structure based on honeycomb panel (hereafter referred to as HCP) was optimized also to verify the superiority of the proposed structure.

2.1 The proposal of TCP structure

The TCP structure applied in this study, is a combination of a flat plate and a triangular pyramid panel in which triangular pyramids are arranged in the form of staggered pattern. The top plate is linked to the vertices of cores in the TCP by spot welding method. The feature of this single TCP is shown in Figure.2.1. Figure.2.1 (a) shows the bottom surface of the TCP; Figure.2.1 (b) shows the top surface. As shown in Figure.2.2, when the single TCP collides against a rigid wall from the side direction, the structure is bent longitudinally due to the asymmetrical shape of the top/bottom surfaces, so it is difficult to apply the single TCP as a collision strength member alone.

Therefore, a lightweight panel structure based on TCP is proposed as shown in Figure.2.3 (a). The vertices of cores in the truss core panel are linked to the plate by spot welding method. Along the both sides, the truss core panel is joined to the insert members also by spot welding method.

The dimensions and shape parameters are set as shown in Figure.2.3 (b). The width of the proposed structure is 420mm; the length is 300mm; the width of the insert member on both sides is 15mm; the bottom side length of the core is 55mm. The crush energy absorption performance of the proposed structure is optimized using the dimensions and thickness shown in Figure.2.3 (b) as the design parameters.

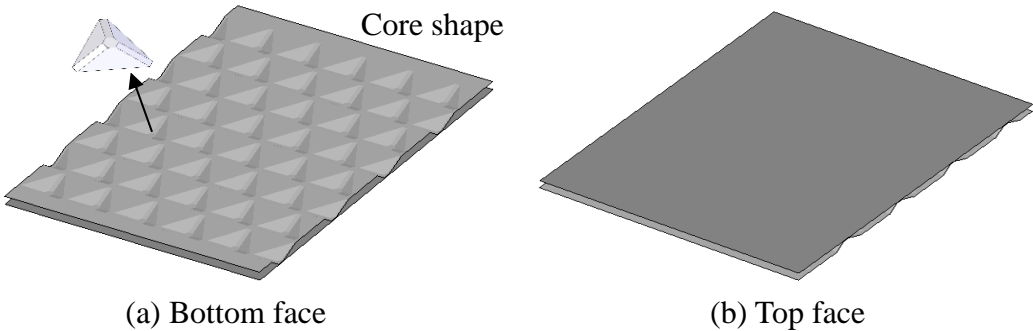


Figure.2.1 The single TCP consists of two parts.

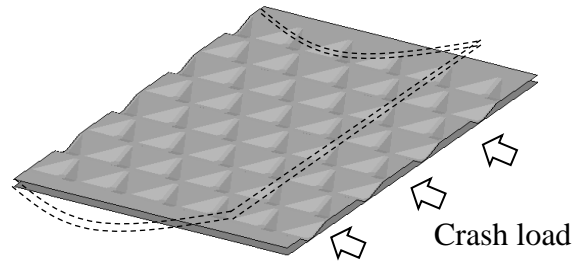


Figure.2.2 The dotted line shows the asymmetrical deformation of the single truss core panel structure after the structure is deformed by crash load.

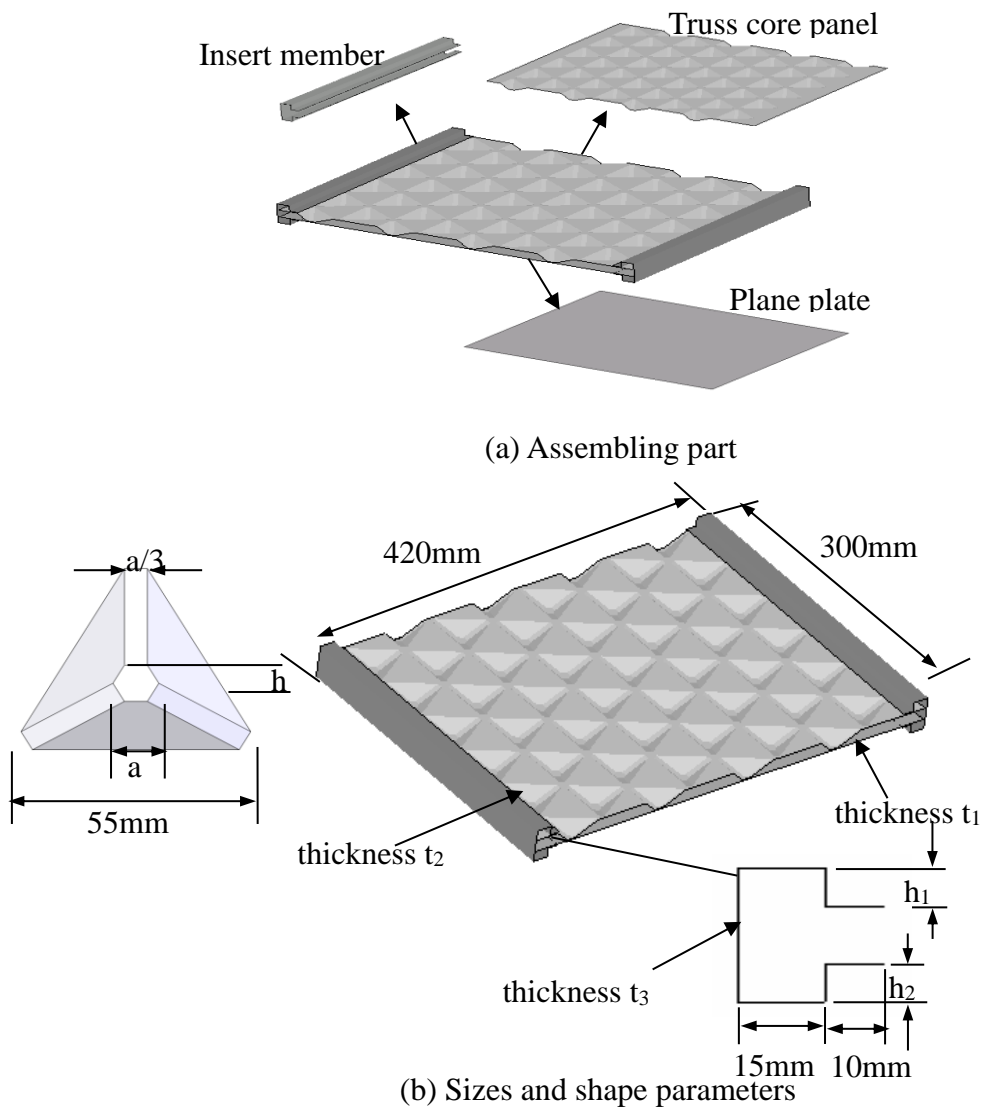


Figure.2.3 Proposed lightweight structure with TCP.

2.2 Crash analysis of the structure based on TCP

Figure.2.4 shows the crash analysis model, where the clamped boundary conditions were applied at the one end of the structure. The rigid wall impacts the structure with the initial velocity of 55km/h and the contact condition between structure and rigid wall is defined by “*AUTOMATIC_SURFACE_TO_SURFACE Command” in LS_DYNA. The structural model was meshed with quadrilateral elements. All the elements are modeled in a character size between 3 and 5mm. The number of elements is 25257, and the number of nodes is 25478.

The cores are connected to the plate and the side members by spot welding elements to build the contact condition of the nodes in each component respectively. Since the spot welding is considered to be significant influence on the crash energy absorption and be closer to the real thing, we set the spot welding modeling using a beam element and make it possible that the nodes (the spot welding points) of both ends of beam elements can be put on the arbitrary positions of the shell element sides as shown in Figure.2.5. Furthermore, because there is a possibility that the spot welding is broken in the actual impact, the rupture criterion is set to equivalent strain 0.3 according to the reference (<http://www.ncac.gwu.edu/>). The steel is used as a material in the simulation. Table.2.1 presents the material properties. And, the Cowper-Symonds equation (2.1) [2.14] is used for the strain rate sensitivity of material.

$$\sigma_y = \sigma_{y_0} \left[1 + \left(\frac{\dot{\epsilon}}{c} \right)^p \right]^{\frac{1}{p}} \quad (2.1)$$

Here, σ_y is the dynamic yield stress. σ_{y_0} is the static yield stress. $\dot{\epsilon}$ is strain rate. c and p is the constant inherent of material. And referring to the automobile crash analysis case in the actual (<http://www.ncac.gwu.edu/>), $c = 8000$ and $p = 8$.

Table.2.1 Material properties of the model.

Young's modulus	210 GPa
Poisson's ratio	0.3
Density	7.8×10^{-6} kg/mm ³
Yield stress	270 MPa

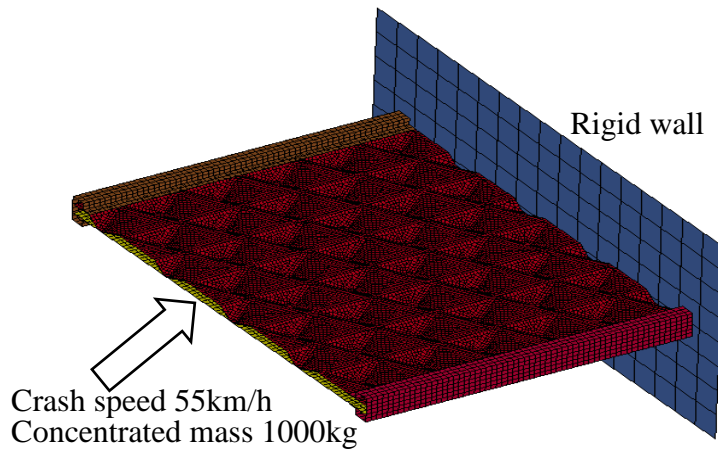


Figure.2.4 Crash analysis model of lightweight structure.

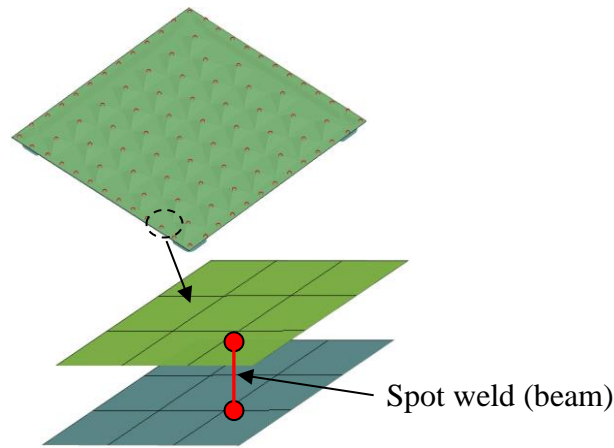


Figure.2.5 Definition of spot weld using beam element.

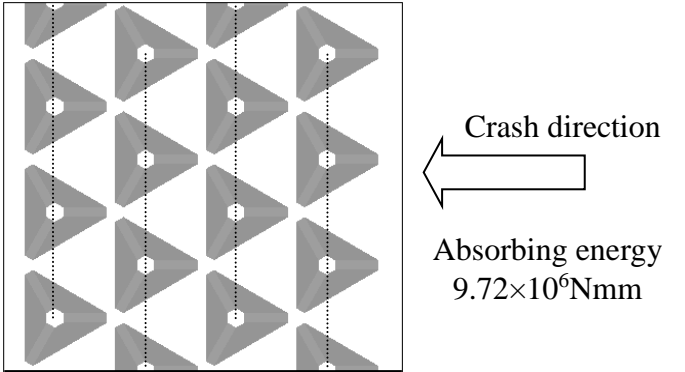
The strain energy of all the elements is obtained by the following equation for the evaluation of the crash energy absorbing performance of the structure:

$$E_{absorb} = \sum_{i=1}^N \int_V \sigma \epsilon dV \quad (2.2)$$

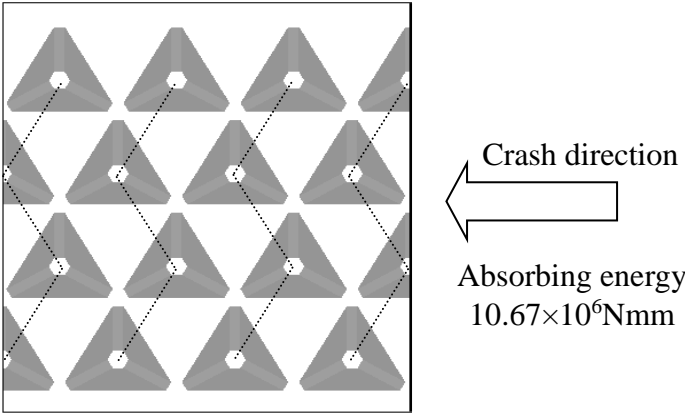
Where N is a number of elements.

The Figure.2.6 (a) shows case A. The crash direction is perpendicular to the panel, and the recesses of the cores equally spaced in rows on the TCP. This relationship causes the straight crushing wrinkle easily. On the other hand, the Figure.2.6 (b) shows case B. The crash direction

is perpendicular to the panel, and the recesses of the cores equally spaced in S-shape. This relationship makes the crushing wrinkle happen in S-shape, which make the buckling resistance is bigger. The crash energy absorption of case A is about 10% different from case B, due to the relationship between the triangular cores of TCP and the crash direction as shown in Figure.2.6. So case B absorbed more crash energy, which is confirmed by numerical analysis. In this paper, we used case B in the proposed structure.



(a) Case A



(b) Case B

Figure.2.6 The directions of TCP and absorbing crash energy.

2.3 Study on the improvement of crash energy absorption

We optimize the geometric parameters design of the proposed structure based on TCP by the response surface methodology (RSM) [2.15] as the optimization method for crash analysis.

2.3.1 Optimum design method

In structural design, the optimum design method is a method of representing the response with the function of the design variables and finding the design variables that best meet the target under the conditions which satisfy the range of design variables and constraint conditions. Here, since the multi-purpose dynamic analysis software LS-DYNA is used for crash analysis, and the analytical solver is separated from the optimization process in the optimum design, it is suitable to utilize RSM which is effective for nonlinear problem as the optimum design method. RSM explores the relationships between several design variables and one or more response variables. Figure.2.7 is a flowchart of an optimum design based on RSM.

(1) To input optimal design condition. The design variables are set from the structure geometry. The range of design variables and the constraint conditions are determined from actual condition. Then, the objective function is input from the requirement.

(2) To choose an appropriate orthogonal table following the design variables and variation range to generate sample data (combination of design variables). Because the level number is unified into three levels: the minimum value, the average value and the maximum value of the change range of design variables. For example, the range of thickness is [0.1mm~0.3mm], so the minimum value is 0.1; the average value is 0.2; the maximum value is 0.3. The three-level orthogonal table $L_9(3^4)$ shown in Table.2.2, and $L_{27}(3^{13})$ shown in Table.2.3 are applied in the RSM optimization of this study. The maximum number of design variables in $L_9(3^4)$ is 4, in $L_{27}(3^{13})$ is 13. The actual number of design variables determines the choice of the orthogonal table. In the tables, numbers 1, 2, 3 mean the minimum value, the average value and the maximum value of the design variables in the tables.

(3) To use above sample data to change the structure models respectively, and then do the crash analysis by using LS-DYNA respectively with these structure models. The crash energy and the weight of structures, which are necessary for the optimization calculations, are obtained from the analysis results.

(4) To organize the one-to-one relationship between sample data and characteristic value, and

create the interpolation approximate formula of response surface. To create a response surface by using statistical method is that to receive an approximate calculation formula of a one-to-one relationship between sample data $[x_i, y_i, \dots](i = 1, 2, \dots, M)$ and characteristic values $Z_i(i = 1, 2, \dots, M)$ of M sets as shown in Table.2.4.

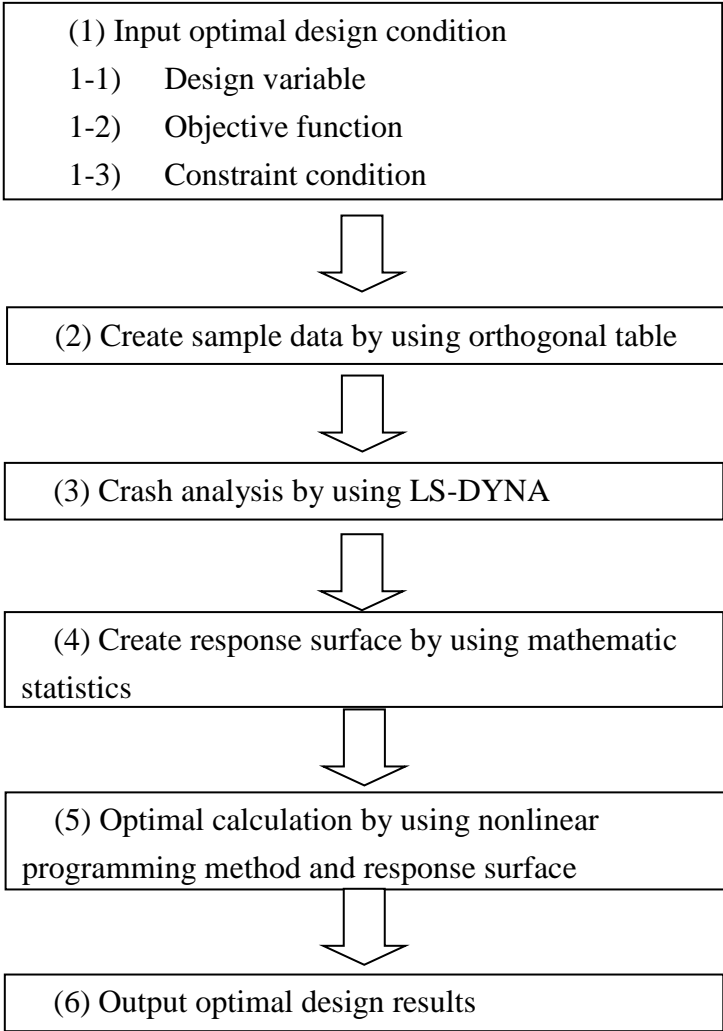


Figure.2.7 Flowchart of response surface optimal method.

Table.2.2 Orthogonal table $L_9(3^4)$.

No.	1	2	3	4
1	1	1	1	1
2	1	2	2	2
3	1	3	3	3
4	2	1	2	3
5	2	2	3	1
6	2	3	1	2
7	3	1	3	2
8	3	2	1	3
9	3	3	2	1

Table.2.3 Orthogonal table $L_{27}(3^{13})$.

No.	1	2	3	4	5	6	7	8	9	10	11	12	13
1	1	1	1	1	1	1	1	1	1	1	1	1	1
2	1	1	1	1	2	2	2	2	2	2	2	2	2
3	1	1	1	1	3	3	3	3	3	3	3	3	3
4	1	2	2	2	1	1	1	2	2	2	3	3	3
5	1	2	2	2	2	2	2	3	3	3	1	1	1
6	1	2	2	2	3	3	3	1	1	1	2	2	2
7	1	3	3	3	1	1	1	3	3	3	2	2	2
8	1	3	3	3	2	2	2	1	1	1	3	3	3
9	1	3	3	3	3	3	3	2	2	2	1	1	1
10	2	1	2	3	1	2	3	1	2	3	1	2	3
11	2	1	2	3	2	3	1	2	3	1	2	3	1
12	2	1	2	3	3	1	2	3	1	2	3	1	2

13	2	2	3	1	1	2	3	2	3	1	3	1	2
14	2	2	3	1	2	3	1	3	1	2	1	2	3
15	2	2	3	1	3	1	2	1	2	3	2	3	1
16	2	3	1	2	1	2	3	3	1	2	2	3	1
17	2	3	1	2	2	3	1	1	2	3	3	1	2
18	2	3	1	2	3	1	2	2	3	1	1	2	3
19	3	1	3	2	1	3	2	1	3	2	1	3	2
20	3	1	3	2	2	1	3	2	1	3	2	1	3
21	3	1	3	2	3	2	1	3	2	1	3	2	1
22	3	2	1	3	1	3	2	2	1	3	3	2	1
23	3	2	1	3	2	1	3	3	2	1	1	3	2
24	3	2	1	3	3	2	1	1	3	2	2	1	3
25	3	3	2	1	1	3	2	3	2	1	2	1	3
26	3	3	2	1	2	1	3	1	3	2	3	2	1
27	3	3	2	1	3	2	1	2	1	3	1	3	2

Table.2.4 Relationship between sample data and characteristic values.

No.	SAMPLE DATA				CHARACTERISTIC VALUES
1	x_1	y_1	→	Z_1
2	x_2	y_2	→	Z_2
⋮	⋮	⋮	→	⋮
<i>i</i>	x_i	y_i	→	Z_i
⋮	⋮	⋮	→	⋮
<i>M</i>	x_M	y_M	→	Z_M

$Z = f(x, y, \dots)$

Here, a quadratic orthogonal polynomial equation is estimated by considering the three- level of sample data as follows. Z is the characteristic value, b_0, b_1, b_2 are the undetermined coefficients, $X_1(x), X_2(x)$ are the terms related to the design variables.

$$Z = b_0 + b_1X_1(x) + b_2X_2(x) \quad (2.3)$$

Since equation (2.3) is an orthogonal polynomial, there is the following relationship of $X_1(x), X_2(x)$.

$$\sum_{j=1}^n X_i(x_j)X_k(x_j) = 0 \quad (i \neq k, \quad i, k = 0, 1, 2) \quad (2.4)$$

n is the level number. By applying $X_0(x_j) = 1$ ($j = 1, 2, \dots, n$) to equation (2.4), the following equations are obtained.

$$\begin{aligned} \sum_{j=1}^n X_1(x_j) &= 0 \\ \sum_{j=1}^n X_2(x_j) &= 0 \\ \sum_{j=1}^n X_1(x_j)X_2(x_j) &= 0 \end{aligned} \quad (2.5)$$

Let $X_1(x), X_2(x)$ be a linear equation and the quadratic equation as follows.

$$\begin{aligned} X_1(x) &= x - a_{10} \\ X_2(x) &= x^2 - a_{21}x + a_{20} \end{aligned} \quad (2.6)$$

Substituting equations (2.6) into equations (2.5), the following equations are obtained.

$$\begin{aligned}
\sum_{j=1}^n x_j - na_{10} &= 0 \\
\sum_{j=1}^n x_j^2 - a_{21} \sum_{j=1}^n x_j + na_{10} &= 0 \\
\sum_{j=1}^n x_j^3 - (a_{10} + a_{21}) \sum_{j=1}^n x_j^2 + (a_{10}a_{21} + a_{20}) \sum_{j=1}^n x_j - na_{20}a_{10} &= 0
\end{aligned} \tag{2.7}$$

Assuming that level values x_1, x_2, x_n are equal intervals, $x_j = j$. From the equation of the sum of arithmetic sequence, the following equations are obtained.

$$\begin{aligned}
\sum_{j=1}^n x_j &= \frac{n(n+1)}{2} \\
\sum_{j=1}^n x_j^2 &= \frac{n(n+1)(2n+1)}{6} \\
\sum_{j=1}^n x_j^3 &= \frac{n^2(n+1)^2}{4}
\end{aligned} \tag{2.8}$$

a_{10}, a_{21}, a_{20} can be obtained by substituting the equations (2.8) into the equations (2.7).

$$\begin{aligned}
a_{10} &= \frac{n+1}{2} \\
a_{21} &= n+1 \\
a_{20} &= \frac{(n+1)(n+2)}{6}
\end{aligned} \tag{2.9}$$

Substituting the equation (2.9) into the equation (2.6), the following equation is obtained.

$$\begin{aligned}
X_1(x) &= x - \frac{n+1}{2} \\
X_2(x) &= x^2 - (n+1)x + \frac{(n+1)(n+2)}{6}
\end{aligned} \tag{2.10}$$

In order to convert the level value x_j from an integer into a normal level value of a regular interval h , the following equation is obtained by using an average value \bar{x} .

$$x_j = \bar{x} - \frac{n+1}{2}h + jh \quad (2.11)$$

The integer j is expressed as follows.

$$j = \frac{x_j - \bar{x}}{h} + \frac{n+1}{2} \quad (2.12)$$

Here, substituting $x = j$ into the equation (2.10), and considering x as a continuous variable, the calculation formal of $X_1(x), X_2(x)$ are obtained as follows.

$$\begin{aligned} X_1(x) &= \frac{x - \bar{x}}{h} \\ X_2(x) &= \frac{(x - \bar{x})^2}{h^2} - \frac{n^2 - 1}{12} \end{aligned} \quad (2.13)$$

Then, in order to obtain the undetermined coefficients of the characteristic value estimation equation (2.3), the sample data and the corresponding characteristics values received from the analysis are substituted into the equation (2.3). The following equation is obtained.

$$\begin{aligned} b_0 + b_1X_1(x_1) + b_2X_2(x_1) &= \bar{Z}_1 \\ b_0 + b_1X_1(x_2) + b_2X_2(x_2) &= \bar{Z}_2 \\ &\dots \\ b_0 + b_1X_1(x_n) + b_2X_2(x_n) &= \bar{Z}_n \end{aligned} \quad (2.14)$$

\bar{Z}_i ($i = 1, 2, \dots, n$) are the average values of the characteristic values. Multiplying $X_0(x_j) = 1, X_1(x_j), X_2(x_j)$ on the both sides of equation (2.14), and considering the orthogonal relation formula (2.5), the following equation is obtained.

$$\begin{aligned}
b_0 n &= \sum_{j=1}^n \bar{Z}_j \\
b_1 \sum_{j=1}^n [X_1(x_j)]^2 &= \sum_{j=1}^n X_1(x_j) \bar{Z}_j \\
b_2 \sum_{j=1}^n [X_2(x_j)]^2 &= \sum_{j=1}^n X_2(x_j) \bar{Z}_j
\end{aligned} \tag{2.15}$$

After rearranging the equation (2.15), the undetermined coefficients b_0, b_1, b_2 are obtained as follows.

$$\begin{aligned}
b_0 &= \frac{\sum_{j=1}^n \bar{Z}_j}{n} = \bar{Z} \\
b_1 &= \frac{\sum_{j=1}^n X_1(x_j) \bar{Z}_j}{\sum_{j=1}^n [X_1(x_j)]^2} \\
b_2 &= \frac{\sum_{j=1}^n X_2(x_j) \bar{Z}_j}{\sum_{j=1}^n [X_2(x_j)]^2}
\end{aligned} \tag{2.16}$$

Substituting $X_1(x), X_2(x)$ of the equation (2.13) and b_0, b_1, b_2 of the equation (2.16) into the equation (2.3), an estimation equation of a single term expressed by an orthogonal polynomial formula is obtained.

Furthermore, in order to improve the approximate accuracy of the estimation formula, a general estimation formula of considering the interaction of any two design parameters x, y is given as follows.

$$Z = b_{00} + b_{10}X_1(x) + b_{20}X_2(x) + b_{01}Y_1(y) + b_{02}Y_2(y) + b_{11}X_1(x)Y_1(y) \tag{2.17}$$

Z is the estimated characteristic value. $b_{00}, b_{10}, b_{20}, b_{01}, b_{02}, b_{11}$ are the undetermined coefficients. $X_1(x), X_2(x)$ are terms related to the design parameter. $Y_1(y), Y_2(y)$ are terms related to the design parameter.

$X_1(x), X_2(x), Y_1(y), Y_2(y)$ in the equation (2.17) have the following relational expressions based on the orthogonality.

$$\begin{aligned}
\sum_{i=1}^n X_1(x_i) &= 0 \\
\sum_{i=1}^n X_2(x_i) &= 0 \\
\sum_{i=1}^n X_1(x_i)X_2(x_i) &= 0 \\
\sum_{i=1}^n Y_1(y_i) &= 0 \\
\sum_{i=1}^n Y_2(y_i) &= 0 \\
\sum_{i=1}^n Y_1(y_i)Y_2(y_i) &= 0
\end{aligned} \tag{2.18}$$

The calculation equations of $X_1(x), X_2(x), Y_1(y), Y_2(y)$ are obtained as follows.

$$\begin{aligned}
X_1(x) &= \frac{x - \bar{x}}{h_x} \\
X_2(x) &= \frac{(x - \bar{x})^2}{h_x^2} - \frac{n^2 - 1}{12} \\
Y_1(y) &= \frac{y - \bar{y}}{h_y} \\
Y_2(y) &= \frac{(y - \bar{y})^2}{h_y^2} - \frac{n^2 - 1}{12}
\end{aligned} \tag{2.19}$$

The sample data and the corresponding characteristic values are substituted into the equation (2.17), and the following equation is obtained.

$$\begin{aligned}
b_{00} + b_{10}X_1(x_1) + b_{20}X_2(x_1) + b_{01}Y_1(y_1) + b_{02}Y_2(y_1) + b_{11}X_1(x_1)Y_1(y_1) &= \overline{Z_{11}} \\
&\dots \\
b_{00} + b_{10}X_1(x_i) + b_{20}X_2(x_i) + b_{01}Y_1(y_j) + b_{02}Y_2(y_j) + b_{11}X_1(x_i)Y_1(y_i) &= \overline{Z_{ij}} \\
b_{00} + b_{10}X_1(x_n) + b_{20}X_2(x_n) + b_{01}Y_1(y_n) + b_{02}Y_2(y_m) + b_{11}X_1(x_n)Y_1(y_m) &= \overline{Z_{nm}}
\end{aligned} \tag{2.20}$$

\bar{z}_{ij} ($i, j = 1, 2, \dots, n$) are the average value of the characteristics values. Multiplying $X_1(x_i) Y_1(y_j)$ on the both sides of equation (2.20), and considering the orthogonal relation formula (2.18), the following equation is obtained.

$$b_{11} \sum_{i=1}^n \sum_{j=1}^n [X_1(x_i) Y_1(y_j)]^2 = \sum_{i=1}^n \sum_{j=1}^n X_1(x_i) Y_1(y_j) \bar{z}_{ij} \quad (2.21)$$

Therefore, the undetermined coefficient of the interaction term is calculated by the following equation.

$$b_{11} = \frac{\sum_{i=1}^n \sum_{j=1}^n X_1(x_i) Y_1(y_j) \bar{z}_{ij}}{\sum_{i=1}^n \sum_{j=1}^n [X_1(x_i) Y_1(y_j)]^2} \quad (2.22)$$

Here, the following equation is expressed by using an average value \bar{x} of the three-level of each level value and a regular interval h .

$$x_1 = \bar{x} - h, \quad x_2 = \bar{x}, \quad x_3 = \bar{x} + h \quad (2.23)$$

Substituting the above equation into the equation (2.10), the following results are obtained.

$$\begin{aligned} X_1(x_1) &= -1, & X_1(x_2) &= 0, & X_1(x_3) &= 1 \\ X_2(x_1) &= \frac{1}{3}, & X_2(x_2) &= -\frac{2}{3}, & X_2(x_3) &= \frac{1}{3} \\ Y_1(y_1) &= -1, & Y_1(y_2) &= 0, & Y_1(y_3) &= 1 \\ Y_2(y_1) &= \frac{1}{3}, & Y_2(y_2) &= -\frac{2}{3}, & Y_2(y_3) &= \frac{1}{3} \end{aligned} \quad (2.24)$$

Substituting the equation (2.24) into the equations (2.16) and (2.22), the calculation formula of the undetermined coefficients is simplified as follows.

$$\begin{aligned}
b_0 &= \bar{Z} \\
b_1 &= \frac{-\bar{Z}_1 + \bar{Z}_3}{2} \\
b_2 &= \frac{3\bar{Z}_1 + 9\bar{Z}_2 + 3\bar{Z}_3}{11} \\
b_3 &= \frac{\bar{Z}_{11} - \bar{Z}_{13} - \bar{Z}_{31} + \bar{Z}_{33}}{4}
\end{aligned} \tag{2.25}$$

The estimation equation of calculating the characteristic values (so-call response surface) will be obtained by performing the above works in order for all the design parameters.

2.3.2 Model's settings of optimization

The optimization question considering the proposed structure as the target is expressed as follows:

$$\text{Find } x = [a, h, h_1, h_2, t_1, t_2, t_3]^T \tag{2.26}$$

$$\text{Target Function } E = f(x)$$

$$\text{Constraint condition } W \leq 3.2kg$$

$$10mm \leq a \leq 30mm, 8mm \leq h \leq 12mm, 0mm \leq h_1 \leq 12mm, 0mm \leq h_2 \leq 12mm$$

$$0.8mm \leq t_1 \leq 1.4mm, 0.8mm \leq t_2 \leq 12mm, 0.8mm \leq t_3 \leq 12mm$$

In this expression, there are seven design variables $x = [a, h, h_1, h_2, t_1, t_2, t_3]^T$, as shown in Figure.2.3, a is the edge length on the top of core, h is the height of core, h_1 is the height of insert member on the truss core panel side, h_2 is the height of insert member on the plate side, t_1 is the thickness of plate, t_2 is the thickness of truss core panel, and t_3 is the thickness of insert member. The variation range of each design variable is shown in expression (2.26).

The target function $E = f(x)$ is to find the maximum crash energy absorption when the crushing deformation reaches 70% of the full length of structure. $W \leq 3.2kg$ is the constraint condition, W is weight of the proposed structure based on TCP and $3.2kg$ is the weight of the existing proposed structure.

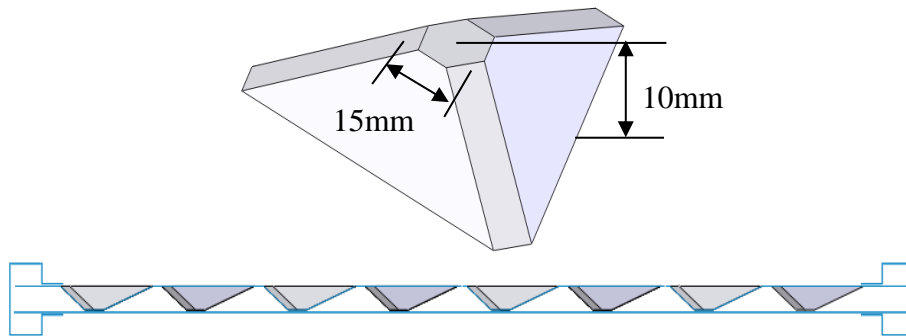
2.3.3 Optimized result

Since the analysis time is considerably long and the design space is complex, we decided to use RSM as the optimization technique. In order that RSM properly finds a meaningful solution, it is necessary that the objective function is sufficiently smooth. Even though the load-time and deformation-time diagrams have the small and high frequency waves, the crash energy absorption value calculated by integration is a smooth function. Therefore, RSM is an appropriate method for the optimization of energy absorption. When the RSM is used to solve the optimization expression (2.26), the geometry optimization calculation procedure is mentioned in section 2.2.1. Now we have to build the proposed truss core panel structure with the calculated optimized geometric variables and then to confirm the accuracy of the calculations through doing the crash analysis by using LS-DYNA.

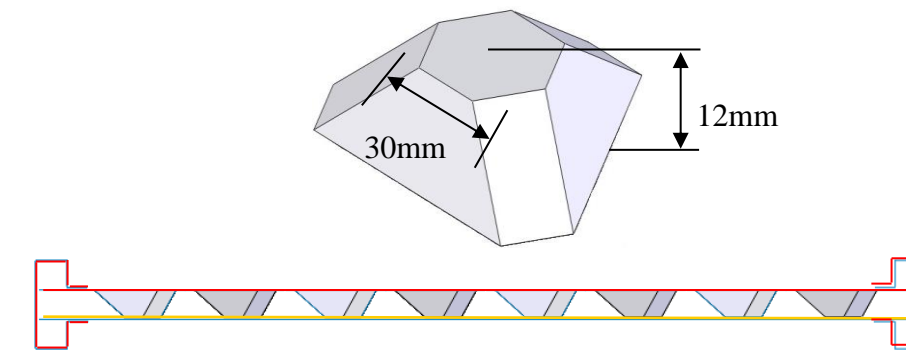
The comparison results between before and after optimization are shown in Table.2.5. As shown in Table.2.5 and Figure.2.8, the thickness of TCP and insert member after optimizing become bigger than in the initial structure. The crash energy absorption has been increased up 62.79% from 10.67MNmm to 17.37MNmm by using geometry optimization.

Table.2.5 Comparison of design variables before and after optimization.

	Before optimization	After optimization
The edge length of upper triangle of core --- (a)	15 mm	30 mm
The height of core ----- (h)	10 mm	12 mm
The height of insert member on core side--- (h_1)	8.5 mm	12 mm
The height of insert member on plate side-- (h_2)	8.5 mm	12 mm
The thickness of plate ----- (t_1)	1.0 mm	0.8 mm
The thickness of truss core panel ----- (t_2)	1.0 mm	1.4 mm
The thickness of insert member ----- (t_3)	1.0 mm	1.4 mm
Crash energy absorption	10.67MNmm	17.37MNmm



(a) Before optimization



— Thicker than before optimization — Thinner than before optimization

(b) After optimization

Figure.2.8 Original and optimal lightweight structures. The dimension of core and the shape of lightweight is compared between before optimization and after optimization are shown in the figure.

2.4 Comparison results between the proposed structure on TCP and the structure based on HCP

In order to confirm the crash energy absorption effect of the proposed structure based on TCP, the structure based on HCP is used to be compared. Considering the geometry and sizes shown in Figure.2.3, we build the structure based on HCP as shown in Figure.2.9 and do the crash analysis simulations under the same condition with the crash analysis of the structure based on TCP. The comparison of absorbing energy character between these optimal structures was investigated. The insert members and plates of honeycomb panel are connected by spot welding.

In the case of the HCP, the absorbing crash energy of case A is about 18% different from case B, due to the relationship between the HCP arrangement and the crash direction as shown in Figure.2.10. We used case B as the compared object to verify the superiority of the structure based on TCP, because the crash energy absorption of case B is more than case A.

Here, in order to compare the crash energy absorption performance, the crash energy absorption optimal result of the structure based on HCP is compared to that of the structure based on TCP, so the structure based on HCP is also necessary to examine the optimization. The target function and the constraints condition are same with the optimized setting of the structure based on TCP. The variation range of design variable is set as follows:

$$45mm \leq L \leq 55mm, 8mm \leq h \leq 12mm, 0mm \leq h_1 \leq 12mm, 0mm \leq h_2 \leq 12mm$$

$$0.8mm \leq t_1 \leq 1.4mm, 0.8mm \leq t_2 \leq 12mm, 0.8mm \leq t_3 \leq 12mm$$

$$0.8mm \leq t_4 \leq 12mm$$

Table.2.6 Comparison of absorbing energy character the optimal structure based on TCP and HCP

	Absorbing energy (MNmm)	Mass (kg)	Absorbing energy per mass (MNmm/kg)
Optimal structure based on TCP	17.37	3.2	5.43
Optimal structure based on HCP	14.65	3.2	4.58

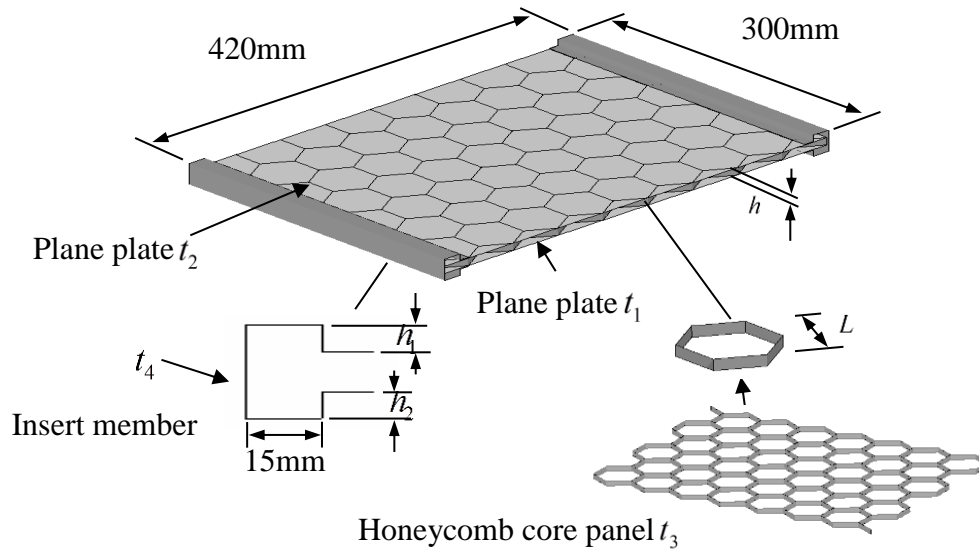


Figure.2.8 The structure based on HCP.

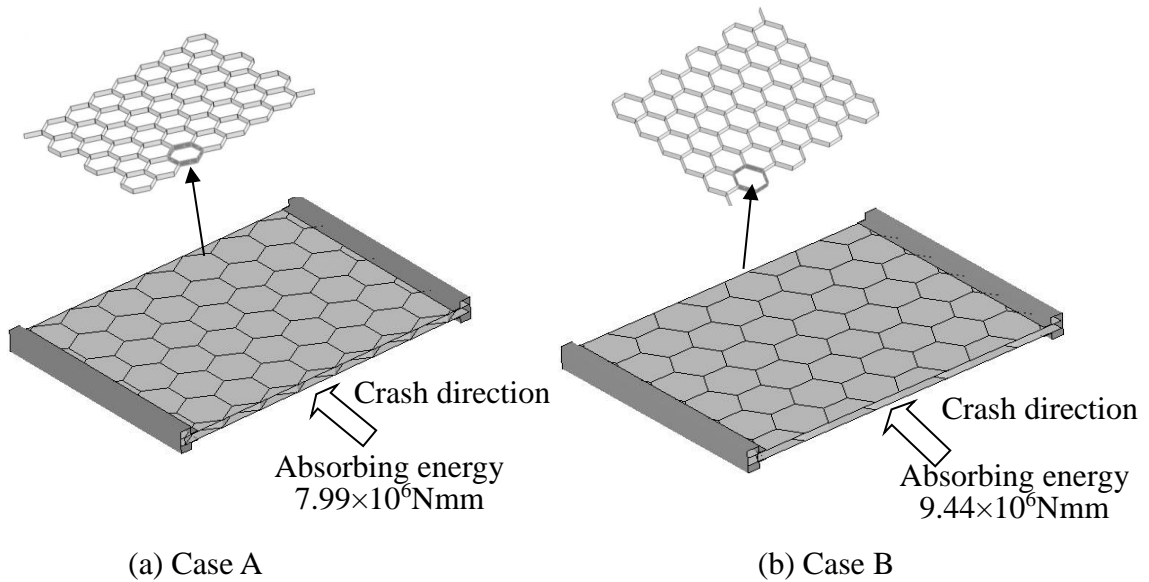


Figure.2.10 Directions of honeycomb structure and absorbing crash energy. The absorbing crash energy of Case A and Case B are different, due to the relationship between the honeycomb structure arrangement and the crash direction.

Table.2.6 shows the comparison results of crash energy absorption between optimal structures based on TCP and HCP. From the simulation results, we can see the crash energy absorption for the structure based on TCP is 18.53% up than the structure based on HCP.

The images of the crash load and the crash energy absorption during collapse deformation process are shown in Figure.2.11 and Figure.2.12. The collapse shapes during collapse deformation are shown in Figure.2.13. The left side in Figure.2.13 shows the collapse shape of the structure based on TCP, and the right side in Figure.2.13 shows the collapse shape of the structure based on HCP. Each pickup crash time in Figure.2.13 (a)~(d) corresponds to the time shown in part A~D of Figures.2.11, 2.12 respectively.

Part A in Figures.2.11, 2.12 and Figure.2.13 (a) show the crash load, the energy absorption and collapse shape when the first buckling of crash occurred. The initial peak load of the optimal structure based on TCP is lower than the optimal structure based on HCP obviously. It means that comparing with the optimal structure based on HCP, the optimal structure based on TCP is structural flexible relatively due to the triangular pyramid cores, which are arranged on the plate uniformly.

Part B in Figures.2.11, 2.12 and Figure.2.13 (b) show the crash load, the energy absorption, and collapse shape when the first buckling fully formed and the next buckling starts to form. From the change of crash load of two structures, the crash load increased because the second buckling of two structures was forming. Comparing with the optimal structure based on HCP, the buckling of the optimal structure based on TCP was narrow and almost concentrated in the first column triangular pyramid cores, so it affected the back end of the structure relatively small. The crash load of the structure based on TCP has relatively higher value than the structure based on HCP during the collapse deformation process after the first buckling formed as shown in Figure.2.11. The crash load and the mechanical work have the higher value in the case when the deformations of each structure are equal. It means the crash energy absorption amount is more.

Part C in Figures.2.11, 2.12 and Figure.2.13 (c) show the crash load, the energy absorption, and collapse shape when the crash energy absorption amounts of the structures based on TCP and HCP are the same. As shown in Figure.2.12, comparing with the structure based on HCP, the crash energy absorption of the structure based on TCP is smaller in the first half of collapse deformation, and tends higher in the second half. The time to energy absorption reversal happened on the part C in Figure.2.12, the crash energy absorption of the structure based on TCP is beginning larger than the structure based on HCP's. As shown in Figure.2.13 (c), the stacked buckling is smaller in the forefront of the structure based on TCP. Meanwhile, the pre-

crash shape of the back end of the structure based on TCP is preserved. Conversely, the collapse deformation occurred in the back end of structure based HCP along with the forepart.

Part D in Figures.2.11, 2.12 and Figure.2.13 (d) show the crash load, the energy absorption, and collapse shape in the final stage of the collapse deformation. Comparing the final buckling mode, the structure based on HCP fell down in the vertical direction, but the structure based on TCP never fall.

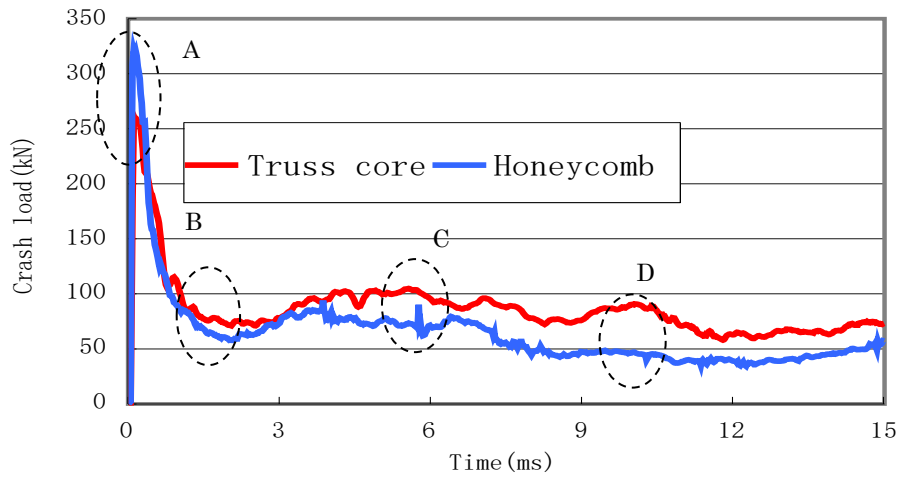


Figure.2.11 Crash load of truss optimal panel and honeycomb optimal panel structure during crash.

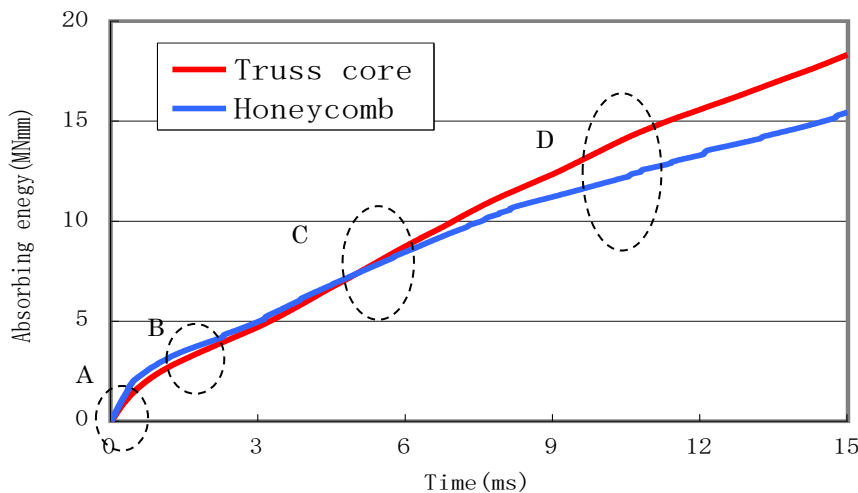
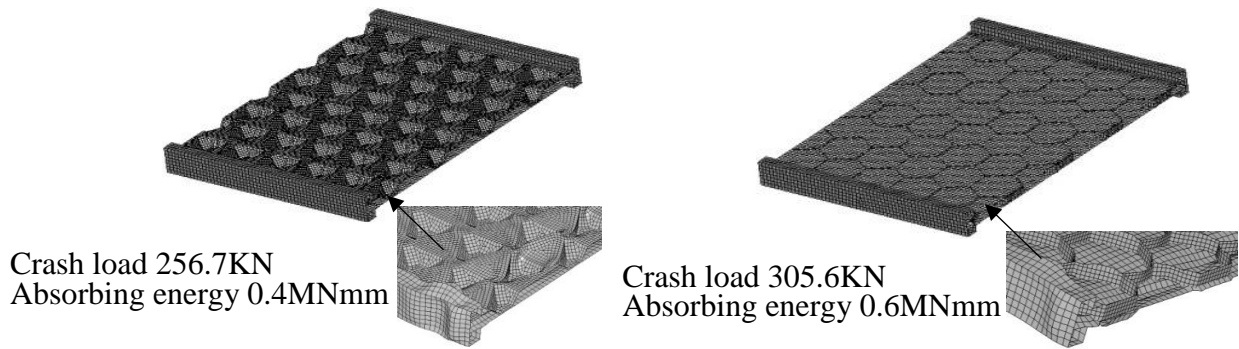
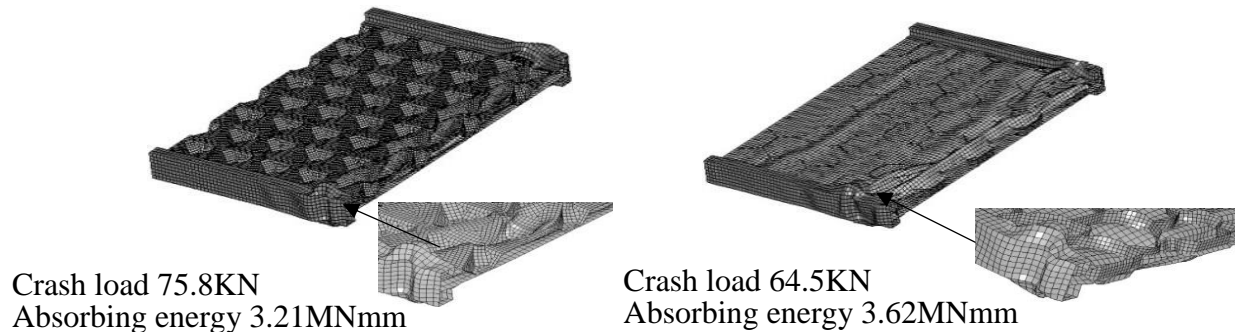


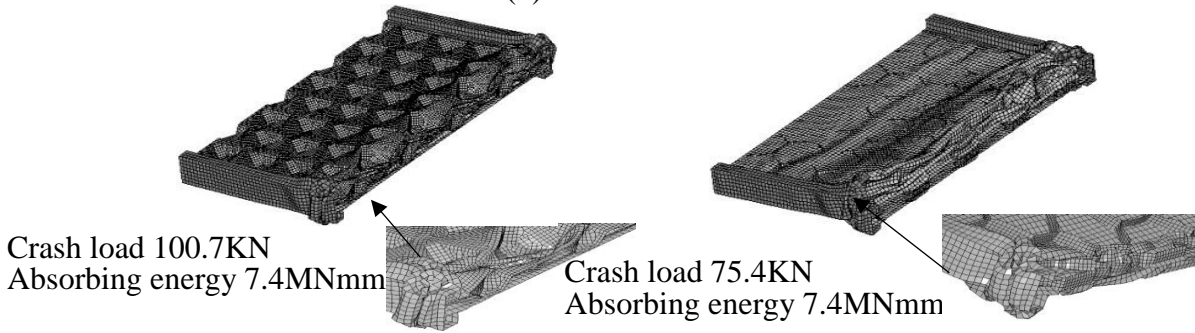
Figure.2.12 Absorbing crash energy during crash of truss optimal panel and honeycomb optimal panel structure during crash.



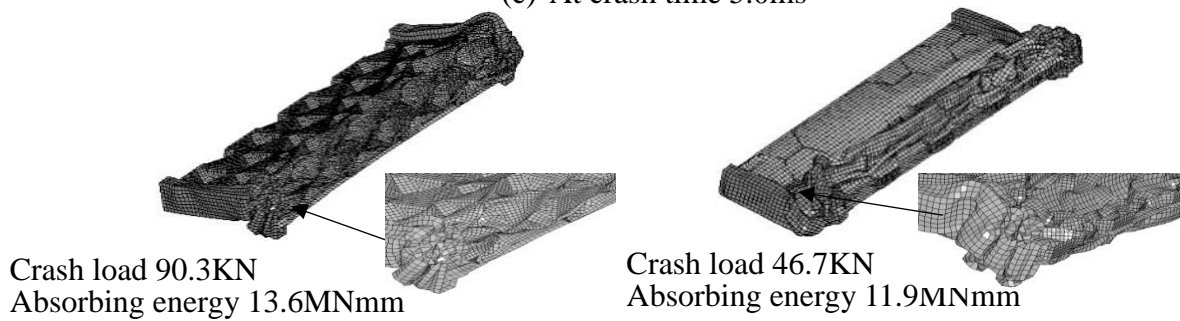
(a) At crash time 0.1ms



(b) At crash time 1.6ms



(c) At crash time 5.0ms



(d) At crash time 10.0ms

Figure.2.13 Crash deformations of each panel structure during crash. The figure shows the crash load and absorbing energy during different crash times. The left side is truss optimal panel structure. The right side is honeycomb optimal panel structure.

2.5 A study on the optimal structure based on TCP

By comparing the TCP structure before and after optimization as shown in Table.2.5 and Figure.2.8, there are big changes in the shape of the core and the insert member, also in the thicknesses of each part. The validity of the optimization result, as well as the mechanical characteristic are discussed as follows.

(1) Figure.2.14 shows crash deformations of the original TCP structure (left side) and the optimal TCP structure (right side). Figure.2.15 shows a partial cross-sectional view of the structure. As shown in Figure.2.14, before the optimization, the flexural stiffness of the plate is strong and the flexural stiffness of TCP is weak, and the buckling is likely to be bent along the weak direction during the crush process. The dashes lines represent the bending center axis of the cross section in Figure.2.15. The bending center axis has been moved to the center after the optimization. When receiving the crash load from the rigid wall, the direction of the weak flexural stiffness of the optimal structure is not clear relatively, and this feature is advantageous for the stability of crush deformation.

(2) With the changes in the cross-sectional shape of the insert members, in the spot welding joint area between the top surface of TCP and the insert members in the optimal structure, a part of the insert member is apart from the core recess of TCP. When the crush acts from the side direction, the part of the plate where there is not joint with the TCP buckles firstly and the first crush wrinkle began shown in Figure.2.16 (a). And then, the crush deformation expands to the adjacent part, and the cores of TCP crush deforms along the line at the same time. As a result, the crush wrinkles are formed as shown in Figure.2.16 (b). After that, the buckling deformation similarly begins at the area of the insert member where is apart from the core recess of TCP and the crush wrinkles gradually expand as shown in Figure.2.16 (c). In this way, the collapse mode in which buckling occurs sequentially from the tip, is the important reason that the structure based on TCP after optimization can stably absorb the crash energy.

Therefore, in order to realize a preferable crush deformation mode as shown in Figure.2.16 (c), considering each component and collision condition, it is a very important design point of adjusting the rigidity balance of the insert members on both sides.

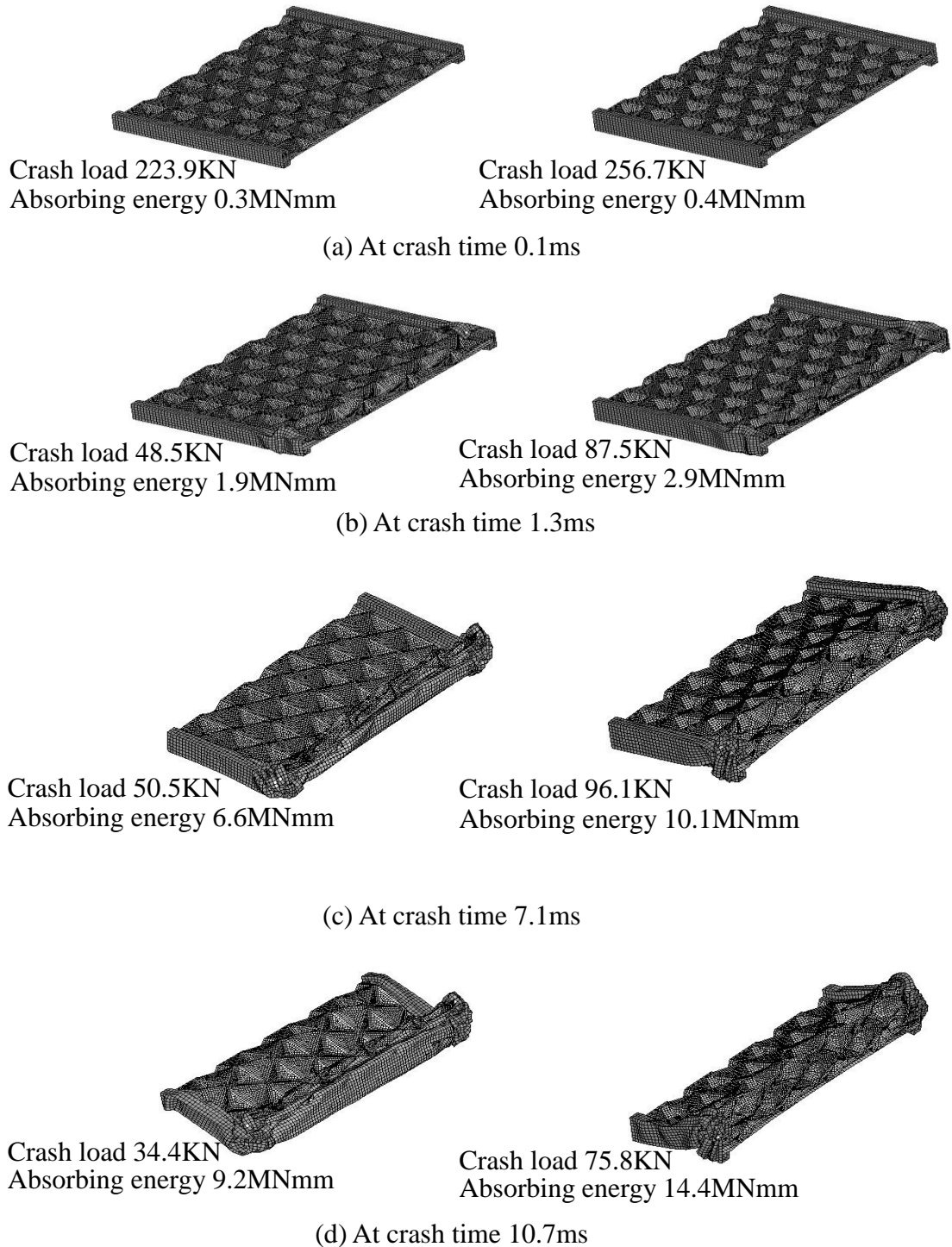


Figure.2.14 Crash deformations of lightweight structures during crash. The figure shows the crash load and absorbing energy during different crash times. The left side is the original lightweight structure, and the right side is optimal lightweight structure.

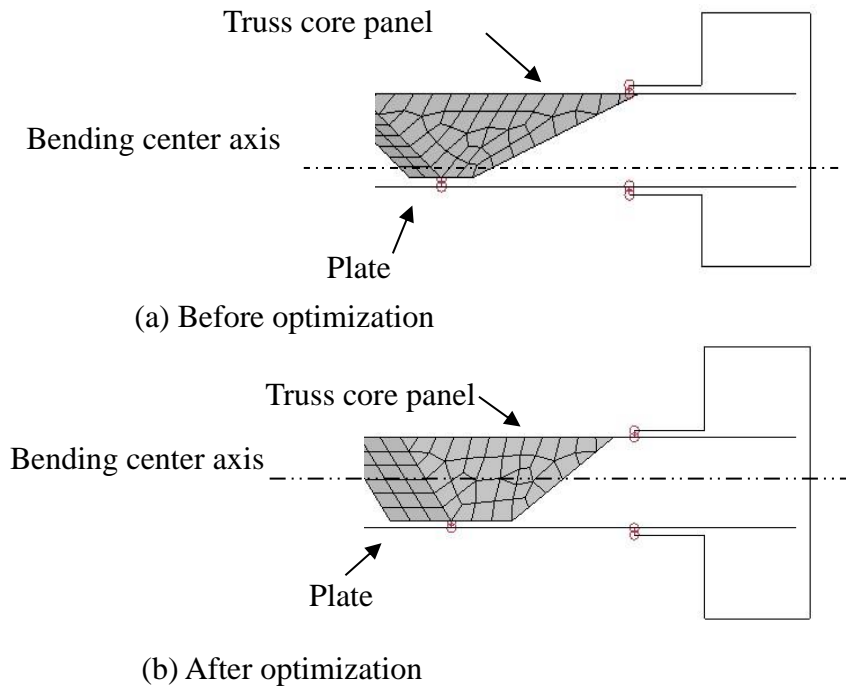


Figure.2.15 Changes of cross section shape of insert member.

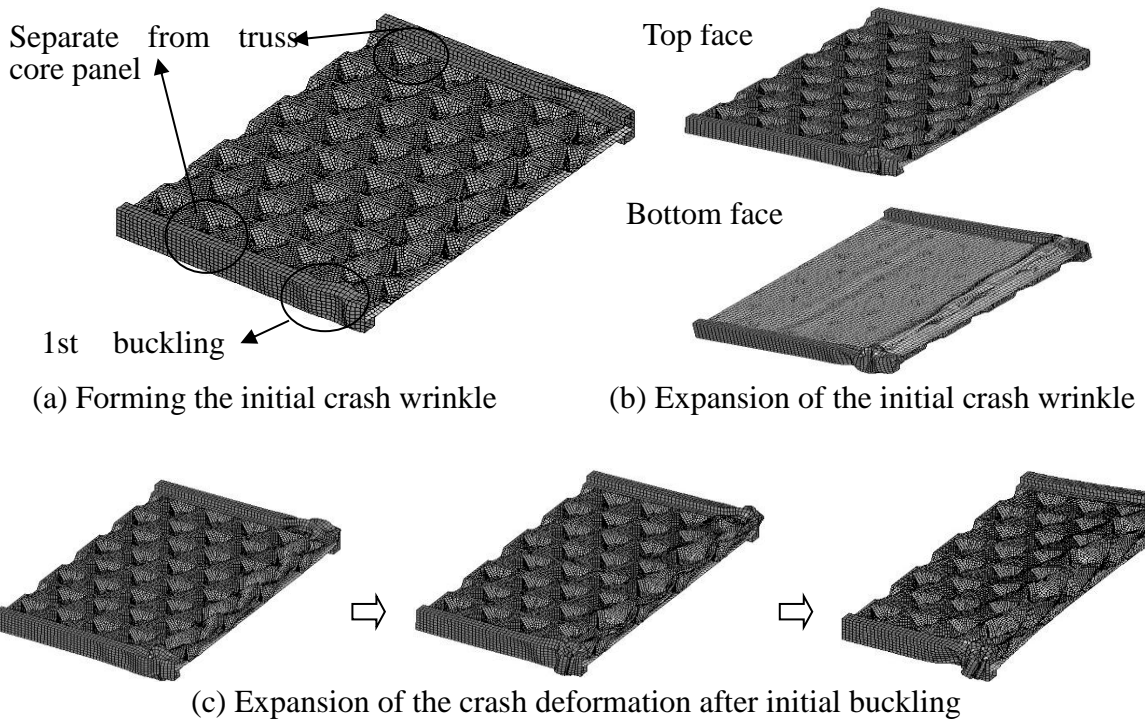


Figure.2.16 Forming and expansion of crash deformation of lightweight structure with truss core panel.

2.6 Summary

In the chapter, a new lightweight is proposed based on the high specific rigidity and high specific strength TCP. And the proposed lightweight structure is optimized by using multi-purpose dynamic analysis software LS-DYNA and the optimization method RSM.

(1) In order to solve the problem that vertical bend occurs when the TCP is crashed from lateral direction and in order to improve crash energy absorption performance, a new type of lightweight structure is proposed by introducing the insert members into the both of TCP.

(2) By combining the multi-purpose dynamic analysis software LS-DYNA and the optimization method RSM, and carrying out the optimum design on the geometric shape and thickness distribution of the proposed lightweight structure, the problem of vertical bend during crush deformation is solved. Furthermore, the crush mode is advantageous for the crash energy absorption which small crush wrinkles overlap continually from the tip to the rear.

(3) In order to verify the superiority of the proposed structure based on TCP, the crash analysis under the same calculation condition is carried out for the structure based on HCP. By comparing the obtained crash energy absorption amount of the same weight, the crash energy absorption performance of the proposed structure based on TCP is better than that of the structure based on HCP. The reasons are discussed by investigating the difference in the geometric configuration the crush mode.

(4) The rationality of the proposed lightweight structure construction based on TCP is discussed in detail. The high crash energy absorption performance can be obtained by keeping long crush deformation from the viewpoint of the position control of the bending center axis and crush wrinkle mechanism of the combination of the core recess and the insert members.

Chapter 3 Crash energy absorbing members of the electrical vehicles by using pairing origami structure

Until now, a lot of origami structures have been invented. Recently, Tachi-Miura polyhedron (denoted by TMP) was designed by Koryo Miura and Tomohiro Tachi [3.1] and has been studied extensively by the folding behavior [3.2,3.3]. Nojima also invented a hexagonal origami shape independently, which can be called Nojima polyhedron (denoted by NP). TMP and NP both are the pairing origami structures. Many researchers have paid attention to the geometrical characteristics of such pairing origami structures. However, so far there are no so much studies of pairing origami structures for applying in the industrial applicability. As we have known, the crash energy absorbing member of vehicles is expected to absorb the collision energy as much as possible. The pairing origami structures have good aspects of collapsing in layer folding along the axial direction.

In this chapter, TMP and NP of pairing origami structures are adopted to compare the collision characteristics and crush modes at the front collision. We utilize multi-purpose dynamic analysis software LS-DYNA to simulate the impact analysis and consider steel as material. And we discuss the possibility of applying TMP and NP as the crash energy absorbing member in vehicle.

3.1 Pairing origami structures

As described in [3.4], the pairing origami is a technique of making three-dimensional structure by affixing two same two-dimensional patterns symmetrically. Figure.3.1 shows such

symmetrical pairing origami features. In the case of one unit of rectangular tube, Miura fold patterns are arranged symmetrically as shown in Figure.3.1 (a), they are pasted together as shown in Figure.3.1 (b). The rectangular tube units are joined together which becomes Figure.3.1 (c). The structure model of Figure.3.1 (c) can be folded in zigzag shape as shown in Figure.3.1 (d). Mountain fold and valley fold lines are drawn by solid and dashed lines respectively in the crease patterns of NP and TMP in Figure.3.2 and Figure.3.3. And then the red lines are the cutting lines.

Figure.3.2 (a), (b), (c) show the crease pattern, the 3D of unit shape of NP, and the whole 3D NP structure respectively [3.4,3.5]. NP is composed of two sheets. There is one zip crease line in one pairing part, which is called a single hinge by Ref. [3.4]. There are 2 mountain fold lines and 4 valley fold lines in pairing parts. It is not necessary to cut the vertical line in pairing part A to separate the two sheets when the 3D shape as shown in Figure.3.2 (b) is folded. The two pairing parts are glued using surface glue. There are 16 mountain fold lines and 10 valley fold lines in main parts (the parts except pairing parts). The sequence of mountain fold and valley fold lines in main parts is valley-mountain-valley/valley-mountain-valley or mountain-valley-mountain/mountain-valley-mountain, which reflects the NP is the mirror symmetry structure as shown in 3D shape.

Figure.3.3 (a), (b), (c) show the crease pattern and 3D shape of unit shape of TMP, the whole 3D TMP structure respectively [3.1], [3.2], [3.6], [3.7], [3.8]. TMP is also composed of two sheets. There are double zip crease lines in one pairing part, which is called double hinge by Ref. [3.5]. There are 2 mountain fold lines and 8 valley lines in pairing parts, and the total of the fold lines in pairing parts of TMP is more than that of NP. It is necessary to cut the vertical line in pairing part A to separate the two sheets when the 3D shape as shown in Figure.3.3 (a) is folded. The two pairing parts are glued using surface glue. The sequence of mountain fold and valley lines in main parts is mountain-valley-mountain/valley-mountain-valley or valley-mountain-valley/mountain-valley-mountain, which reflects the NP is the glide symmetry structure as shown in 3D shape.

The unit shapes of NP and TMP can be characterized by length parameters (l, m, d), an inner angle of parallelogram (α, β) and the folding angle (θ). In NP, $\beta = 2\alpha$ and in TMP, $\beta = \alpha$. As shown in Figure.3.2 (b), Figure.3.3 (b), $\angle ACB$ of right triangle ΔABC is 2α , so $\alpha < 45^\circ$. NP and TMP structures are built by repeating the number (N) of unit shapes as shown in Figure.3.2 (c), Figure.3.3 (c) respectively.

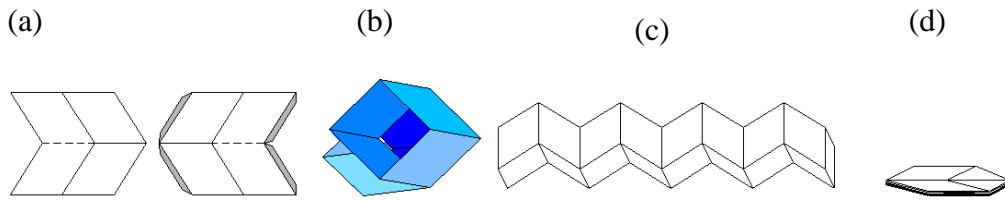
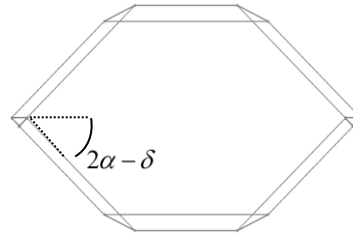
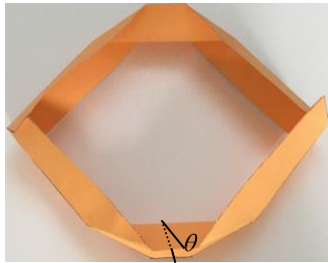
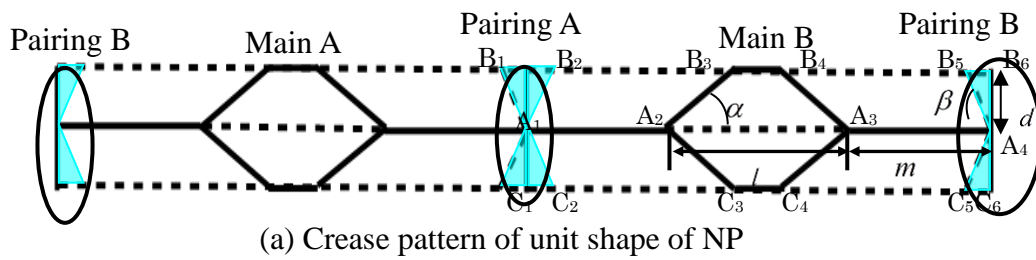
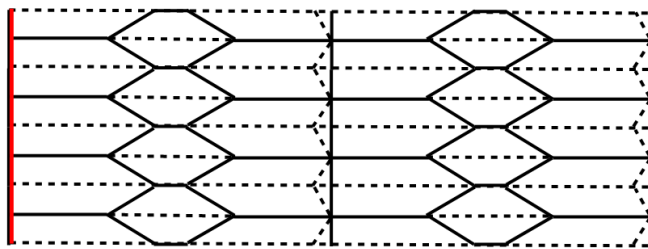


Figure.3.1 Pairing origami structure. (a)Minimum unit development of symmetry pairing origami; (b)Pasted together model of (a); (c)Model of connected minimum units; (d) Model from folded (c).

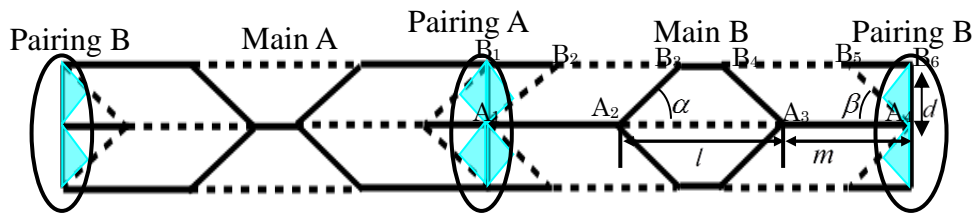


(b) 3D shape of unit NP

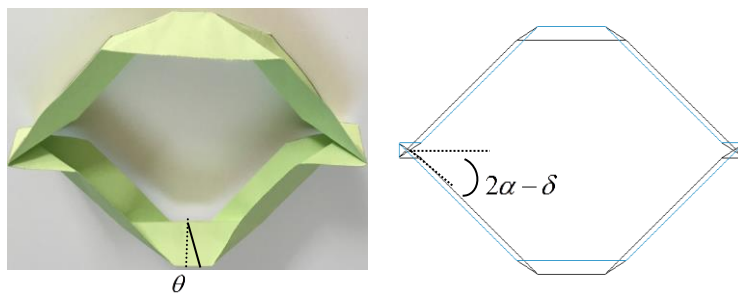


(c) Crease pattern and 3D shape of NP structure

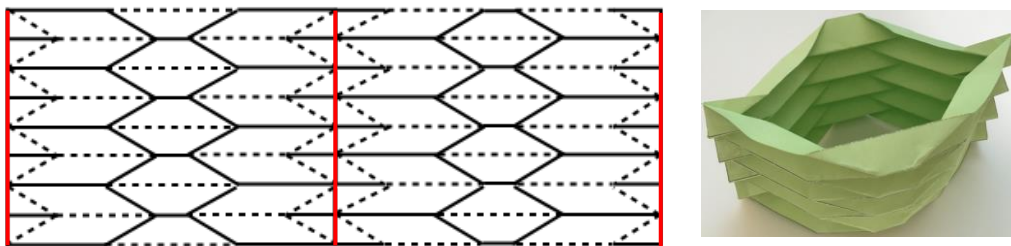
Figure.3.2 The geometrical characteristics of NP. Mountain fold and valley fold lines are drawn by solid and dashed lines. (a) shows the crease pattern of unit shape of NP. (b) shows NP shape deformation in top view when the folding angle changes. (c) shows that 3D shape in right side from the view of upper-left is folded from the crease pattern in left side.



(a) The crease pattern of unit shape of TMP



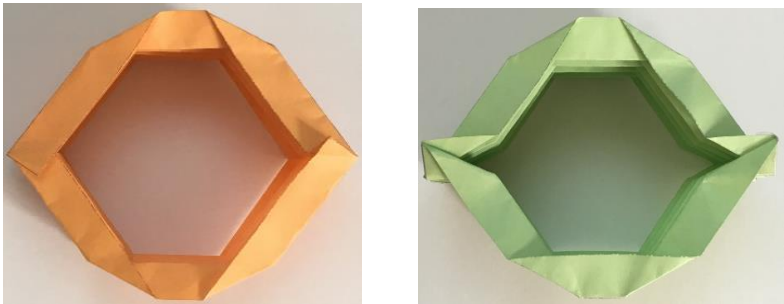
(b) The 3D shape of unit TMP



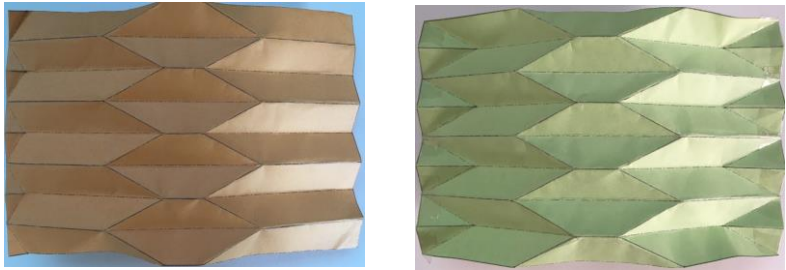
(c) The crease pattern and 3D shape of TMP structure

Figure.3.3 The geometrical characteristics of TMP. Mountain fold and valley fold lines are drawn by solid and dashed lines. (a) shows the crease pattern of unit shape of TMP. (b) shows TMP shape deformation in top view when the folding angle changes. (c) Shows that 3D shape in right side from the view of upper-left is folded from the crease pattern in left side.

Such structure can be folded in two directions. One is in the axial direction like bellows when it is pressed along the axial direction as shown in Figure.3.4 (a). Another is that structure transforms to the original shape of 2 flat sheet when it is pressed from the radial direction as shown in Figure.3.4 (b). The geometrical comparisons between NP and TMP structures are shown in Table.3.1.



NP TMP
(a) Press along the axial direction



NP TMP
(b) Press along the radial direction

Figure.3.4 Shapes after two direction press. One is in the axial direction like bellows when it is pressed along the axial direction as shown in (a). Another is that structure transforms to the original shape of 2 flat sheets when it is pressed from the radial direction as shown in (b). The left side is NP and right side is TMP.

Table.3.1 Geometrical comparisons between NP and TMP.

	NP	TMP
Composed of	Two sheets	Two sheets
Pairing part	Single hinge	Double hinge
	Mountain lines:2	Mountain lines:2
	Valley lines:4	Valley lines:8
	No cutting	Cutting
	Triangle surface glue	Triangle surface glue
Main part	Mountain lines:16	Mountain lines:17
	Valley lines:10	Valley lines:9
	valley-mountain-valley / valley-mountain-valley or mountain-valley-mountain / mountain-valley-mountain	mountain-valley-mountain / valley-mountain-valley or valley-mountain-valley / mountain-valley-mountain
Symmetry	Mirror symmetry	Glide symmetry
Parameters	$[l, m, d, \alpha, \theta, N]$ $\beta = 2\alpha$	$[l, m, d, \alpha, \theta, N]$ $\beta = \alpha$

3.2 Impact analysis by finite element method (FEM)

For the finite element analysis, the geometrical model is established using the 3D CAD design software SOLIDWORKS. The finite element model is then completed with the preprocessor LS-PREPOST. The impact calculations are performed by using dynamic explicit finite element program LS-DYNA.

3.2.1 Analysis method

The following dimension is taken account of proportionality relation for the real dimension of an existing collision energy absorber of a vehicle: the perimeter of cross section is 180mm, the length in axis direction is 375mm, the thickness is 1mm. Figure.3.5 shows the overview of the NP and TMP models. The height of models is fixed as $H = 375mm$, so that the number N is given by $H/(2d\sin(\theta))$ and $d = 10mm$.

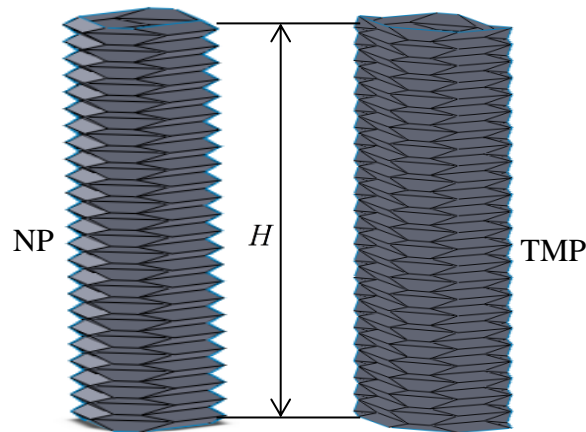


Figure.3.5 The overview of the NP and TMP models.

3.2.2 Simulation method

The impact analysis model is illustrated in Figure.3.6. The pairing structure impacts the rigid wall with the initial velocity of 15000mm/s, and 1000kg mass as the vehicle weight is added to the back of structure.

The structure is made of steel SPCE with the following mechanical properties of Young's modulus $E = 2.1 \times 10^5 \text{N/mm}^2$, Poisson's ratio $\nu = 0.3$, the density $\rho = 7.8 \times 10^{-6} \text{kg/mm}^3$, the yield stress $\sigma = 270 \text{N/mm}^2$. The stress-strain relation for this material is shown in Figure.3.7.

The whole structure is modeled by using 4-node Beltschko-Tsay shell element. The number of elements is 15069, and the number of nodes is 13947. The penalty contact condition is defined between the structure and the rigid wall. The self-contact condition is defined for structure itself. The coefficient of friction is 0.3. During the solution a new time step size is determined by taking the minimum value loop through all the elements.

$$\Delta t = \min(\Delta t_{e1}, \Delta t_{e2}, \dots, \Delta t_{em})$$

$$\Delta t_e = K \left(\frac{L}{C} \right) \quad (3.1)$$

$$L = \frac{A}{\max(L_1, L_2, L_3, L_4)}$$

$$C = \sqrt{\frac{E}{\rho(1 - \mu^2)}}$$

Where m is the number of elements, K is the scale factor which is typically set to a value of 0.9 (default), L is the length of one element, C is stress wave propagation speed, A is the area of element, L_1, L_2, L_3, L_4 are the side lengths of one element.

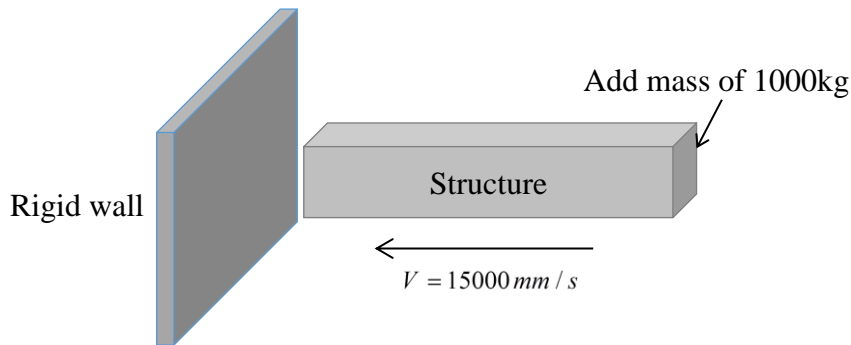


Figure.3.6 Impact analysis model.

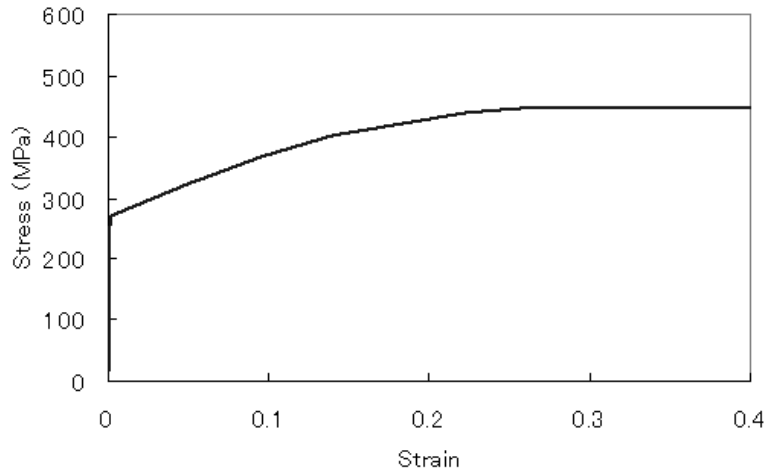


Figure.3.7 Elastic-plastic material property is for structure analysis.

3.3 Optimization of the structure geometry

The proposed pairing structures, which are used as the crash energy absorbing member, are required to absorb sufficient collision energy and avoid too much peaky shock. The optimization technique is used to achieve the goal by using the response surface methodology [3.9, 3.10]. The objective problem is to find the maximum absorbed energy of each pairing structure till the end of the structure's deformation. The optimal problem for the pairing structures is presented by mathematical expression as follows:

$$\begin{aligned}
 &\text{Find } x = [l, \alpha, \theta]^T \\
 &\text{Max. } E = f(x) \\
 &35\text{mm} \leq l \leq 55\text{mm} \\
 &30^\circ \leq \alpha \leq 40^\circ \\
 &30^\circ \leq \theta \leq 50^\circ
 \end{aligned} \tag{3.2}$$

Here, in order to increase the efficiency of creating new mesh by referring to the shape change during the optimization process, the coordinates of each point shown in Figure.3.8 and Figure.3.9 are expressed as the function of the design variable (l, α, θ) .

3.3.1 The relationship between configuration and parameters in NP

As shown in Figure.3.8, the points $(A_1, A_2, B_1, B_2, B_3)$ and $(A_3, A_4, B_4, B_5, B_6)$ are y-axial symmetry, and points $(B_1, B_2, B_4, B_5, B_6)$ and $(C_1, C_2, C_4, C_5, C_6)$ are z-axial symmetry. Therefore, after key points $(A_1, A_2, B_1, B_2, B_3)$ are obtained, other points can be also received automatically. These key points are expressed as (l, α, m, d) .

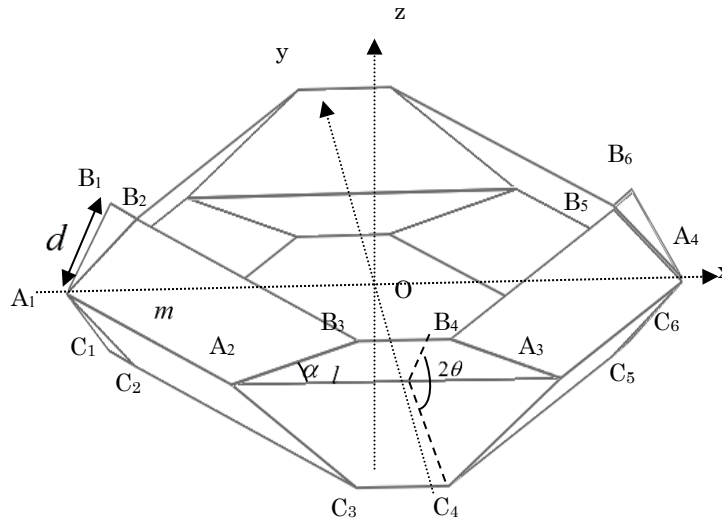


Figure.3.8 Slanted view of 3D NP unit cell. The key-nodes of the unit cell and the mirror symmetry structural relationship are represented.

As shown in Figure.3.9, the lengths of each side and angle are fixed values as following:

$$|A_1B_1| = |A_4B_6| = d, \quad |A_2A_2| = l, \quad |A_1A_2| = |A_3A_4| = m$$

$$\angle B_3A_2A_3 = \alpha, \quad \angle B_2A_1A_2 = \beta = 2\alpha$$

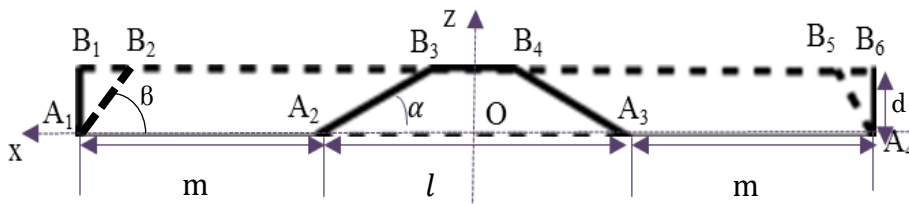


Figure.3.9 Drawing of unit NP.

The lengths of each following sides are expressed as the fixed values as shown in equation (3.3).

$$\begin{aligned}
|A_1B_2| &= \frac{|A_1B_1|}{\sin(2 \times \alpha)} = \frac{d}{\sin(2 \times \alpha)} \\
|B_3B_4| &= |A_2A_3| - 2 \times \frac{d}{\tan(\alpha)} = l - 2 \times \frac{d}{\tan(\alpha)} \\
|B_2B_3| &= |A_1A_2| + \frac{d}{\sin(2 \times \alpha)} = m + \frac{d}{\sin(2 \times \alpha)} \\
|B_1B_2| &= \frac{|A_1B_1|}{\tan(2 \times \alpha)} = \frac{d}{\tan(2 \times \alpha)}
\end{aligned} \tag{3.3}$$

As the angle θ changes, the model is raised from a flat shape to a three-dimensional shape. The points A_1 and A_2 are expressed by equation (3.4) with varying angle δ .

$$\begin{aligned}
A_1 &\left\{ \begin{aligned} x &= \frac{|A_2A_3|}{2} + |A_1A_2| \times \cos(2 \times \alpha - \delta) = \frac{l}{2} + m \times \cos(2 \times \alpha - \delta) \\ y &= 0 \\ z &= 0 \end{aligned} \right. \\
A_2 &\left\{ \begin{aligned} x &= \frac{|A_2A_3|}{2} = \frac{l}{2} \\ y &= |A_1A_2| \times \sin(2 \times \alpha - \delta) = m \times \sin(2 \times \alpha - \delta) \\ z &= 0 \end{aligned} \right.
\end{aligned} \tag{3.4}$$

And then the points B_2 and B_3 are expressed by equation (3.5).

$$B_2 \left\{ \begin{aligned} x &= \frac{|B_3B_4|}{2} + |B_2B_3| \times \cos(2 \times \alpha - \delta) \\ &= \frac{l - 2 \times \frac{d}{\tan(\alpha)}}{2} + \left(m + \frac{d}{\sin(2 \times \alpha)}\right) \times \cos(2 \times \alpha - \delta) \\ y &= 0 \\ z &= |A_1A_2| \times \sin(\theta) = d \times \sin(\theta) \end{aligned} \right. \tag{3.5}$$

$$B_3 \left\{ \begin{array}{l} x = \frac{|B_3B_4|}{2} = \frac{l - 2 \times \frac{d}{\tan(\alpha)}}{2} \\ y = |B_2B_3| \times \sin(2 \times \alpha - \delta) = \left(m + \frac{d}{\sin(2 \times \alpha)}\right) \times \sin(2 \times \alpha - \delta) \\ z = |A_1A_2| \times \sin(\theta) = d \times \sin(\theta) \end{array} \right.$$

The point B_1 is on the same straight line with line, and the coordinate is determined in equation (3.6).

$$\begin{aligned} K &= \frac{|B_1B_2| + |B_2B_3|}{|B_2B_3|} \\ \overrightarrow{B_3B_1} &= \overrightarrow{B_3B_1} \times K \\ B_1 \left\{ \begin{array}{l} x = (x_{B_2} - x_{B_3}) \times K + x_{B_3} \\ y = (y_{B_2} - y_{B_3}) \times K + y_{B_3} \\ z = |A_1A_2| \times \sin(\theta) = d \times \sin(\theta) \end{array} \right. \end{aligned} \quad (3.6)$$

Since the value of obtained from equations (3.4) and (3.5) is equal to the value in equation (3.3), the relationship of angles is expressed in equation (3.7).

$$\cos(2 \times \alpha - \delta) = 2 \times \cos^2(\alpha) - \sqrt{1 - (\sin(\theta)\sin(2 \times \alpha))^2} \quad (3.7)$$

3.3.2 The relationship between configuration and parameters in TMP

Just like NP, the key points of TMP as shown in Figure.3.10 are expressed by four parameters (l, α, m, d) as following equation (3.8).

$$\begin{aligned} |B_3B_4| &= |A_2A_3| - \frac{2 \times d}{\tan(\alpha)}, \quad |B_2B_3| = m \\ |A_1A''| &= |A''B''| = \frac{|A_1B_1|}{2 \times \sin(2 \times \alpha)} = \frac{d}{2 \times \sin(2 \times \alpha)} \end{aligned} \quad (3.8)$$

$$\begin{aligned}
A_1 & \begin{cases} x = \frac{|A_2 A_3|}{2} + |A_1 A_2| \times \cos(2 \times \alpha - \delta) = \frac{l}{2} + m \times \cos(2 \times \alpha - \delta) \\ y = -\frac{|A_1 B_1|}{2} \times \cos(\theta) = -\frac{d}{2} \times \cos(\theta) \\ z = 0 \end{cases} \\
A_2 & \begin{cases} x = \frac{|A_2 A_3|}{2} = \frac{l}{2} \\ y = (|A_1 A_2| - |A_1 A''|) \times \sin(2 \times \alpha - \delta) = \left(m - \frac{d}{2 \times \sin(2 \times \alpha)}\right) \times \sin(2 \times \alpha - \delta) \\ z = 0 \end{cases} \\
B_1 & \begin{cases} x = x_{A_1} = \frac{l}{2} + m \times \cos(2 \times \alpha - \delta) \\ y = -y_{A_1} = \frac{d}{2} \times \cos(\theta) \\ z = d \times \sin(\theta) \end{cases}
\end{aligned}$$

$$B_2 \begin{cases} x = \frac{|B_3 B_4|}{2} + |B_2 B_3| \times \cos(2 \times \alpha - \delta) \\ = \frac{l - 2 \times \frac{d}{\tan(\alpha)}}{2} + m \times \cos(2 \times \alpha - \delta) \\ y = y_{B_1} = \frac{d}{2} \times \cos(\theta) \\ z = d \times \sin(\theta) \end{cases}$$

$$B_3 \begin{cases} x = \frac{|B_3 B_4|}{2} = \frac{l - 2 \times \frac{d}{\tan(\alpha)}}{2} \\ y = (|B_2 B_3| + |A'' B''|) \times \sin(2 \times \alpha - \delta) = \left(m + \frac{d}{2 \times \sin(2 \times \alpha)}\right) \times \sin(2 \times \alpha - \delta) \\ z = d \times \sin(\theta) \end{cases}$$

$$y_{A_2} = y_{A_2} - d \times \cos(\theta) \Rightarrow \sin(2 \times \alpha - \delta) = \cos(\theta) \times \sin(2 \times \alpha)$$

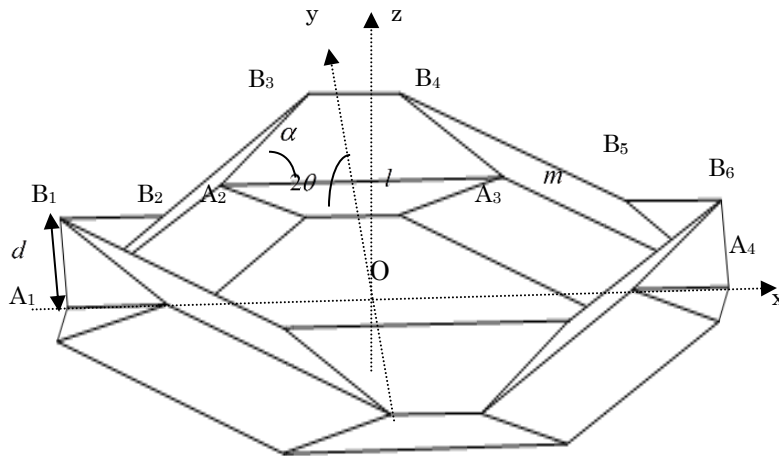


Figure.3.10 Slanted view of 3D TMP unit cell. The key-nodes of the unit cell and the glide symmetry structural relationship are represented.

3.4 Optimization results and discussion

The optimum design parameters with the resulting values are shown in Table.3.2. Figure.3.11 and Figure.3.12 show the absorbed energy and the crushing force comparisons between optimal NP and optimal TMP in the crush processing respectively. In general, so-called bottoming phenomenon occur when the vehicle collapse deformation reaches 70% [3.11]. Here, the bottoming phenomenons of NP and TMP occur at almost the same time when the deformations reach 90%. After that, the crushing force is rapidly increasing that do not contribute to the energy absorption. The absorbed energy value of optimal TMP is more than that of the optimal NP before the deformation reaches 65%. The optimal NP is capable of absorbing energy more than that of the optimal TMP finally, because after that the TMP bent with a larger deviation from the central axis comparing to the optimal NP as shown in Figure.3.13. The NP and TMP are multi-layer structure arranged by concave/convex folding shapes in axial direction and the deformation mode is governed by the folding stripes, so that the very smooth crushing force wave is observed.

Table.3.2 Optimum design parameters and the result values.

	Optimal NP	Optimal TMP	Existing member	RSC
r [mm]	55	45		
α [°]	40	40		
θ [°]	30	30		
Absorbed energy[Nmm]	6.05E+6	4.53E+6	4.4E+6	8.4E+6
Absorbed energy per mass [Nmm/kg]	8.6E+6	6.4E+6	8.2E+6	15.9E+6

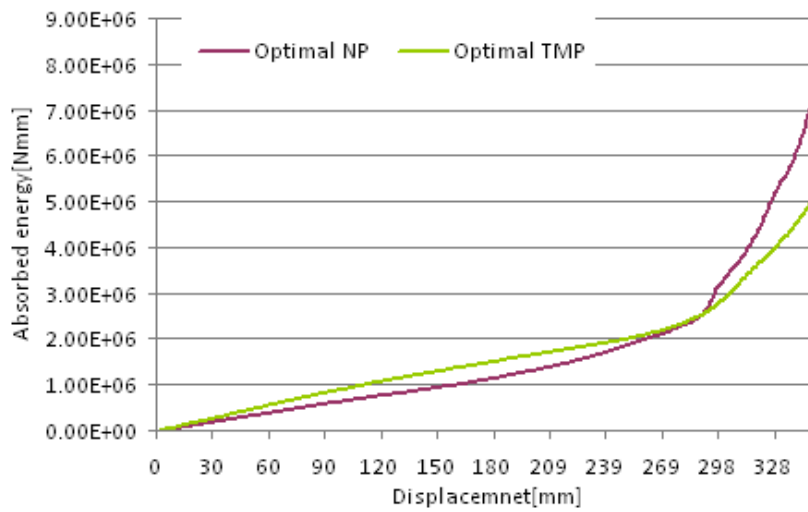


Figure.3.11 Absorbed energy-displacement curves of optimal NP and optimal TMP. The optimal NP is the red line, and the optimal TMP is the green line.

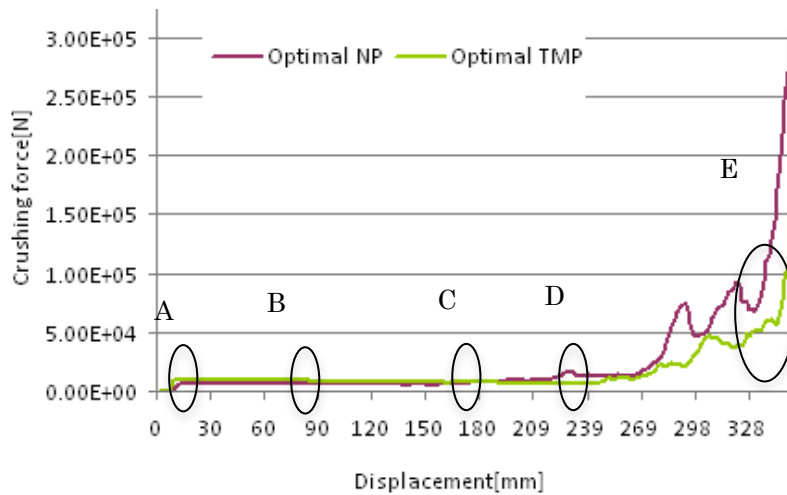


Figure.3.12 Crushing force-displacement curves of optimal NP and optimal TMP. The optimal NP is the red line, and the optimal TMP is the green line.

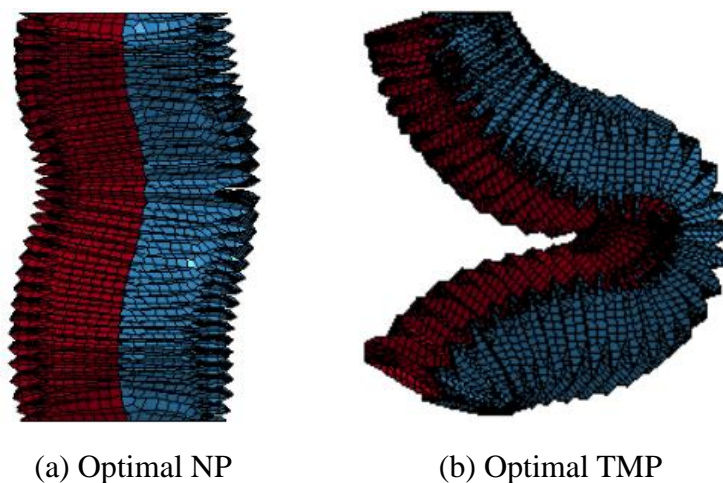


Figure.3.13 Crush deformations of optimal NP and TMP. TMP bent with a larger deviation from the central axis comparing to the optimal NP.

Figure.3.14 shows the crash tentative deformation modes of NP and TMP. The left side shows the deformation of NP, and the right side shows the deformation of TMP. (a) ~ (e) in Figure.3.14 are corresponding to A ~ E in Figure.3.12.

As shown in Figure.3.14 (a) and part A of Figure.3.12, at the beginning stage of crash deformations, NP and TMP both crush with smaller accordion-like wrinkles at the front part of structures.

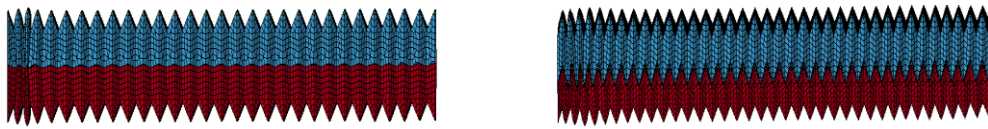
As shown in Figure.3.14 (b) and part B of Figure.3.12, the crushing force of NP remains stable, and the smaller accordion-like wrinkles occur at the bottom part of NP structure, so that it continues crush deformation along the axis direction. The crushing force of TMP starts to decrease because the bigger accordion-like wrinkles occur at the middle part of TMP structure. In the paper (Yang *et al.* [3.12]), we have already discussed the application possibility of NP and TMP. In the application of beer cans, while the structure length is shorter (about 153mm), TMP has more absorption energy.

As shown in Figure.3.14 (c) and part C of Figure.3.12, NP continues to crush with accordion-like wrinkles; in addition, the accordion-like deformations occur not only in each layer but also between layers which makes the middle part bend a little from the central axis. On the other hand, the middle part of TMP structure asymmetrically collapses which makes the bend structure deviate from the central axis.

As shown in Figure.3.14 (d) and part D of Figure.3.12, TMP has completely deformed longitudinally. On the other hand, small bulkings of NP are stacking; NP continues to maintain relatively stable axial deformation and has not fallen down, so NP still can afford to absorb the collision energy. From this stage, the crushing force of NP is higher than that of TMP.

As shown in Figure.3.14 (e) and part E of Figure.3.12, it is the final stage of crash deformation, the bottoming phenomenon occurs and the crushing force rapidly increased.

Hagiwara et al. has confirmed that the appropriate position of beads on the appropriate thin-walled column of side member can actively conduct the longitudinal crushing deformation to avoid Euler buckling phenomenon [3.13]. Here, NP keeps the crushing force stable due that the folding strips of pairing hinge part like the edge beads; the face structure arranged by valley lines and mountain lines like the concave/convex beads.



(a) At crash time 0.002s



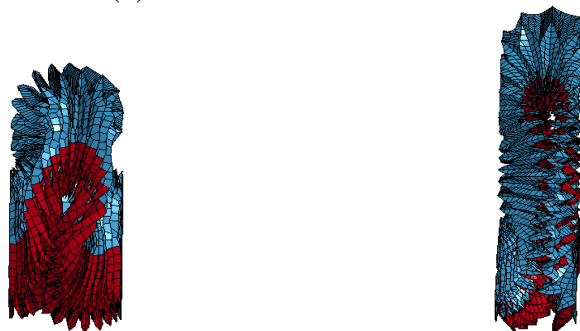
(b) At crash time 0.005s



(c) At crash time 0.012s



(d) At crash time 0.016s



(e) At crash time 0.0225s

Figure.3.14 Structure deformations during crash analysis. The left side is the NP and the right side is TMP.

3.5 Comparison with the existing rectangular cross section structure and RSC structure

In order to discuss the crash energy absorption of NP and TMP, the existing rectangular cross section structure which is used for energy absorbed structure of vehicle and the reversed spiral cylindrical origami structure (RSC) are adopted for the comparison. The absorbed energy per mass of the optimal NP ($8.6 \times 10^6 \text{Nmm/kg}$) is a little more than that of the existing rectangular cross section structure ($8.2 \times 10^6 \text{Nmm/kg}$), but the absorbed energy per mass of the optimal TMP ($6.4 \times 10^6 \text{Nmm/kg}$) is less than that of the existing rectangular cross section structure. Our group has already shown that the RSC structure is extremely excellent for the absorption energy performance ($15.9 \times 10^6 \text{Nmm/kg}$) [3.10]. Comparing to NP and TMP, the RSC structure is still capable of more absorbing energy. However, the manufacturing method of RSC structure is hydro forming with high-cost. Conversely, NP and TMP can be produced easily and cost-effectively: firstly, the shape is formed based on origami-forming [3.14] from a steel plate sheet, secondly, two sheets are joined by spot welding process, which is typically used in the manufacture of the existing collision energy absorber.

3.6 Summary

The absorption energy performances of NP and TMP are investigated to consider these structures to be applied in a wide range of applications. The optimization process with the objective of maximizing the absorption energy has been carried out. As a result, NP regularly deforms from the front to the end, and it has relatively better energy absorption characteristic. On the other hand, relative to the mirror symmetry structure of NP, TMP is easy to bend due to the non-axisymmetry. Comparing with RSC, NP has the advantage of manufacture cost, so an excellent energy absorbing member based on NP is the future challenge.

Chapter 4 Application of vehicle crash technology and origami structures to daily necessities

4.1 Previous researches

After the Great East Japan Earthquake in March, 2011, self-protection is a very important issue for everyone, and it is an urgent request to invent helmets which are convenient for storage, for example, the one which is not disturbing to walk through aisles between desks and enough small to put in lockers in class room of school. There are many foldable helmets in market (for example, the ones by the Toyo Bussan Co., Ltd., in 2012 and 2014 [4.1,4.2], and the ones by DIC corporation in 2013 [4.3]) but they can be folded in only one direction, so those folded states are not small enough for general requests. Therefore, we challenge to invent a helmet which is foldable in two directions [4.4,4.5].

Just at that moment, we were asked by Japan Broadcasting Corporation (NHK) to participate as one team to the competition “Sugo-waza (Outstanding techniques)” with the title “The competition of the strongest hat (helmet) for safety” which is a TV program by NHK. The regulations by NHK is as follows: a hat is foldable and fit the box of 300mm×150mm×50mm, and when an iron ball of 5 kg at 1m height above the hat is dropped, the impact force on head should be reduced to not more than 4.9 KN (generally speaking, one tenth of the original). The size of box showed by NHK is pretty small, and commercially available helmets cannot fit it. Three examples of helmets on the market are shown in Table.4.1, and the left example has its volume 420% of the box, the middle one 114%, and the right one 240%.

We invent a cover part which fits the box and leaves enough space to put energy-absorbing materials together. For the length of energy-absorbing materials the longer the better in general,

which means the length of unfolded shape is long but the one of folded shape is short. Using the origami-based structure, we find an energy absorbing structure which fits the box when it is folded and which has enough length when it is unfolded.

Folding a helmet with hard materials is deeply related to the origami-based technology. We should work for both compact foldable structures and energy-absorbing structures. The helmet we invented is divided into three parts, the cover part and two energy-absorbing parts.

For an energy-absorbing structure which is foldable, we use a prism of the reverse spiral cylindrical origami-based structure (RSC) which can control the initial load, has no the Euler buckling halfway, and has the small deformation [4.6~4.10] as shown in Figure.4.1. We think this structure is also useful for the energy absorption of the helmet. We choose cardboards instead of materials used in the Table.4.1 for commercial products of helmets, since cardboards are a little flexible and much cheaper than others. In the Figure.4.1 “Conventional one” means the load-deformation characteristic diagram of the quadrilateral thin hollow pillow structure used for the energy-absorbing materials for car [4.11].

Table.4.1 Helmets on sale.

Products			
Size[mm](L×W×H)	280×225×150	332×221×35	358×197×45
Material	ABS	PP+PE	PP+PE+ABS
Weight [g]	400	370	370

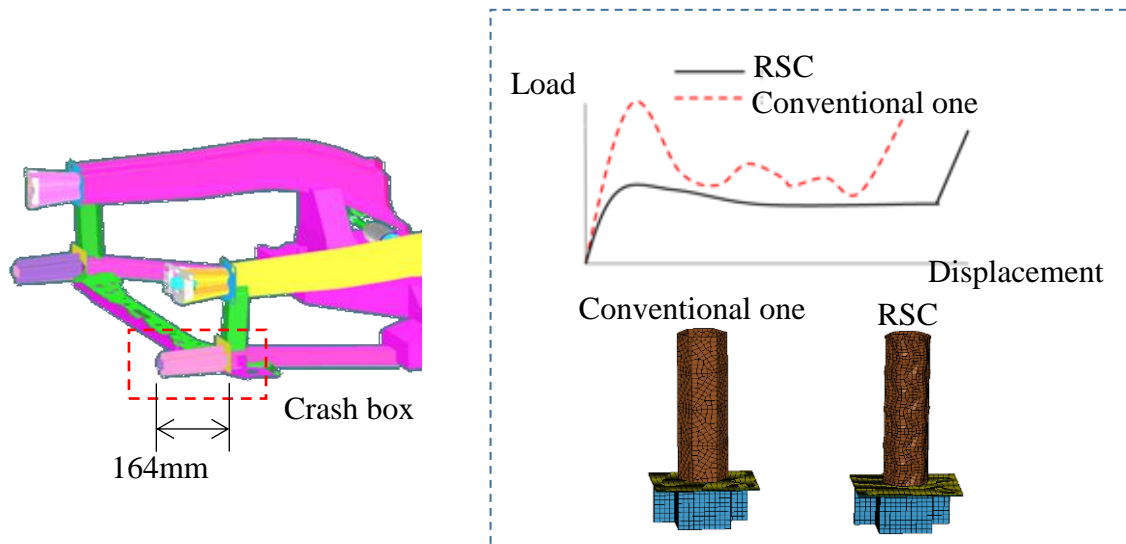


Figure.4.1 Load-displacement characteristics of RSC and conventional one.

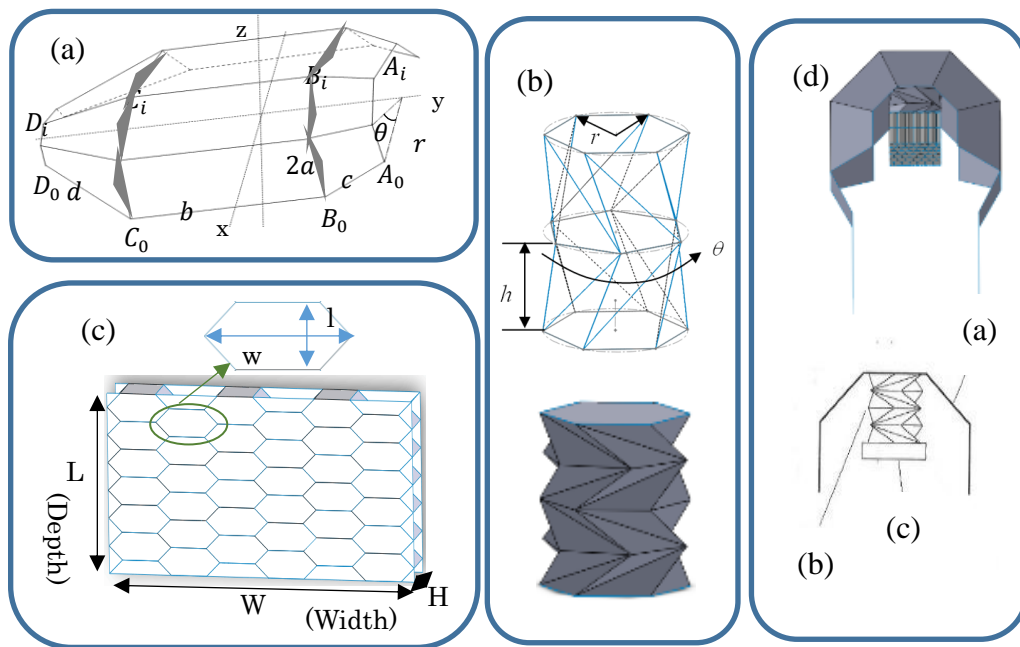


Figure.4.2 Cardboard helmet of NHK confrontation.

4.2 Newly developed safety foldable helmet

As mentioned in the section 4.1, we choose RSC for energy-absorbing structure, but it is not enough because of the round shape of head, so we add the honeycomb structure to improve fitting. Therefore, the helmet invented for the competition “Sugo-waza” consists of three parts as shown in Figure.4.2, namely, (a) the cover with accordion folding, (b) the RSC structure and (c) the honeycomb structure, whose details are shown as follows.

4.2.1 The origami structure of the cover part

We employ the method developed by Nara, one of authors, et al. [4.12~4.14] on “Continuous flattening problems of polyhedra” as a design of the cover. Firstly, since it is impossible to flatten a surface S of non-zero Gauss curvature, we approximate S by a polyhedral surface. Secondly, we apply the known results to continuously flatten S . We design a cover which is simple and easy to transform its shape. Hence, the cover can be flattened like an umbrella which is convenient for storage, and its flat folded state is like a foldable fan.

The cover is comprised by congruent pieces (Figure.4.2 (a)) and can be easily flattened into the multilayered shape (Figure.4.2 (b)). If we use rigid materials for the cover, suitable holes would be required to avoid collisions. We can calculate the sizes of holes by using the kite property [4.12, 4.14]. The design of the safety helmet proposed here has very small holes (shaded parts in Figure.4.2 (a)). If we use flexible materials like a piece of paper, such holes are not necessary. We choose cardboards for materials which are flexible enough to flatten the cover part without holes. The unfolded shape of the cover is a polyhedron inscribed in a rotated surface about an axis. Pairs of adjacent vertices on a plane orthogonal to the axis have an equal distance.

The example of a helmet showed in Figure.4.2 (a) has the unfolded shape which is a half polyhedron (cut off the pecks), composed of an octagonal prism and two (not necessary congruent) octagonal pyramids. In this example, the dihedral angle of common edges of the prism and the pyramid is not less than 135° so that the isosceles triangles shaded to avoid collisions have the height with less than 8.5% of the length of common edges, where the value 8.5% is a little larger than the exact value to move smoothly, and the value can be smaller than 8.5% if the dihedral angle is larger than 135° . If we use rigid materials for shaded isosceles

triangles, it is necessary to replace those parts by flexible materials or to cut off for a smooth motion.

For the sake of generalization, we can replace the regular octagonal prism to a regular n -gonal prism. We describe vertices of the cover by using parameters r , θ , and a , where r is the radius of the circumscribed circle of a half octagon which is a part of the boundary of the cover part, θ is the angle about the rotation axis, and a is the half length of common edges of the prism and the pyramid. Figure.4.3 shows the 2D pattern and 3D model of the accordion cover structure and Figure.4.4 shows the sample of accordion cover structure based on Figure.4.3.

$$\begin{aligned}
 A_0 &= \left(r - \frac{c}{\sqrt{1+\cos^2\theta}}, d + \frac{c}{\sqrt{1+\cos^2\theta}}, 0 \right) & B_0 &= \left(r, \frac{b}{2}, 0 \right) & C_0 &= \left(r, -\frac{b}{2}, 0 \right) \\
 D_0 &= \left(r - \frac{c}{\sqrt{1+\cos^2\theta}}, -\left(d + \frac{c}{\sqrt{1+\cos^2\theta}} \right), 0 \right) & \theta &= \frac{\pi}{n} & r &= \frac{a}{\sin\theta} \\
 A_{i+1} &= A_i T_{2\theta} & B_{i+1} &= B_i T_{2\theta} & C_{i+1} &= C_i T_{2\theta} & D_{i+1} &= D_i T_{2\theta} \quad i = 0,1,2,3
 \end{aligned} \tag{4.1}$$

where b , c , and d are the side lengths of the prism, and those two truncated pyramids, respectively.

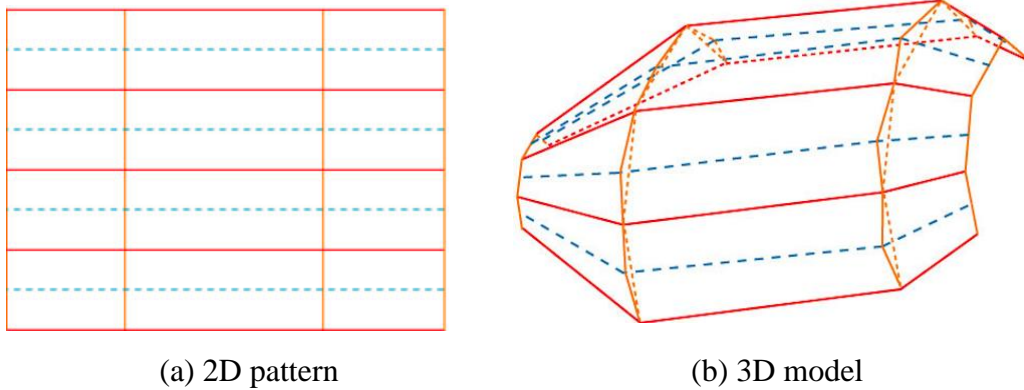


Figure.4.3 The geometrical parameterization of the accordion cover structure.

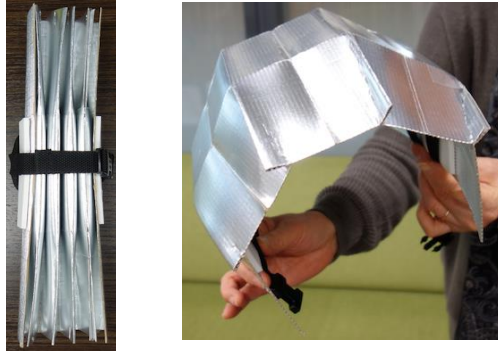


Figure.4.4 The accordion cover structure sample.

4.2.2 The origami structure of the reverse spiral cylindrical structure (RSC)

The reverse spiral cylindrical origami structure (RSC) is decomposed into layers congruent to the side surface of a twisted prism which is flat foldable (see the middle of Figure.4.2). The twisted prism consists of congruent triangles. As shown in Figure.4.3, after N striping, and let $\theta_1, \theta_2 \dots \theta_N$ ($0 \leq \theta_i \leq \pi/2$) be the angles between folding lines (①, ② ...) and X axis, the folded angles Θ_i between X_i axis and X_0 axis are expressed as follows:

$$\begin{aligned} \Theta_1 &= 2\theta_1 \\ \Theta_2 &= 2(\theta_1 - \theta_2) \\ &\vdots \\ \Theta_N &= 2(\theta_1 - \theta_2 + \theta_3 - \dots - \theta_N) \end{aligned} \quad (4.2)$$

Here, N is an even number and satisfies the following equation.

$$\Theta_N = 2\{\theta_1 - \theta_2 + \theta_3 - \dots - \theta_N\} \quad (4.3)$$

That is,

$$\Theta_N = 2\pi \quad (4.4)$$

If the folding angle is determined to satisfy the equation (4.4), the folded plane is closed to form a tubular shape. And then if the 3D structure is made, 3D construct condition is also necessary to be considered. In Figure.4.4, the number of parallelograms is labeled as m , the angle $\angle B_1A_1B_2$ is labeled as α and the angle $\angle B_2A_1A_2$ is labeled as β . It is obvious that the shape of cylindrical folding is determined by α and β only. From equation (4.3) and (4.4), the value of α can be derived as following:

$$\alpha = \pi/n \tag{4.5}$$

When this stripe pattern is completely folded, no matter what the value of β is, the side A_1A_2 should be fixed as one sideline of an m -sided equilateral polygon, and point B_2 should exactly fall in on the circumscribed circle of the m -sides equilateral polygon, as illustrated in Figure.2.12. If β changes, the point of fall of B_2 should be adjusted accordingly, in order to restrict it strictly on the circumscribed circle. It has been found that if a stripe pattern can be folded into a crushable structure, the point of fall of B_2 is limited on the arc R_1R_2 . According to this, the range of β is expressed as equation (4.6) [4.15].

$$\pi/4 - \pi/2m < \beta < \pi/2 - \pi/m \tag{4.6}$$

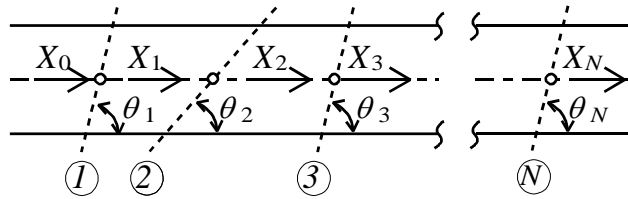


Figure.4.3 Arrangement of folding lines.

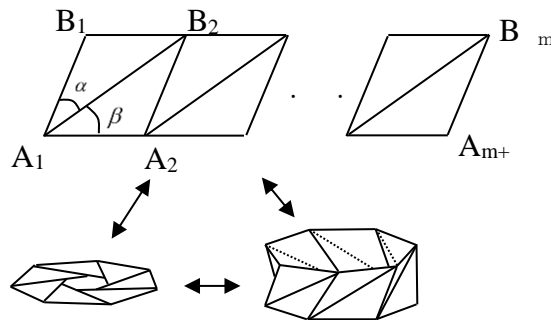


Figure.4.4 Folding procedure of origami structure.

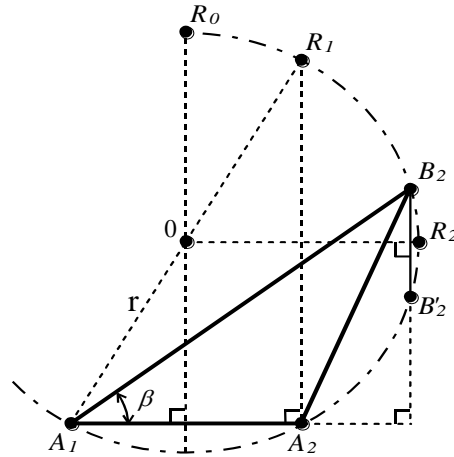


Figure.4.5 The arrangement of triangle A_1A_2B on the circle.

An unfolding of a twisted prism corresponding to one layer of the RSC is a parallelogram decomposed of $2n$ congruent triangles $\Delta A_1A_2B_2, \Delta A_1B_1B_2, \dots, \Delta A_nA_{n+1}B_{n+1}, \Delta A_nB_nB_{n-1}$ as shown in Figure.4.4, where we denote $\angle B_1A_1B_2 = \alpha$ and $\angle B_2A_1A_2 = \beta$. Since the RSC is flat foldable and the boundary edges $A_1A_2, \dots, A_nA_{n+1}$ comprise a regular n -gon, consecutive edges A_1A_2 and A_2A_3 compose the angle $\pi(n-2)/n = \pi - 2\pi/n$, and hence $2\alpha = 2\pi/n$. When the prism is flat-folded, $\Delta A_1A_2B_2$ should be inscribed in the circle with the radius r as shown in Figure.4.5. The orthogonal projection of the vertex B_2' of the twisted prism corresponding to B_2 is the reflected point of B_2 about the line OR_2 where O, R_1, R_2 the center of the circumscribed circle, the symmetric point of A_1 , the point on the arc A_2B_2 such that the line OR_2 is parallel to A_1A_2 , respectively (see Figure.4.5). Since $|B_2'A_1| = |B_2A_1|$, $|B_2'A_2| = |B_2A_2|$, and the height is h , we can lead a simple equation as follows.

$$h^2 = 4r^2 \cos\left(\frac{\pi}{n}\right) \cos\left(\frac{\pi}{n} + \theta\right), \quad 0 < \theta < \frac{\pi}{2} \left(1 - \frac{2}{n}\right) \quad (4.8)$$

4.2.3 The origami structure of honeycomb

The hexagonal honeycomb structure used for the helmet is made of a quadrilateral sheet of paper with the process of accordion folding, cutting some line segments, and gluing some parts [4.16], and it is flat foldable. Since the length of the honeycomb structure gets longer than the

original size under flattening, we should attach it to the cover part carefully for smooth flattening motion. Figure.4.6 shows the 2D pattern and 3D model of the accordion cover structure. Because the structure can be deformed into a line by squashing the hexagons as shown in Figure.4.7, so it is useful that the honeycomb can be produced as a planarization three-dimension.

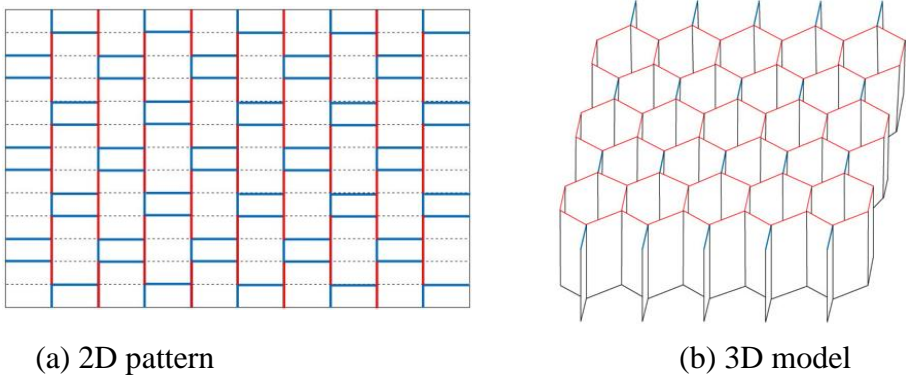


Figure.4.6 2D pattern and 3D model of honeycomb structure.

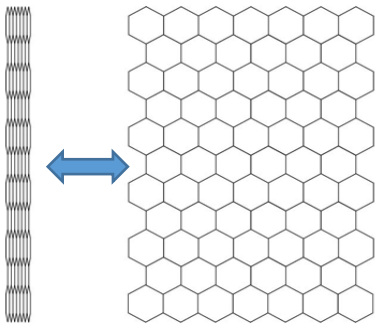


Figure.4.7 Changes of the structure by squashing and expansion the hexagons.

4.3 Numerical simulation for helmet

4.3.1 Analysis method of impact

Figure.4.8 shows the impact experiment system. Complying with the safety standards of the working helmet, the test method is to drop a radius 45mm hemispherical striker of 5kg from 1m in height in a vertical direction and then impacts a human head model covered with a helmet.

Here, considering the efficiency, we seek the countermeasures in analysis simulation by creating the impact analysis mode as shown in Figure.4.9. In the figure, the bottom of head model is completely fixed. When the hemispherical striker falls freely from $h = 1000mm$, the speed reaches the helmet surface is $v = \sqrt{2gh}$ (gravitational acceleration: $g = 9800 mm/s^2$).

The impact analysis starts with the state that the hemispherical striker is in touch with the helmet and the initial speed of the helmet is calculated using above equation. The impact position is the central part of the helmet. And we evaluate the impact force using the top part of head model as the evaluation point. The hemispherical striker is modeled by three-dimensional solid element. The node number is 1027, and the element number is 1036. And the value of its steel material characteristics is shown as follows:

Mass density $2.31 \times 10^{-4} kg/mm^3$

Young's modulus $2.1 \times 10^5 N/mm^2$

Poisson' ratio 0.3

Here, as shown in Figure.4.10, the human head model made by aluminum modeled by three-dimensional solid element. The node number is 2078, and the element number is 10395. And the value of its material characteristics is shown as follows:

Mass density $2.7 \times 10^{-6} kg/mm^3$

Young's modulus $6.89 \times 10^4 N/mm^2$

Poisson' ratio 0.3

In order to put the cover into the box (300mm×150mm×50mm) and the head is wrapped, the dimensions of the cover as shown in Figure.4.2 (a) is $a = 45mm, b = 150mm, c = 83mm, d = 83mm$. The cover model as shown in Figure.4.10 is modeled by using shell element. The node number is 6768, and the element number is 6600.

Figure.4.10 shows the steel RSC structure which is made by hydroforming. RSC has been confirmed that the energy absorption greatly changes by combining the design parameters [4.17~4.19]. Therefore, the optimization was carried out to search the combination of design parameters that maximizes the absorbed energy. If RSC is made by a material with a certain harness, it can be folded state when putting into a box; and it becomes natural length state after taking out. RSC is placed in the middle of the cover. In Figure.4.2 (b), the maximum value of r of RSC is 40mm, and maximum height h of one layer is 20mm which is calculated from equation (4.7). When this RSC structure is put into a box, its height will be reduced to about 60%. Although it is considered that the longer the total height, the beneficial impact energy absorption, since it takes much time to make RSC, 4 layer with one-layer length of 20mm and shortening of 12mm are selected as candidates. The model as shown in Figure.4.9 uses shell

element. The node number is 7772, and the element number is 7990.



Figure.4.8 Impact experiment system.

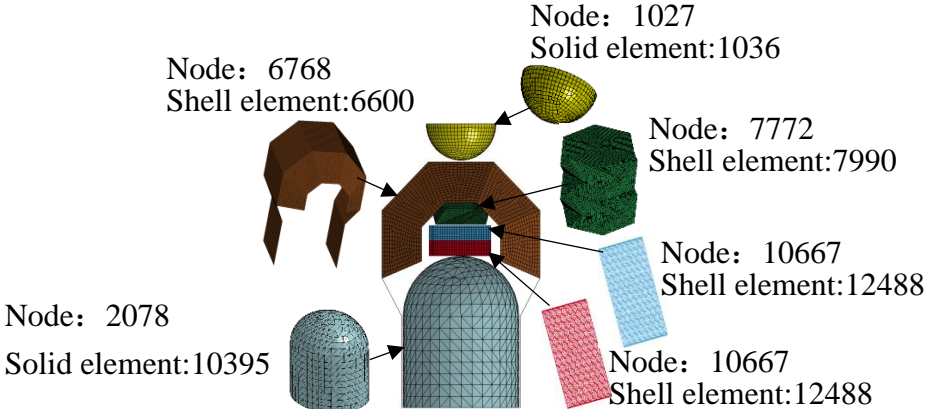


Figure.4.9 Impact analysis model.



Figure.4.10 RSC of steel material made by hydroforming manufacture.

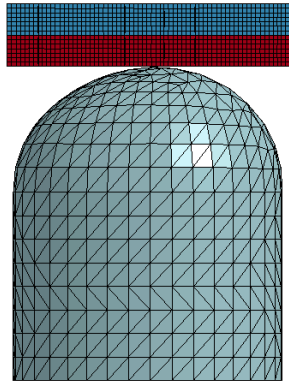


Figure.4.11 The position of Honeycomb and head model.

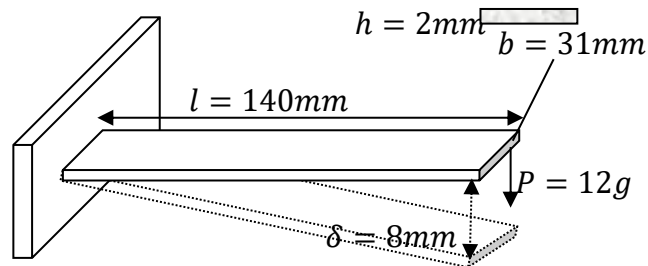


Figure.4.12 Experiment of young's modulus of cardboard.

In addition, in order to put honeycomb structure into a small box, L, H of honeycomb in Figure.4.2 (c) are set to 80mm, 20mm respectively. As shown in Figure.4.11, in order to cover the head, W in Figure.4.2 (c) is 190mm. So the dimension of the honeycomb structure is determined ($L \times W \times H$: 85mm \times 190mm \times 20mm). Furthermore, in order to determine the thickness of honeycomb, when analyzing by changing the thickness of honeycomb to five values of 0.3, 0.5, 0.8, 1.0, 1.2mm, the absorbed energy amount is 5.53, 6.58, 6.31, 5.23, 5.31Nm. Because the absorbed energy is largest when the thickness is 0.5mm, the thickness of honeycomb is set to 0.5mm. As shown in Figure.4.9, the honeycomb structure is also modeled by using shell element. The node number is 21334, and the element number is 24976. Although the cardboard used in helmet has anisotropic characteristic, here we used one of the catalog values (density of 2.569×10^{-7} kg/mm³, Poisson' ratio of 0.34) which have small influence on energy absorption. Here, the Young's modulus in axial direction since the axial crushing is central was obtained by a simple bending experiment shown in Figure.4.12 with the following equation:

$$\begin{aligned}
I &= \frac{bh^3}{12} = \frac{0.031 \times 0.002^3}{12} = 2.0667 \times 10^{-11} \\
E &= \frac{Pl^3}{3I\delta} = \frac{0.12 \times 0.14^3}{3 \times 2.0667 \times 10^{-11} \times 0.008} = 664 \text{MPa}
\end{aligned}
\tag{4.9}$$

4.3.2 Model's setting of optimization

The ratio of the energy absorption amount of honeycomb part, accordion cover part and RSC part of Figure.4.2 is 30%, 4% and 66% respectively. Compared with the accordion cover part and honeycomb part, the RSC part plays an important role in absorbing impact energy. Therefore, the RSC part is optimized to maximize the energy absorption under the condition that the accordion cover part and the cover part are kept above constant values. The Response Surface Method is used as the optimization method as follows:

$$\begin{aligned}
&\text{Design variables: } x = [r, h, n]^T \\
&\text{Constraint condition1: } F = f(x) \leq 4.9 \text{kN} \\
&\text{Constraint condition2: } W \leq 370 \text{g} \\
&\text{Variation range of each design variable:} \\
&30 \text{mm} \leq r \leq 40 \text{mm}, 15 \text{mm} \leq h \leq 20 \text{mm}, 4 \leq n \leq 6
\end{aligned}
\tag{4.10}$$

In this expression, F is the impact force at the top point of head model, W is less than the minimum weight of existing folding helmet. r is the radius of the circumscribed circle of regular polygon. h is the height of one layer of RSC structure. n is the edge number of regular polygon. The variation range of each design variable is shown in expression (4.10). Here, we use Response Surface Method as the optimization technique and L9 orthogonal table to generate sample data. Next, we use these sample data to change the structure model respectively by above equation (4.8), and then from the analysis results, we obtain the impact force and structure weight which are necessary for the optimization calculation. Finally, we organize the one-to-one relationship between sample data and characteristic value, and create the interpolation approximate formula and obtain the optimized solution. Table.4.2 shows the optimal results and Figure.4.13 shows the optimized RSC structure.

Table.4.2 Optimal RSC structure.

	r [mm]	h [mm]	n	Impact force of proposed helmet with optimal RSC structure[kN]	Weight of proposed helmet with optimal RSC structure[g]
Optimal RSC structure	40	20	6	1.91	220

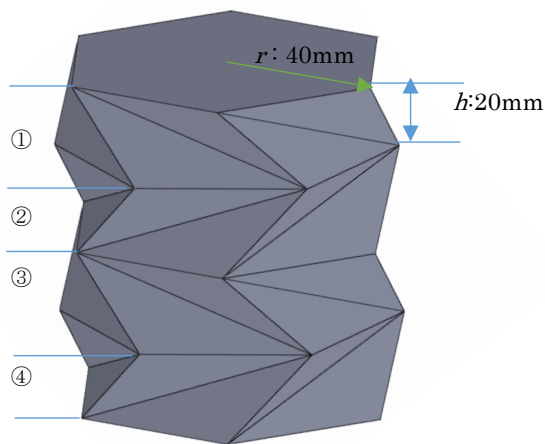


Figure.4.13 Optimal RSC structure.

4.3.3 Characteristic discussions of proposed helmet based on optimal RSC structure

Figure.4.14 shows the energy absorption amount of honeycomb part, accordion cover part and RSC part when the RSC of Figure.4.13 is used in the helmet and this helmet is impacted by the weight falling from 1m. As expected, the cover part is thin, so RSC will start absorbing energy immediately after impacting. The stress wave of impact load of RSC propagated to the honeycomb part, and then honeycomb also starts absorbing energy immediately. In the same figure, the energy absorption amount of the cover part is consistently extremely low. RSC contributes to the impact energy absorption from the early stage of impact, and the energy absorption amount of RSC decreases steadily and becomes close to 0 with the cover part as the energy absorption amount of RSC reaches the maximum. After the energy absorption amount of RSC part reaches maximum, the energy absorption contribution of the honeycomb part in

orange line increases, and the energy absorption amount of RSC part doesn't change until the end. As shown in Figure.4.16, RSC reaches the maximum displacement at 0.018 sec, and after that the springback occurs. On the other hand, the load on the head becoming close to 0 is defined as the impact end, however, the honeycomb part continues to deform after the end of impact 0.04 sec.

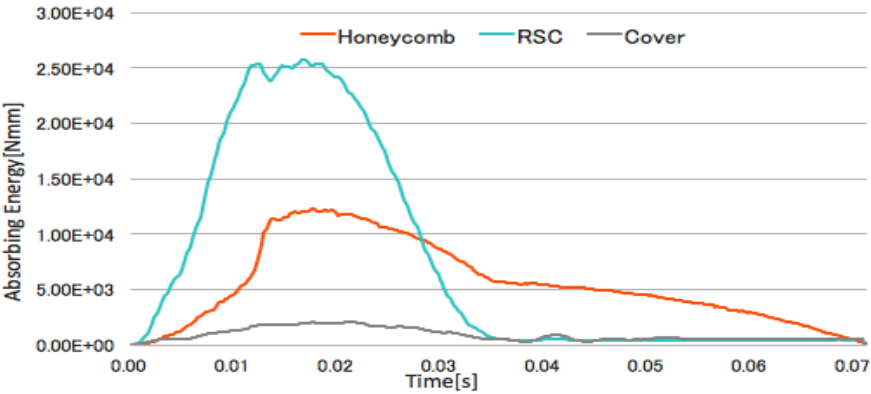


Figure.4.14 Energy of honeycomb, RSC, Cover respectively.

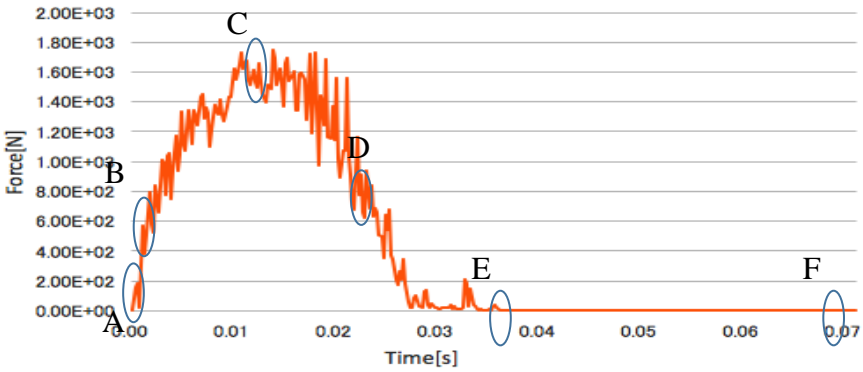
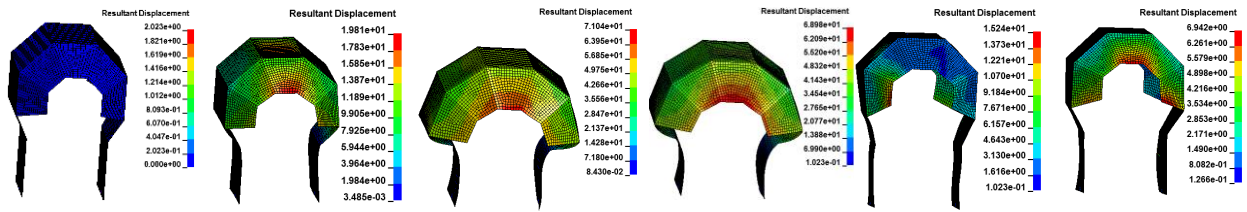
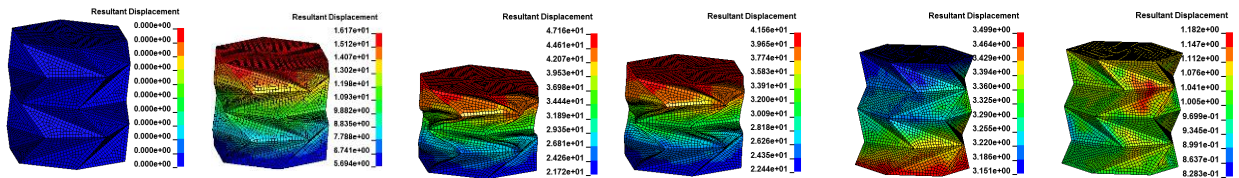


Figure.4.15 Impact force of optimal proposed helmet during impact.



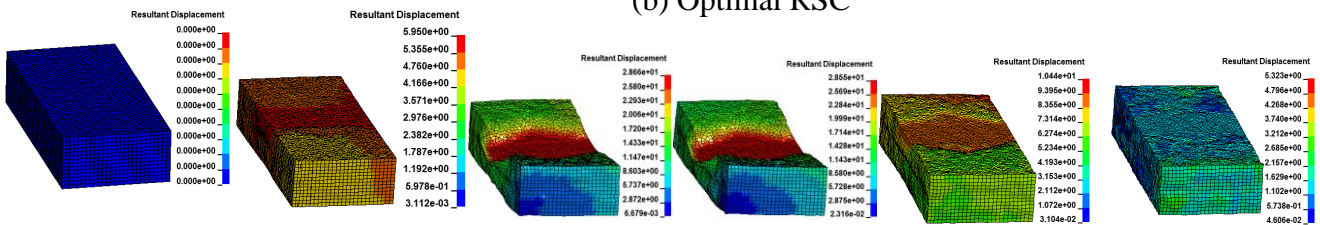
A t=0.000s B t=0.003s C t=0.018s D t=0.025s E t=0.036s F t=0.07s

(a) Cover



A t=0.000s B t=0.003s C t=0.018s D t=0.025s E t=0.036s F t=0.07s

(b) Optimal RSC



A t=0.000s B t=0.003s C t=0.018s D t=0.025s E t=0.036s F t=0.07s

(c) Honeycomb

Figure.4.16 Impact deformations of three parts in helmet during impact process.

The load-displacement curve of the optimal proposed helmet is shown in Figure.4.15. Each impact time in Figure.4.16 (a)~(c) corresponds to the time shown in part A~D of Figure.4.15. Figure.4.16 (a) and Point A in Figure.4.15 show the impact moment and the crush deformation of the cover part and RSC part occur immediately. Along with the crush deformation of the cover part and RSC part, the crush deformation of honeycomb part starts occurring in Point B of Figure.4.15. After reaching the maximum force, the point at which the hemispherical striker has the maximum displacement is Point C in Figure.4.15. That is to say, cover part and RSC part haven't absorbed the total energy. At the last stage of the impact, the start point where the hemispherical striker rebounds and the spring back of the cover part/ RSC part occurs is Point D in Figure.4.15. However, comparing with RSC, the spring back of honeycomb part is still extremely small. The point where the hemispherical striker rebound and doesn't contact to the

helmet is point E in Figure.4.15. The point where the sprig back of honeycomb part reaches the final is point F in Figure.4.15. Looking at the impact behavior in more detail, as shown in Figure.4.16 (a), as the hemispherical striker falls, the cover part not only deforms in axial direction but also spreads sideways. As shown in Figure.4.16 (b), the RSC part folds in an accordion shape and continues buckling deformation along the axial direction. As shown in Figure.4.16 (c), the deformation of the honeycomb part concentrated on the area where the RSC part contacts.

4.4 Experimental results

Even the safety standard of the helmet is that when 5kg drops from 1m, the impact load on the head must be less than 4.9kN, in addition, we continue the experiments of changing the fall height 6 times: 25cm each up from 1m to 2m; 50cm each up from 2m to 3m (1.25m, 1.5m, 1.75m, 2m, 2.5m, 3m). Table.4.3 shows the load-time diagrams of experiments and analyses and Table.4.4 shows the impact peak forces of experiments and analyses. Some sinks are clearly found in the load-time experimental diagrams at the fall height of 1.5m and 3m, however, they are not found in the load-time analysis diagrams. When the honeycomb structure is firmly held against the head, it may become a curved shape along the surface of top head. That is, when the RSC and honeycomb structure are actually made by cardboard material, the adhesiveness strength is not sufficient, so comparing to ideal analysis models, the strength of actual honeycomb cardboard structure becomes weaker.

In order to investigate the cause of sink, we will analyze the following three cases by changing the strength of the RSC part and the honeycomb part. 1) the strength of the RSC is not changed and Young's modulus of the honeycomb is reduced by 5%; 2) Young's modulus of the RSC is reduced by 5% and the strength of the honeycomb is not changed; 3) Young's modulus of the RSC the honeycomb both are reduced by 5%. The load-time diagrams of three cases are shown in Figure.4.17 (Blue line: case 1; Orange line: case2; Grey: case3). In case 1, the sink reproduced, so the actual experimental method is closed to case 1, which indicates in order to secure the strength, it is necessary to develop the adhesion method. In this case, the absorbing energy-time diagram of honeycomb, RSC and cover is shown in Figure.4.17 (b). Comparing the Figure.4.17 (b) with Figure.4.14, the absorbing-time curves of the honeycomb and RSC are clearly different. In Figure.4.17 (b), since the strength of the honeycomb is less than RSC, the honeycomb deforms before the RSC in the initial stage of the impact, so the

absorption energy amount of the honeycomb is relatively higher than the RSC. While the honeycomb continues absorbing energy for a long time even after giving its top energy absorption position to RSC, RSC has become clearly higher after jumping to the top. After that, the energy absorption amount approaches 0 along with the cover. However, for the honeycomb, the energy absorption amount is not 0 even after the load became 0, which is same as in Figure.4.14.

Table.4.3 Force-time curves of different impact heights of origami team-experiment and analysis.

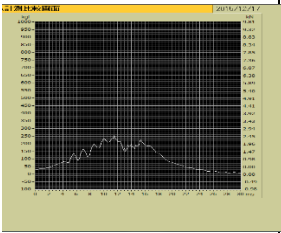
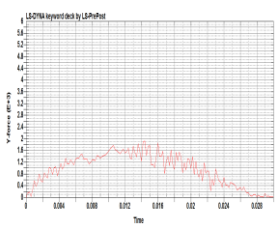
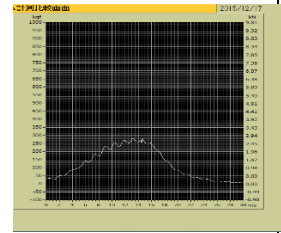
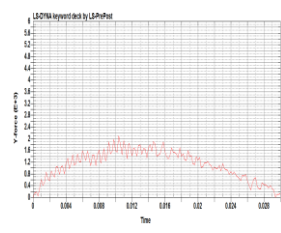
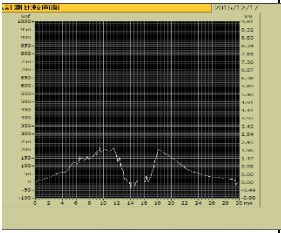
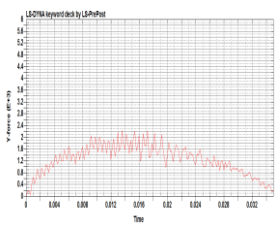
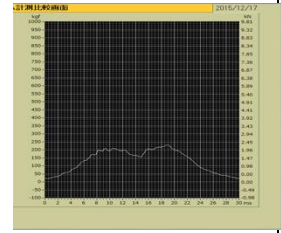
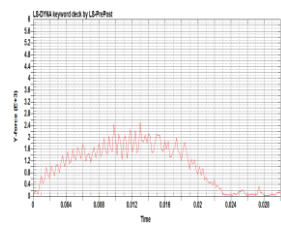
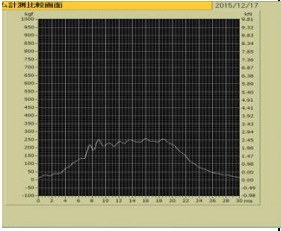
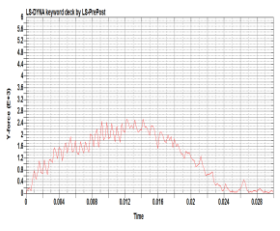
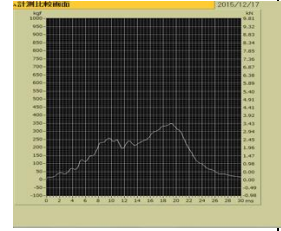
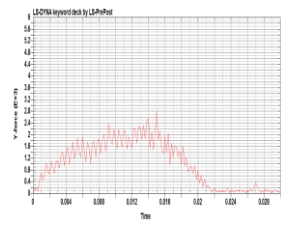
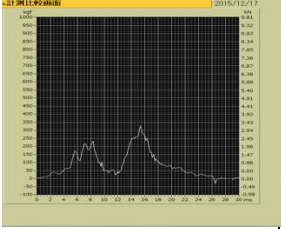
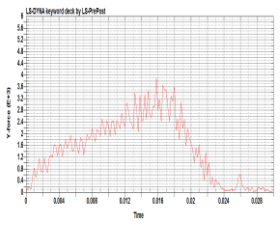
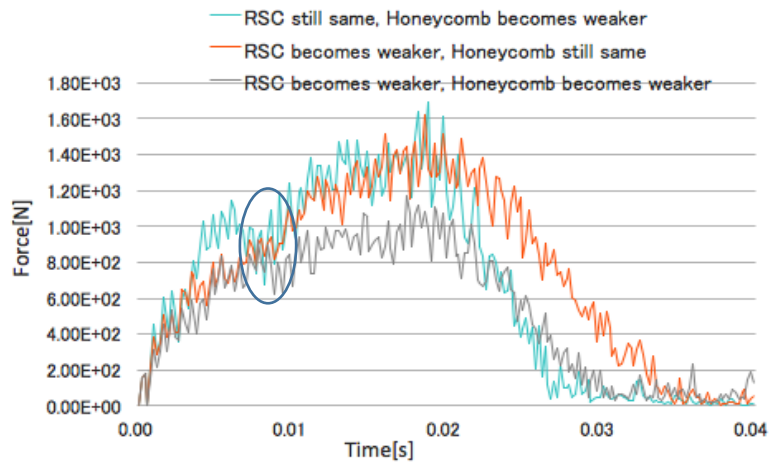
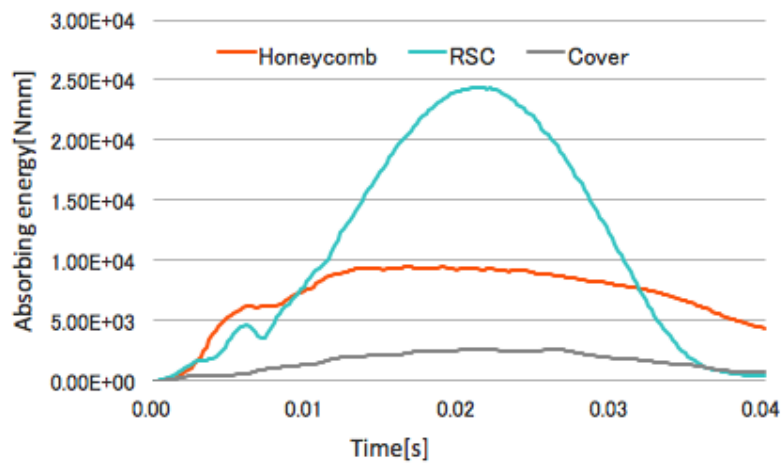
Origami team-experiment	Analysis	Origami team-experiment	Analysis
1m		1.25m	
			
1.5m		1.75m	
			
2m		2.5m	
			
3m			
			

Table.4.4 Peak impact forces of different impact heights of origami team-experiment and analysis.

	1m	1.25m	1.5m	1.75m	2m	2.5m	3m
Origami team-experiment	2.15kN	2.55kN	2.05kN	2.25kN	2.55kN	3.45kN	3.3kN
Analysis	1.91kN	2.3kN	2.13kN	2.4kN	2.61kN	2.8kN	3.5kN



(a)



(b)

Figure.4.17 Hollow phenomenon discussion.

Here, when a helmet is put on, the human operation and manufacture error may influence the impact result, so we from three different impact conditions to investigate the effects as shown in Figure.4.18. Figure.4.18 (a) shows the case that there is 5 inclination angle between the RSC and the honeycomb; Figure.4.18 (b) shows the case that the frictional force between the cover and the head is made 1.2 times as normal; Figure.4.18 (c) shows the case that the RSC and the honeycomb are deviated by 20mm from the center of the helmet. Figure.4.19 shows the load-time curves diagram of 4 impact conditions (three different cases as shown in Figure4.18 and one case of the normal). In Figure.4.19, the orange line is the result of the criteria impact condition for comparison (case 1); the blue line is the result of Figure.4.18 (a) (case 2); the purple line is the result of Figure.4.18 (b) (case 3); the green line is the result of Figure.4.18 (c) (case 4). As shown in Figure.4.19, the load-time curves of case1, case 2 and case 4 are almost same, and the sinks don't occur. When the hemispherical striker reaches the maximum displacement, the impact loads of case 2 and case 4 are bigger than that of case1. This is because that, as shown in Figure.4.16, when the sink doesn't occur, RSC makes large contribution to the energy absorption at the beginning and it also shows that RSC is hardly affected by load direction [4.8]. On the other hand, after the maximum deformation, the contribution of the honeycomb to the energy absorption becomes larger, but the honeycomb is sensitive to the load direction, so the energy absorption amount at this case is smaller than the normal case and the load increases. The load of case 3 is smaller than three other cases. This shows the effect that the helmet is strongly tied with the head by strings. It is reconfirmed that the sink can be obtained through changing the balance of the honeycomb and the RSC.

And then, the ratio of the average load to the maximum is considered to discuss the aim of reducing the maximum load as much as possible. The numerical values are received from Table.4.3 and the average load \bar{F} of theoretical values are calculated by equation (4.11).

$$\bar{F} \times S = \frac{1}{2}mv^2 \quad (4.11)$$

Here, S is the maximum drop displacement of the hemispherical striker. m is the 5kg weight of the hemispherical striker. v is the initial velocity of the hemispherical striker. The results are summarized in Table.4.5. The difference between the experimental values and the numerical values is about 10% because of the uncertain setting factors in the manufacturing as described above, so the accuracy of modeling numerical results is sufficiently satisfactory. However, regarding to reduce the maximum load, it is not sufficient as seen in Table.4.5. The (maximum load/average load) of RSC in the analysis model of Figure.4.1 is close to 1.5, but it is around 2.0 here. And when the energy absorbing member of automobile is made of the current

hollow cross-section structure, the (maximum load/average load) is nearly 2.7 times. So although the effect of RSC has been confirmed, the RSC here may be not optimum design from the point of (maximum load/average load). However, the proposed helmet can be placed into such small box of 300mm×150mm×50mm, and comparing to the lightest helmet of 370g, the proposed helmet has significantly reduced weight to 200g.

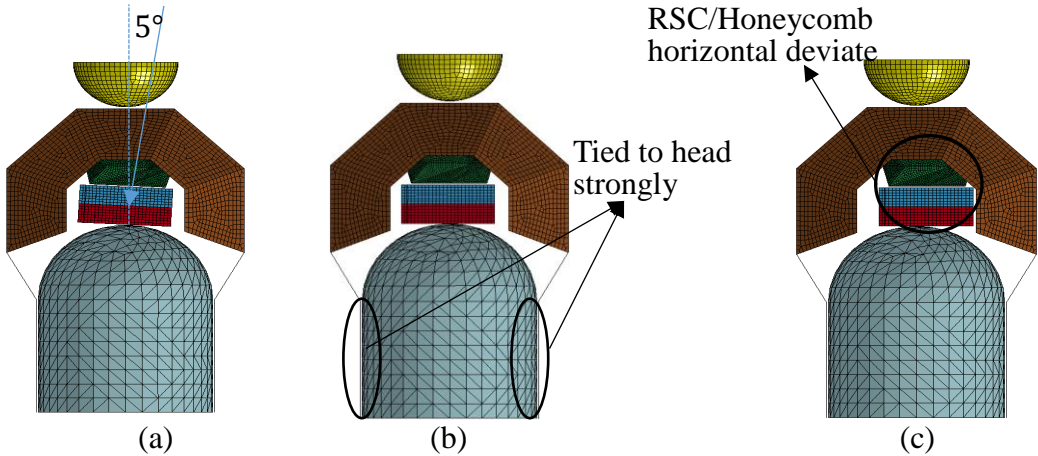


Figure.4.18 Impact condition is changed.

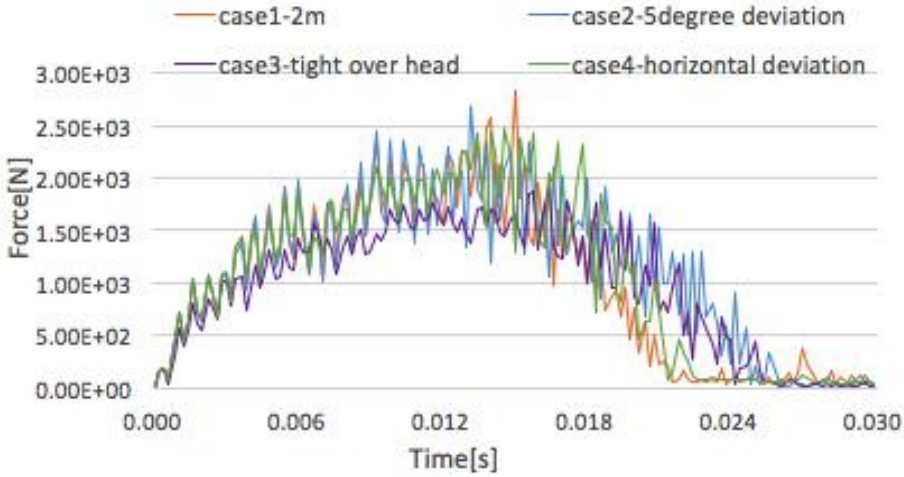


Figure.4.19 Force-time curves of different impact conditions when the impact height is 2m.

Table.4.5 Average forces of different impact heights of analysis and theoretical value.

	1m	1.25m	1.5m	1.75m	2m	2.5m	3m
Experimental \bar{F}	1.19kN	1.32kN	1.13kN	1.23kN	1.33kN	1.66kN	1.59kN
Theoretical value \bar{F} (Max displacement S)	1.02kN (48mm)	1.11kN (54.96mm)	1.2kN (61.13mm)	1.29kN (66.44mm)	1.39kN (71.1mm)	1.5kN (79.88mm)	1.7kN (86.95mm)
F_{Max}/\bar{F} Experimental Value (Numerical Value)	1.8 (1.87)	1.93 (1.89)	1.81 (1.86)	1.83 (1.86)	1.91 (1.88)	2.07 (1.87)	2.07 (2.11)

4.5 Summary

In this Chapter, in order to develop a helmet satisfying the safety standards of working helmet and can be put into the a very small box of 300mm×150mm×50mm, the following results are obtained.

(1) The cardboard is selected as material from the viewpoint of low price and lightweight. If the energy absorbing member of automobile is made of the current hollow cross-section structure, the longer the structure becomes the more prone Euler buckling occurs. But if RSC instead of the current hollow cross-section structure, Euler buckling hardly occurs and the longer it becomes the more advantageous in terms of energy absorption. The cardboard also can work in elastic respects that it becomes a folded state when it is put into a box and it becomes an unfold stat when it is taken out.

(2) The cover part is designed to be put into a small box sufficiently by considering the origami thickness material theory [4.4].

(3) In the experiments, inexplicable results are obtained that the maximum load of the drop height 1.5m is lower than that of the drop height 1m, 1.25m and the maximum load of the drop height 3m is lower than that of the drop height 2m, 2.5m. The cause is due to the manufacturing

defects, etc. and the case that the strength of the honeycomb is relatively smaller than RSC. In this case, the energy absorption-time curve diagram of RSC part and honeycomb part is different from usual, so that a sink occurs in this characteristic curve, in which the maximum load value becomes smaller. For this reason, even the optimization is performed for the RSC only this time, but the combination of RSC part and honeycomb part should be the object of optimum design.

(4) We thought that the ratio of the (maximum load/average load) would be close to 1.0, but it is around 2.0 in fact. So there is also still room for further study from the optimum design.

(5) The sink is caused by the misalignment that the helmet tilts a little when attaching the helmet to the dummy head and even this influence is small, it is confirmed by simulation. The difference between the analysis and the experiment is within 10% in the presence of irregularities in manufacturing and mounting and the validity of the analysis model is confirmed.

(6) Not only the cardboard material and origami structures have showed the effectiveness for the development of a safe, small foldable helmet, but the weight of the helmet is 220g, which is lighter than anyone in Table.4.1. Because there is room for further optimization as mentioned above, we will continue to develop a lighter and more compact helmet.

(7) As described above, origami thickness material theory is applied to the folding design of the cover part, and the RSC structure and honeycomb structure acted to complement each other, and then ideal load-displacement characteristic is obtained and the effectiveness of origami engineering is shown.

Chapter 5 Preventive safety for the self-driving vehicles by deep learning

In autonomous driving level2, it is important to switch from manual to automated driving when the driver's situation is recognized to be dangerous for driving. In order to realize such function, facial expression recognition technology has been included in the autonomous cars. The existing technology is based on facial feature points extraction. In this chapter, we propose to analysis the driver's facial expression by using deep learning technology which learns information directly from data such as images. And the data augmentation method is discussed to solve the problem that the quality of learning depends on the amount of image data.

5.1 Self-driving vehicles and convolutional neural network

At decades ago, in science fiction file, like knight rider, batman, we have seen a lot of self-driving cars. At that time, the autonomous cars are far away from us. But with the development of science and artificial intelligence technology is maturing, those cool autonomous cars are coming to real life. The auto industry has been moving toward more autonomous cars for years. The autonomous car is a vehicle that is capable of sensing its environment and navigating without human input. SAE International (Society of Automotive Engineers) has defined the driving automation classification based on six different levels in 2016: ranging from fully manual to fully automated systems as shown in Figure.5.1. Many major automotive manufactures have pledged to have at least their semi-autonomous systems available by 2020. The self-driving vehicles will bring profound changes. Some of the big ways that self-driving vehicles are summarized as follow:

- ① Millions of people will be rescued every year

According to the report from the World Health Organization, about 1.25 million people worldwide die per year in collisions as shown in Figure.5.2 [5.2], and that number is expected to skyrocket to 2.2 million by 2030. Driverless cars, though, have the potential to dramatically reduce the number of accidents, thus potentially saving millions of lives. According to a study by the Eno Centre for Transportation, if about 90% of cars on American roads were autonomous, the number of accidents would fall from six million a year to 1.3 million and deaths would fall from 33,000 to 11,300. For example, as of February 2016, Google has reported a total of 18 accidents without death involving its self-driving cars since the beginning of testing in 2010.

② Greenhouse gas emissions will be significantly reduced

Because self-driving vehicles are built to optimize efficiency in acceleration, braking, and speed variation, they help increase fuel efficiency and reduce carbon emissions.

③ People will not buy the private car

Industry experts predict self-driving cars will dramatically change consumers' traveling habits, spurring them to trade car ownership for on-demand robo-taxis. One big reason for this is because it will be more cost effective to use a shared fleet car as opposed to your own autonomous vehicle. According to Casualty Actuarial Society by taking a shared, driverless fleet vehicle, the cost per mile could be reduced as much as 80% versus some personally owned vehicles when driven 10,000 miles per year.

④ Traffic congestion will be significantly reduced

Self-driving vehicles will not only help reduce car crashes, they will also likely dramatically reduce traffic congestion. The platooning of vehicles could increase highway capacity by as much as 500%, meaning less traffic and less wasted time.

⑤ People will have more free time

Time spent in traffic is wasted time. But self-driving vehicles would enable drivers to spend that time doing something else instead.

⑥ Mobile ability will be improved

Self-driving vehicles will enable not only the elderly to be mobile, but it will also empower those with disabilities, the unlicensed, and those who do not own a car to travel as well.

⑦ Parking lot will not be needed

The adoption of driverless fleets will mean you never have to search for a parking space again because you will always get dropped off at your desired location.

And even if you do opt to own your own autonomous vehicle, there will still be no need for you to park it because it will locate a space and park itself.

But until now, the automated cars permitted on public roads are not yet fully autonomous. They all require a human driver to take control of the vehicle at moment's notice. So there are

still a number of tough problems that must be resolved before automatic driving technology can achieve the goal that will allow the driver to be full removed from driving. Meanwhile, facial recognition, which has many applications in security and biometrics, has recently been drawn to a new realm of application: driver safety. The driver’s state is known by recognized the driver’s facial expression. The existing facial recognition is using the traditional machine learning technology which learns the facial expression through extracting the facial feature points, for example, OKI’s DMS (Driver Monitoring System), TOYOTA’s vehicle system and so on.

SAE level	Name	Narrative Definition	Execution of Steering and Acceleration/Deceleration	Monitoring of Driving Environment	Fallback Performance of Dynamic Driving Task	System Capability (Driving Modes)
Human driver monitors the driving environment						
0	No Automation	the full-time performance by the human driver of all aspects of the dynamic driving task, even when enhanced by warning or intervention systems	Human driver	Human driver	Human driver	n/a
1	Driver Assistance	the driving mode-specific execution by a driver assistance system of either steering or acceleration/deceleration using information about the driving environment and with the expectation that the human driver perform all remaining aspects of the dynamic driving task	Human driver and system	Human driver	Human driver	Some driving modes
2	Partial Automation	the driving mode-specific execution by one or more driver assistance systems of both steering and acceleration/deceleration using information about the driving environment and with the expectation that the human driver perform all remaining aspects of the dynamic driving task	System	Human driver	Human driver	Some driving modes
Automated driving system ("system") monitors the driving environment						
3	Conditional Automation	the driving mode-specific performance by an automated driving system of all aspects of the dynamic driving task with the expectation that the human driver will respond appropriately to a request to intervene	System	System	Human driver	Some driving modes
4	High Automation	the driving mode-specific performance by an automated driving system of all aspects of the dynamic driving task, even if a human driver does not respond appropriately to a request to intervene	System	System	System	Some driving modes
5	Full Automation	the full-time performance by an automated driving system of all aspects of the dynamic driving task under all roadway and environmental conditions that can be managed by a human driver	System	System	System	All driving modes

Figure.5.1 SAE international’s levels of driving automation for on-road vehicles [5.1].

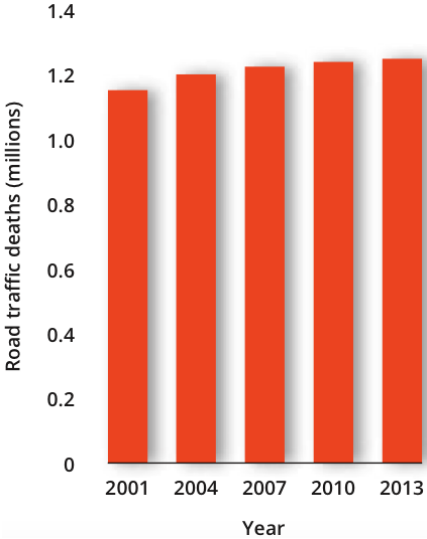


Figure.5.2 Number of road traffic deaths [5.2].

On the other hand, the deep learning proposed by Hinton et al stirs up another study wave in neural networks [5.3]. CNNs (Convolutional Neural Networks) were responsible for major breakthroughs in image classification. CNNs are very similar to ordinary Neural Networks [5.4~5.5]. ConvNet architectures make the explicit assumption that the inputs are images, which is allowed to encode certain properties into the architecture. These then make the forward function more efficient to implement and vastly reduce the amount of parameters in the network. ConvNets transform the original image layer by layer from the original pixel values to the final class scores. Figure.5.3 is one picture in reference [5.6] which shows an simple CNN architecture example. The initial volume stores the raw image pixels (left) and the last volume stores the class scores (right). Each volume of activations along the processing path is shown as a column. A CNN architecture is comprised of a number of convolutional layers, relu layers and pool layers followed by fully connected layers [5.7~5.11]. CNNs have been introduced to the applications such as image classification, face recognition, audio retrieve, electrocardiogram classification, object detection and so on [5.12~5.20].

Considering the superiority in image classification, in order to improve the processing speed and identification accuracy, we proposed to use deep learning which learns information directly from drivers' images for autonomous driving technology instead of existing machine learning which learns information based on facial feature points extraction. Because the deep learning need large amount of image data to study the information for classification [5.21], and in autonomous driving, any drivers' state need to be discussed, however, it is difficult to get so many images like drivers' painful images, so it is necessary to adopt effective method to increase image data from existing facial expression data. In this paper, we used deep learning technology AlexNet and GoogLeNet to analysis facial expression of JFFE database and the data augmentation method to increase useful image data.

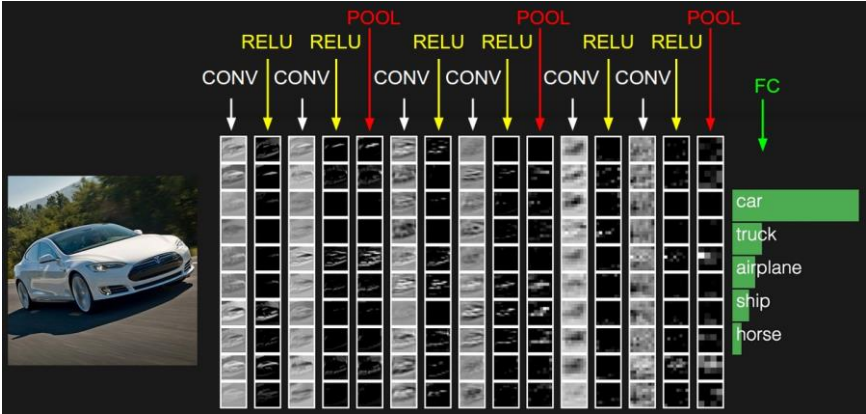


Figure.5.3 The activations of an example CNN in [5.6].

5.2 Analysis method of facial expression recognition

Generally, it is necessary to prepare a large amount of input data as one million unit. However, it is more difficult to prepare so many learning data for driver expression recognition. Therefore, we try to increase the data by image processing as the pre-processing to the learning data and discuss the effectiveness through the quantity of learning data.

5.2.1 Analysis system

Here, the analysis system used to train the image data to analyze the effective method is DIGITS (Deep Learning GPU Training System). DIGITS simplifies common deep learning tasks such as managing data, designing and training neural networks on multi-GPU systems, monitoring performance in real time with advanced visualizations, and selecting the best performing model from the results browser for deployment. DIGITS can be used to rapidly train the highly accurate deep neural network (DNNs) for image classification, segmentation and object detection tasks [5.22, 5.23]. The system material used to analysis the facial expression is shown as following:

CPU : Intel Xeon E5-1650 v4 (3.60 GHz 6 Core 10M Cache)×1;

GPU : NVIDIA GeForce GTX 1080×1;

Memory: 64GB (DDR4-2400 ECC REG 16GB×4);

SSD:240G;

HDD: 1TB;

OS: Ubuntu.

The neural networks used to analysis the facial expression are AlexNet and GoogLeNet.

AlexNet is the name of a convolutional neural network, originally written to run with GPU support, which competed in the ImageNet Large Scale Visual Recognition Challenge in 2012. The network achieved a top-5 error of 15.3% [5.24]. As shown in Figure.5.5, Alexnet contained only 8 layers, first 5 were convolutional layers followed by fully connected layers.

GoogLeNet is a 22 layer CNN and the winner of ILSVRC 2014 with a top 5 error rate of 6.7% [5.25]. GoogLeNet is constructed by stacking inception layers to create a deep convolutional neural network as shown in Figure.5.6.

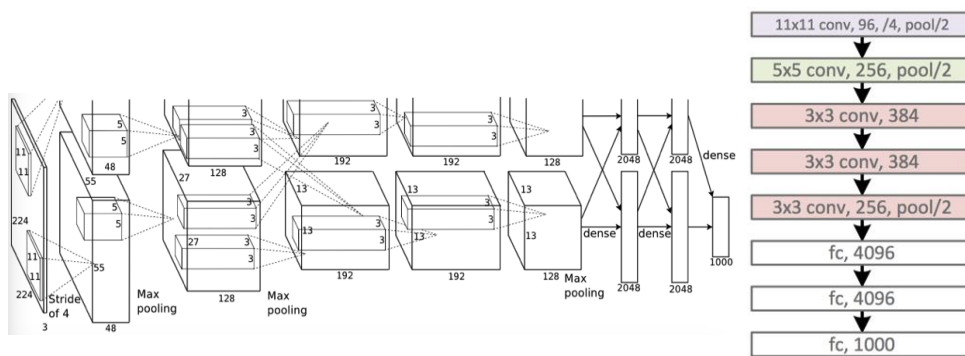


Figure.5.5 The architecture of AlexNet [5.24].

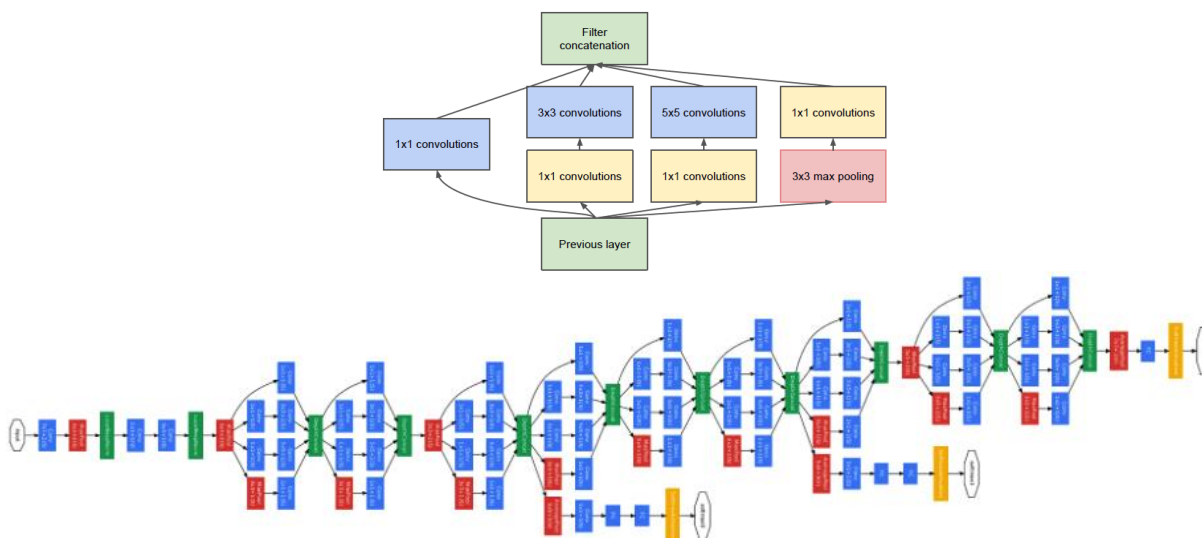


Figure.5.6 The architecture of GoogleNet [5.25].

5.2.2 Analysis database

Here, the image database we use to learn is the Japanese Female Facial Expression (JAFPE) Database [5.26]. The database contains 213 gray images of 10 Japanese female models' 7 facial expressions: 6 basic facial expressions (anger, disgust, fear, happiness, sadness and surprise) and 1 neutral expression as shown in Figure.5.7. The resolution of each image is 256×256 .

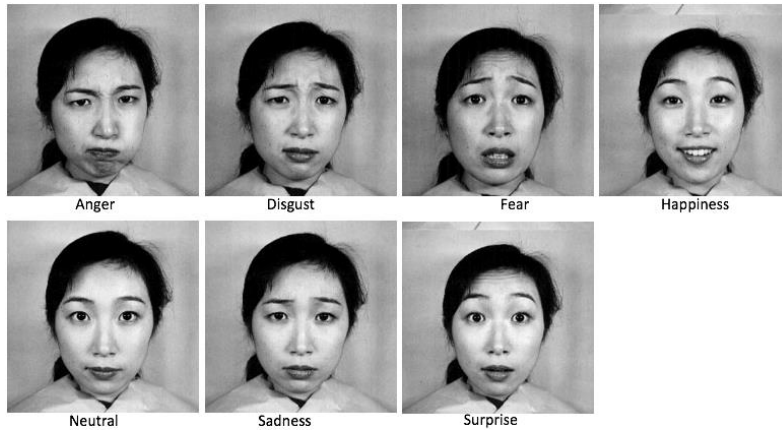


Figure.5.7 Facial expression images of one Japanese female from JAFFE database.

5.2.3 Analysis method of data augmentation

Since deep networks need to be trained on a huge number of training images to achieve satisfactory performance, if the original image data set contains limited training images, it is better to do data augmentation to boost the performance [5.24].

To improve prediction rate, two ways are proposed to do data augmentation. The first form of data augmentation consists of generating image translations as shown in Figure.5.8. The rotation angle to be added to one image is mirror reversal, 90-degree left rotation, 90-degree right rotation and 180-degree rotation. The second form of data augmentation consists of altering the intensities in training images as shown in Figure.5.9. The amount of uniform distribution noise to be added to one image is 1%, 5%, 10%, 20%, 30%, 40% and 50%. As shown in Table.5.1, the original images without image processing is 213, the number increases in stages after doing each image processing to each image.

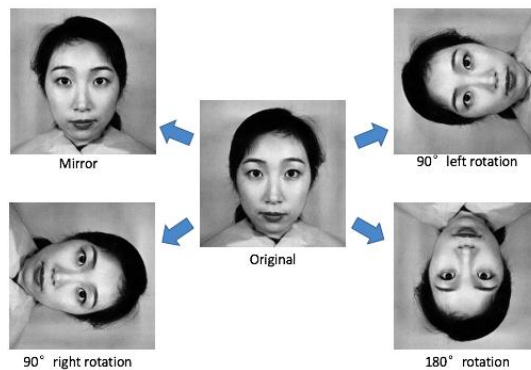


Figure.5.8 A sample of translation in training image.

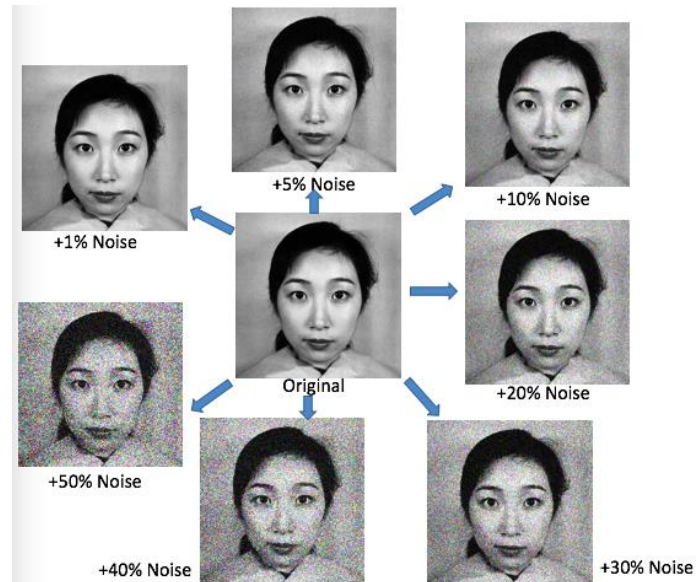


Figure.5.9 A sample of adding noise in training image.

Table.5.1 Combination of image processing with the input data set.

Data number	Method to get more input data
213	Original
426	Original + Mirror inverted (Mirror)
426	Original + 90-degree to left (L90)
426	Original + 90-degree to right (R90)
426	Original + 180-degree rotation (180)
1065	Original + Mirror + L90 + R90 + 180
426	Original + 1% noise add (1%N)
426	Original + 5% noise add (5%N)
426	Original + 10% noise add (10%N)
426	Original + 20% noise add (20%N)
426	Original + 30% noise add (30%N)
426	Original + 40% noise add (40%N)
426	Original + 50% noise add (50%N)
1704	Original + 1%N + 5%N + 10%N + 20%N + 30%N + 40%N + 50%N

5.2.4 Learning convergence time

In this system, based on the teacher data, each parameter is updated from the identification error. In order to reduce the errors, it is necessary to update parameters calculation iteratively by Stochastic Gradient Descent method. As shown in Figure.5.4, when the repetition time is less than 100, the train error values are high for both AlexNet and GoogLeNet; when the repetition time reaches 300, the learning converges with the prediction rate is being stable, while the train errors and valuable errors are being low; when the repetition time is more than 400, comparing to AlexNet , GoogLeNet keeps a good state.

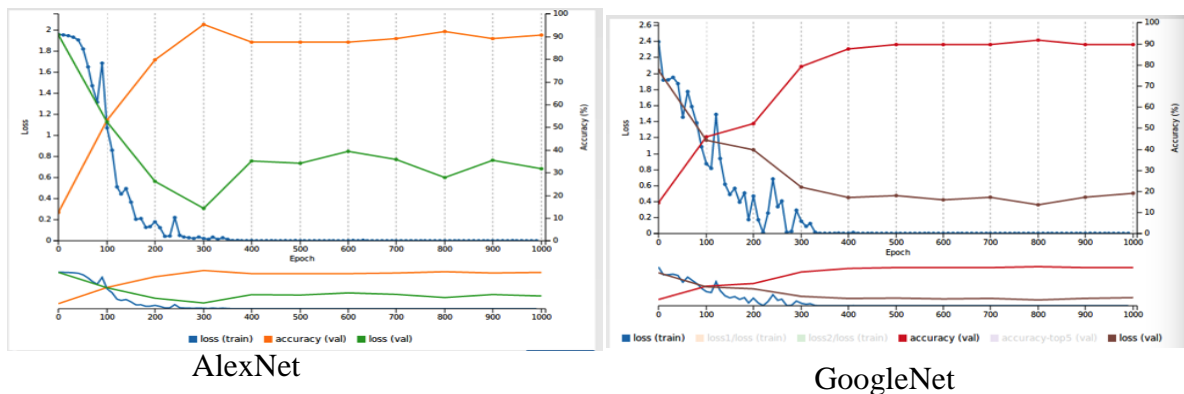


Figure.5.4 The results of the convergence calculation in DIGITS.

5.3 Analysis results

The image processing of generating image translations and altering the intensities is added to the original images to increase input data and learning is carried out using two kinds of CNNs (GoogLeNet and AlexNet). Figure.5.5 shows prediction rate results of input data the original image data 213 images is processed by above-described 4 types of image translations. Figure.5.6 shows prediction rate results of input data the original image data 213 images is processed by above-described 7 types of image intensities.

As shown in Figure.5.5, by the data processing method of generating image translations, the prediction accuracy of learning by AlexNet is higher than by GoogLeNet. Whether GoogLeNet or AlexNet, it is shown that the prediction accuracy of input learning data of combination of the original images and each image adding mirror inversion (Original+Mirror) is highest. The prediction results of doing the data processing by other 3 types of angle rotation (Original+L90,

Original+R90 and Original+180) are lower, and it is thought that in the network a face cannot be learned when the parts of face rotate. The data number of combination of the original data and data from doing all image translations (Original+Mirror+L90+R90+180) is 5 times than that of the original data, but from the result, just simply increasing the number of learning data does not improve the prediction accuracy.

As shown in Figure.5.6, by the data processing method of altering the intensities, the prediction accuracies of learning by AlexNet and GoogLeNet are almost same. It is shows that altering the intensities effectively improve the prediction accuracy. To increase data number simply by combination of the processed data (Original + 1%N + 5%N + 10%N + 20%N + 30%N + 40%N + 50%N) also receives improved prediction accuracy. The specific amount noise adding to image can receive best prediction accuracy needs to continue to study.

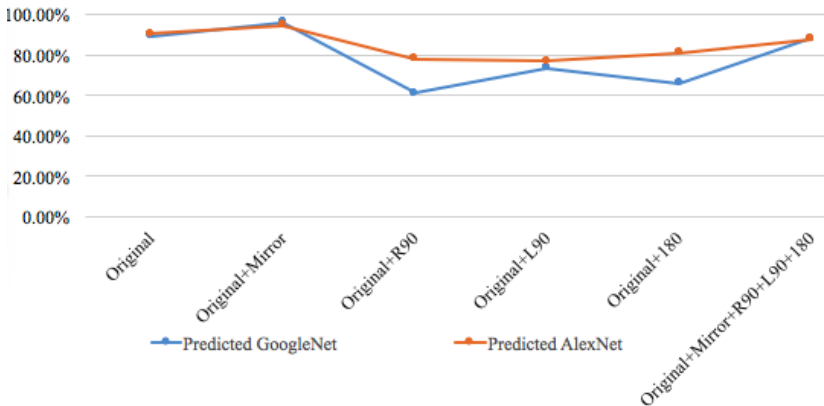


Figure.5.5 The prediction rates of different image translations by GoogLeNet and AlexNet.

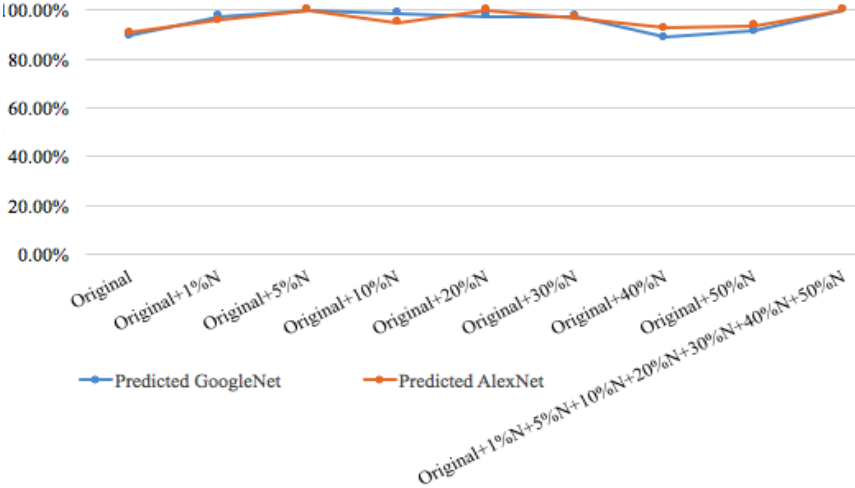


Figure.5.6 The prediction rates of different image intensities by GoogLeNet and AlexNet.

5.4 Summary

Deep learning which inputs images directly without read the features gets public attention. Applying deep learning to the research of facial expression recognition for self-driving, the effectiveness is discussed and the following results are obtained.

(1) As compensation for simplicity of inputting images only, a large amount of input data is required for deep learning, but it is not easy to gather so large amount of input data in general. Therefore, there are two data processing methods of generating image translations (mirror inversion, 90-degree left rotation, 90-degree right rotation and 180-degree rotation) and altering the intensities (1%, 5%, 10%, 20%, 30%, 40% and 50% uniform noise added) applied to increase input learning data for facial expression recognition. The learning and prediction discussion are carried out to show the effectiveness of these two data processing methods.

(2) The learning and prediction is studied by using AlexNet which has the top recognition performance in ILSVRC 2012 and GoogLeNet which has the top recognition performance in ILSVRC 2014. In these two CNNs, to increase input data by data processing method of mirror inversion receives higher prediction accuracy.

(3) By using data processing method of altering the intensities, regardless of the noise adding amount, the prediction accuracy results from both CNNs shows the usability of this data processing method of altering the intensities.

Chapter 6 Conclusions and future works

6.1 Conclusions

In recent years, due to the growing concerns over the environmental problem and safety issue, there is rapid changeover from gasoline engine power vehicles to electric vehicles and self-driving vehicles. This thesis presents the studies on the collision characteristics for electric vehicles from the viewpoint of the crash energy absorption and self-driving vehicles from the viewpoint of image recognition based on deep learning. On the basis of the experience of the crash energy absorption study, a foldable safety helmet is invented by using energy-absorbing origami structures and won the strongest helmet competition hold by NHK program “X-technology-SUGOWAZA”.

The concluding remarks of each chapter of this thesis are summarized as follows.

Chapter 1 is an introduction. This chapter introduces the background of this thesis, including the importance of energy-absorbing structures, the superiority of origami engineering and the development of collision avoidance system. This chapter describes collision characteristics for the electrical vehicles, self-driving vehicles and daily necessities from energy-absorbing member design to driver’s facial expression recognition. And finally describes the purpose and research contents of this thesis.

Chapter 2 is crash energy absorbing members of the lightweight electrical vehicles by using truss core panel. In the electric vehicle, when the mechanical power transmission systems such as propeller shafts or piping routes are unnecessary and the front floor will be in flat shape, the crush strength of the flat structure becomes weaker. On the other hand, TCP has better aspects in bending stiffness and in shear stiffness, but when TCP receives a lateral impact load, the vertical bend occurs. In order to solve this problem, the insert members on the both side are proposed into the TCP structure and the proposed structure is optimized to seek the maximum crash energy absorption. And then, in order to verify the superiority of the proposed lightweight

structure based on TCP, the structure based on HCP is optimized and used to be compared. According to the simulation results, the structure based on TCP is capable of absorbing energy more than the one based on HCP at the same mass of structures.

Chapter 3 is crash energy absorbing members of the electrical vehicles by using pairing origami structure. In the electric vehicle, if the existing box-type is still used as the side member, there is a problem that though this side member has ideal collapse mode without Euler buckling, it cannot be collapsed more than 70% of its length because of its bulk and moreover, its initial peak load is sometimes too high. To solve these problems, two pairing origami structures have been proposed; one is Tachi-Miura polyhedron (TMP), which has been studied extensively by the folding behavior for mechanical energy, and another is Nojima polyhedron (NP), which is invented from a hexagonal origami shape independently. The geometrical characteristics of two pairing structures are discussed by parameters for the first time. In order to investigate the energy absorption performance of TMP and NP, these pairing structures are characterized by extracting geometrical parameters. By using the optimization method of Response Surface Methodology, the shapes of TMP and NP are numerically optimized respectively to seek the maximum energy absorption. As a result, in the comparison of TMP and NP, relative to the mirror symmetry structure of NP, there is a big vertical bend in TMP during the collapse deformation process. So the energy absorption amount of NP is more than that of TMP. In the comparison of NP and existing box-type side member, because NP regularly deforms from the front to the end and the deformations reach 89%, NP has relatively better energy absorption characteristic and the very smooth force is received. In the comparison of NP and RSC, even the energy absorption amount of RSC is more than that of NP, but NP has the advantage of manufacture cost. So an excellent energy absorbing member based on NP is the future challenge.

Chapter 4 is an application of vehicle crash technology and origami structures to daily necessities. The goal of safety helmet is absorbing the impact energy and decreasing the impact force as much as possible, which is similar to the crash analysis of strength member of vehicle. In order to seek the requirements of being saved compactly and satisfying the safety performance, three type origami structures (accordion cover structure, RSC structure and honeycomb structure) are introduced to the design of the safety helmet. By the methods of geometric analysis, impact simulation analysis and structural optimization, the combination helmet structure composed of cover structure, RSC structure and honeycomb structure is improved. The proposed helmet made of cardboard totally satisfies the safety standards of the working helmet with lightweight and can be put into a very small box of 300mm (length) \times 150mm (width) \times 50mm (height), where the helmet could be kept to save space. The validity of the numerical analysis models is confirmed by discussing the differences between the

analysis and the experiment, where the error is within 10% in the presence of irregularities in manufacturing and mounting.

Chapter 5 is preventive safety for self-driving vehicles by deep learning. From the previous chapters, the collision characteristics for self-driving and electric vehicles have been studied from the design of car component--energy-absorbing structure by using origami structures to improve the safety of protecting driver and passengers. Furthermore, from the perspective of preventing collision, the advanced driving assistant system (ADAS) has been practically applied in self-driving vehicles to help the driver in the driving process. In ADAS, the driver monitoring system (DMS) uses sensors to monitor driver attentiveness. In DMS, the driver's facial recognition is fundamental. Considering the superiority of CNN in image classification, in order to improve the processing speed and identification accuracy, the deep learning which learns information directly from drivers' images is used to detect drivers' states instead of the machine learning which learns information based on facial feature points extraction. Because the deep learning needs large amount of image data to study the information for classification, however, it is difficult to get so many images of drivers in the painful case or other dangerous cases. So an effective processing method is developed to increase image data from existing facial expression data. The proposed method is training by the AlexNet and GoogleNet in the DIGITS system and shows the feasibility of improving the accuracy of facial expression recognition.

6.2 Future works

6.2.1 Improvement of the foldable safety helmet

In chapter 4, the proposed foldable safety helmet has been confirmed that it meets the foldability and safety. From the prospect of application of foldable safety helmet and to avoid the instability of the proposed helmet while wearing it, the foldable safety helmet is considered to improve by removing the RSC and adding the urethane part as shown in Figure.6.1. At the current stage, this safety helmet also can satisfy the requirements of the proposed foldable safety in chapter 4. If used as the bicycle helmet, there are several tasks to be solved in the following.

(1) To simulate the impact by FEM under some impact configurations mentioned in Figure.6.2 [6.1].

(2) To perform the numerical impact simulation to compute the Head Injury Criterion (HIC)

of the following equation to validate the helmet.

$$HIC = \left\{ \left[\frac{1}{t_2 - t_1} \int_{t_1}^{t_2} a(t) dt \right]^{2.5} (t_2 - t_1) \right\}_{max} \tag{6.1}$$

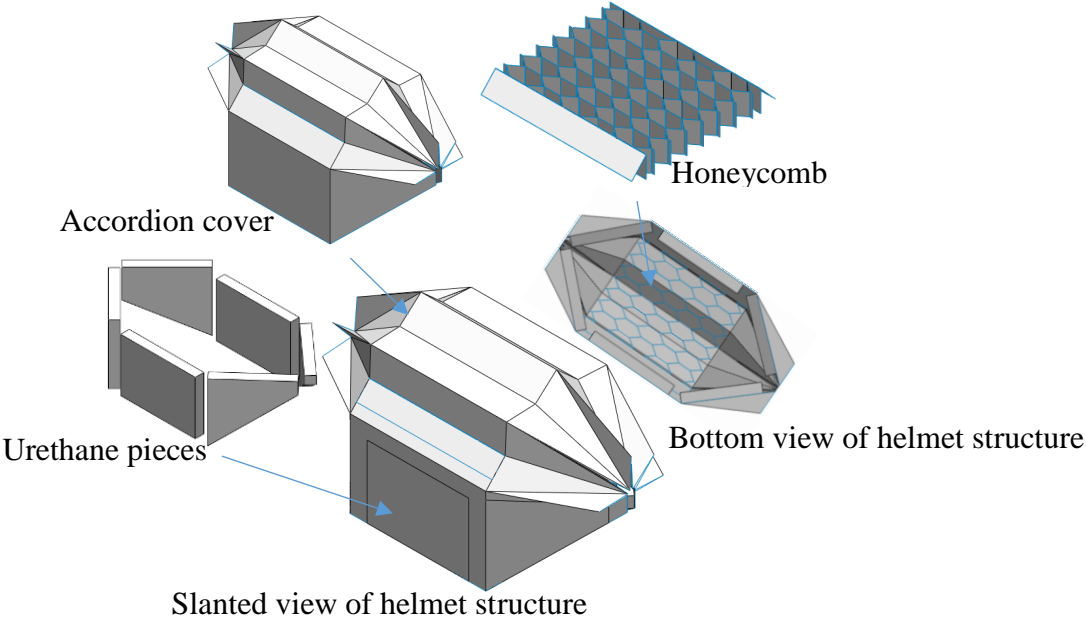


Figure.6.1 The structure of helmet.

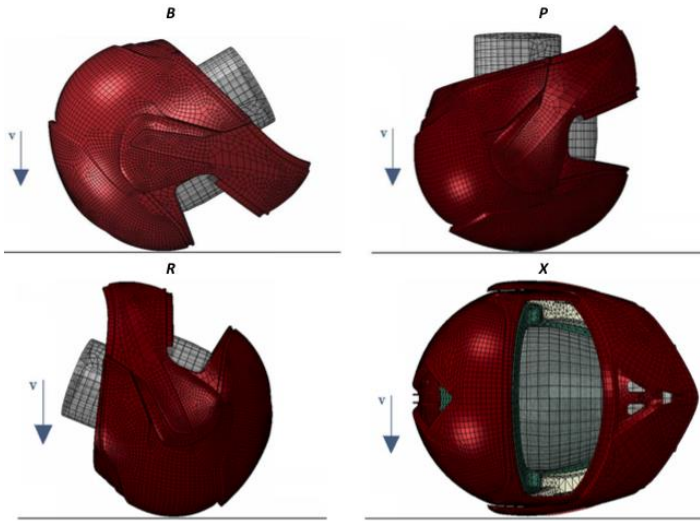


Figure.6.2 The impact configurations mentioned in [6.1].

6.2.2 Improvement of the image recognition for automatic driving

In chapter 5, two data processing methods are proposed to increase the number of learning data for improving prediction accuracy. This is just a shallow attempt to use deep learning into image recognition for automatic driving, therefore, there are still many shortages needed to be completed.

Firstly, in order to confirm the applicability of the proposed data processing method, one widely applicable database is introduced into test: Extended Cohn-Kanada Dataset (CK+).

CK+ includes 593 image sequences of 210 adults. Participants are from 18 to 50 years of age, 69% female, 81%, Euro-American, 13% Afro-American, and 6% other groups. Image sequences for frontal views and 30-degree views are digitized into either 640x490 or 640x480 pixel arrays with 8-bit gray-scale or 24-bit color values [6.2]. An inventory of the AUs coded in the CK+ database is given in Table.6.1 and one sample described by AUs as shown in Figure.6.3.

Table.6.1 Frequency of AUs coded by manual FACS coders on the CK+ database [6.3].

AU	Name	AU	Name	AU	Name
1	Inner Brow Raiser	13	Cheek Puller	25	Lips Part
2	Outer Brow Raiser	14	Dimpler	26	Jaw Drop
4	Brow Lowerer	15	Lip Corner Depressor	27	Mouth Stretch
5	Upper Lip Raiser	16	Lower Lip Depressor	28	Lip Suck
6	Cheek Raiser	17	Chin Raiser	29	Jaw Thrust
7	Lid Tightener	18	Lip Puckerer	31	Jaw Clencher
9	Nose Wrinkler	20	Lip Stretcher	34	Cheek Puff
10	Upper Lip Raiser	21	Neck Tightener	38	Nostril Dilator
11	Nasolabial Deepener	23	Lip Tightener	39	Nostril Compressor
12	Lip Corner Puller	24	Lip Pressor	43	Eyes Closed




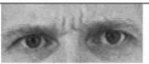











<i>NEUTRAL</i>	AU 1	AU 2	AU 4	AU 5
				
Eyes, brow, and cheek are relaxed.	Inner portion of the brows is raised.	Outer portion of the brows is raised.	Brows lowered and drawn together	Upper eyelids are raised.
AU 6	AU 7	AU 1+2	AU 1+4	AU 4+5
				
Cheeks are raised.	Lower eyelids are raised.	Inner and outer portions of the brows are raised.	Medial portion of the brows is raised and pulled together.	Brows lowered and drawn together and upper eyelids are raised.
AU 1+2+4	AU 1+2+5	AU 1+6	AU 6+7	AU 1+2+5+6+7
				
Brows are pulled together and upward.	Brows and upper eyelids are raised.	Inner portion of brows and cheeks are raised.	Lower eyelids cheeks are raised.	Brows, eyelids, and cheeks are raised.

Figure.6.3 Describing facial expression by action units (AUs).

Secondly, due to different illuminating conditions in outdoor environments, there are cases when the shadows in the face of the driver, the DMS is developed by using correction method for shadows in the face and deep holographic neural networks (D-HNN) for modeling the normal/abnormal driver's statuses under different lighting conditions and driver's appearances.

The correction method proposed in research [6.4] is more efficient than traditional methods if the shadow is less than 40% of the face. Figure.6.4 shows the histogram of the lightness in face. The shadow part of face is defined as the pixels. All pixels in the shadow part are shifted towards the region between H_a (50%) and H_b (80% of the cumulative distribution).

The fuzzy-quantized holographic neural network (FQHNN) is used to add explanations about the classification made by deep neural networks about the driver's driving statuses. Figure.6.5 shows the architecture of proposed FQHNN. A novel fuzzy quantification module (lower part) is added to the HNN (upper part) in order to increase the interpretability of HNN models [6.5].

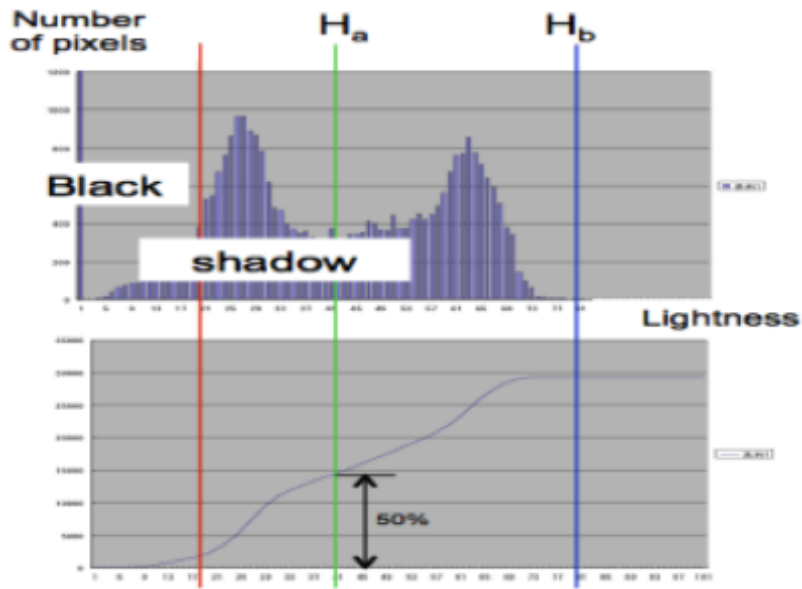


Figure.6.4 Definition of the shadow part of face.

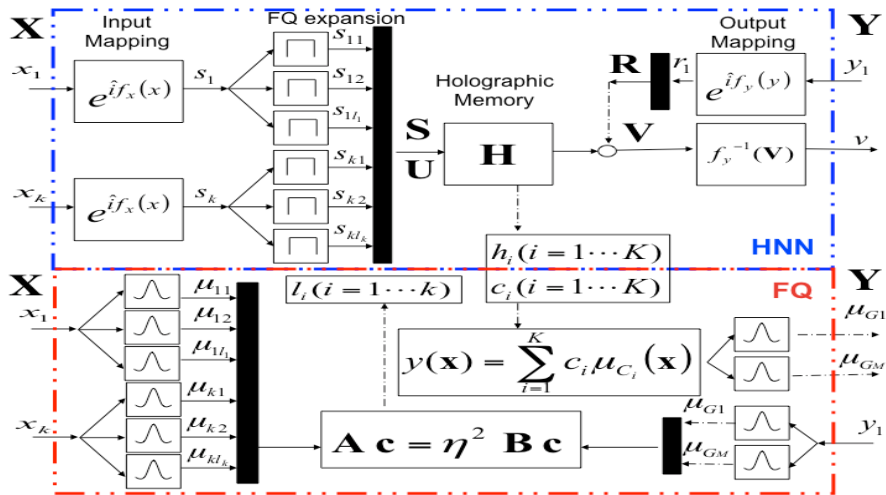


Figure.6.5 The architecture of the Fuzzy-Quantized Holographic Neural Network (FQHNN).

Bibliography

Chapter 1

- [1.1] Yoshizawa, S., “Atarashii Origami Geijutsu.” Tokyo:Origami Geijutsusha(1954).
- [1.2] Robert, L., Tree Maker, <http://www.langorigami.com/science/treemaker/treemaker5.php4>
- [1.3] <http://sciencelinks.jp/content/view/656/260/> (English)
<http://sciencelinks.jp/fr/content/view/592/260/> (French)
<http://sciencelinks.jp/ch/content/view/619/261/> (Chinese)
- [1.4] Nojima, T. and Hagiwara, I., “Geometrical Mathematics for Origami and Its Industrial Application.” (2012), pp.60-77, Kyoritsu Publisher.
- [1.5] Ishida, S., Nojima, T. and Hagiwara I., “Conformal Transformation and Application to Origami Designing.” Transactions of the JSME C, Vol.79, No.801(2013), pp.336-344.
- [1.6] Saito, K., Nomura, S., Yamamoto, S., Niiyama R. and Okabe, Yoji. “Investigation of hindwing folding in ladybird beetles by artificial elytron transplantation and microcomputed tomography.” Proceedings of the National Academy of Sciences of the United States of America, Vol.114, No.22(2017), doi: 10.1073/pnas.1620612114.
- [1.7] Mitani, J., “A design method for 3D Origami based on rotational sweep.” Computer Aided Design Applications 6(1):69–79(2009).
- [1.8] Miura. K., “Proposition of pseudo-cylindrical concave polyhedral shells.” In Proceedings of IASS Symposium on Folded Plates and Prismatic Structures, (1970).
- [1.9] Tachi. T., “Geometric Considerations for the Design of Rigid Origami Structures.” In Proceedings of the International Association for Shell and Spatial Structures (IASS) Symposium, (2010).
- [1.10] Gattas, J.M., Wu W. and You Z., “Miura-Base Rigid Origami: Parameterization of First-Level Derivative and Piecewise Geometries.” Journal of Mechanical Design, Vol.135(2013), 111011-1.
- [1.11] Hull, T., “Project Origami: Activities for Exploring Mathematics”, AK Peters/CRC Press, pp.229-235(2006).

- [1.12] Sreinu, I., and Whiteley W. “Single-vertex Origami and Spherical Expansive Motions.” Lecture Notes in Computer Science, No.3742, pp.161-173(2005).
- [1.13] Belcastro, S., and Hull, T., “Modeling the Folding of paper into Three Dimensions Using Affine Transformations.” Linear Algebra Appl, No.348, pp.273-282(2002) (doi:10.1016/S0024-3795(01)00608-5).
- [1.14] Tachi, T., “One-DOF Cylindrical Deployable Structures with Rigid Quadrilateral Panels.” International Association for Shell and Spatial Structures Symposium (IASS), pp. 2295–2305(2009).
- [1.15] Tachi, T., “Freeform Rigid-Foldable Structure Using Bidirectionally Flat-Foldable Planar Quadrilateral Mesh,” Advances in Architectural Geometry 2010, Springer, pp.87–102(2010).
- [1.16] Wang, K. F., and Chen, Y., 2010, “Rigid Origami to Fold a Flat Paper Into a Patterned Cylinder,” Origami 5: Fifth International Meeting of Origami Sci-ence, Mathematics, and Education, CRC Press (2010).
- [1.17] Balkcom, D.J., and Mason, M.T, Robotic origami folding. Int. J. Robot. No.27, pp.613–627 (2008) (doi:10.1177/0278364908090235).
- [1.18] Romero, J.A., Diago, L.A., Nara, C. and Hagiwara, I., “Norigami Folding Machines for 3D Complex Shape.” at Proceeding of ASME 2016 International Design Engineering Technical Conferences & Computers and Information in Engineering Conference, No.DETC2016-60580 (2016).
- [1.19] Liu, S., Lv, W., Chen Y. and Lu, G., “Deployable Prismatic Structures with Rigid Origami Patterns.” J. Mechanisms Robotics 8(3), No. JMR-15-1129(2015), doi: 10.1115/1.4031953.
- [1.20] Trautz, M., and Kunstler, A., “Deployable Folded Plate Structures: Folding Patterns Based on 4-Fold-Mechanism Using Stiff Plates.” Proceedings of the International Association for Shell and Spatial Structures (IASS) Symposium (2009).
- [1.21] Guest, S., and Pellegrino, S., “Inextensional Wrapping of Flat Membranes.” Proceedings of the First International Seminar on Structural Morphology, pp. 203–215(1992).
- [1.22] Nara, C., Hagiwara, I., Yang Y., and Chen X., “Flat-foldable Boxes of Thick Panels–Hinges and Supporters.” at Proceedings of the ASME 2017 International Design Engineering Technical Conferences & Computers and Information in Engineering Conference (2017).
- [1.23] Tachi, T., “Rigid Foldable Thick Origami.” Origami 5: Fifth International Meeting of Origami Science, Mathematics, and Education (2011).
- [1.24] Jones, N., “Dynamic and Static Axial Crushing of Axially Stiffened Square Tubes.” at Proceeding of the Institution of mechanical engineering, Vol.204, pp.293-310 (1990).
- [1.25] Yamashita, M., Gotoh, M., Takahashi T., and Sawairi Y., “Axial Crush of Strengthening Structural Members with Various Hat-Shaped Cross-Sections (1st Report, Impact Test by a Drop Hammer).” Transactions of the Japan Society of Mechanical Engineers A, Vol.68, No.668, pp.140-145 (2002) (in Japanese).

- [1.25] <https://www.driverless.global/glossary/49-adaptive-cruise-control>
- [1.26] Paromtchik, I. and Laugier, C., “Motion Generation and Control for Parking an Autonomous Vehicle.” at Proceedings of the IEEE International Conference on Robotics and Automation (2015).
- [1.27] Kanarachos, S.A., “A New Method for Computing Optimal Obstacle Avoidance Steering Manoeuvres of Vehicles.” *Int. J. of Vehicle Autonomous Systems*, Vol.7, No.1/2, pp.73-95 (2009).
- [1.28] Yamashita, M., Gotoh, M., Takahashi T., and Sawairi Y., “Axial Crush of Strengthening Structural Members with Various Hat-Shaped Cross-Sections (1st Report, Impact Test by a Drop Hammer).” *Transactions of the Japan Society of Mechanical Engineers A*, Vol.68, No.668, pp.140-145 (2002) (in Japanese).
- [1.29] Yamashita, M., Gotoh, M., Takahashi T. and Sawairi Y., “Axial Crush of Strengthening Structural Members with Various Hat-Shaped Cross-Sections (2nd Report, Impact Test by a Drop Hammer).” *Transactions of the Japan Society of Mechanical Engineers A*, Vol.68, No.666, pp.37-42 (2002) (in Japanese).
- [1.30] Ujihashi, S., Sogo, T., Matsumoto, H. and Adachi, T., “Energy Absorption Ability of Thin-Walled Members by Crushing Under Impact Loading.” *J. Soc. Mat. Sci.*, Vol.42, No.483, pp.1427-1431 (1993) (in Japanese).
- [1.31] Kim, H.S., Ben Goichi. and Aoki, Y., “Experimental and FEM Analysis of Rectangular CFRP Tubes for Front Side Members of Automobiles under Impact Load.” *Journal of the Japan Society for Composite Materials*, Vol.34, No.2, pp.51-59 (2008) (in Japanese).
- [1.32] Hagiwara, I., “Impact Analysis by Simulation.” *Society of Automotive Engineers of Japan*, No.33-3, pp.154-157 (1979) (in Japanese).
- [1.33] Yasuki, T. “Vehicle Development Application of Crash Simulation.” *Society of Automotive Engineers of Japan*, Vol.152-4, pp.43-48 (1998) (in Japanese).
- [1.34] Yasuki, T. “Current Situation and Problems of Vehicle Crash Analysis.” at JSME conference, No.5, pp.485-486 (2000) (in Japanese).
- [1.35] Yasuki, T. and Watanabe, N. “Application of Collision Calculation in automobile development.” *Toyota Technical Review*, No.51-1, pp.54-59 (2001) (in Japanese).
- [1.36] Araki T., “Accuracy of Collision Analysis and use cases in vehicle development.” *The Japan Society for Computational Engineering and Science*, No.8-1, pp.619-621 (2003) (in Japanese).
- [1.37] Kitagawa, Y., Hagiwara, I. and Tsuda M., “Dynamic Analysis of Thin-Walled Columns with Box Section Geometry Subjected to Axial Crushing.” *Transactions of the Japan Society of Mechanical Engineers A*, Vol.57, No.537, pp.115-119 (1991) (in Japanese).
- [1.38] Hagiwara, I., Tsuda M. and Saito, T., “Dynamic Analysis of Thin-Walled Columns with Arbitrary Section Geometry Subjected to Axial Crushing.” *Transactions of the Japan Society of Mechanical Engineers A*, Vol.55, No.514, pp.1407-1415 (1988) (in Japanese).

- [1.39] Hagiwara, I., Tsuda, M. and Sato, Y., “Dynamic Analysis of Thin-walled Box Columns Subjected to Axial Crushing Using the Finite Element Method.” JSME International journal, Series I, Vol.33, No.4, pp.444-452, (1990).
- [1.40] Toi, Y., “Finite Element Crashing Analysis of Structural Components and Experimental Validations.” SAM paper No.871246 (1987).
- [1.41] Abramowicz, W., “Dynamic Axial Crashing of Square Tubes.” International Journal of Impact Engineering, Vol.2, No.2, pp.179-208 (1984).
- [1.42] Mori, K., “Analysis of Impact Energy Absorption for Tapered Cylindrical Tubes.” Transactions of society of Automotive Engineers of Japan, Vol.36, No.3, pp.91-96 (2005).
- [1.43] Yamashita, M., “Numerical Study on Impact Crushing Characteristics of Cylindrical Body with Polygonal Section.” at Proceedings of the Japanese Spring Conference for the Technology of Plasticity, pp.461-465 (2002) (in Japanese).
- [1.44] Yasui, Y., Hosomi, K. and Onitake, a., “Dynamic Energy Absorption of Various Thin-Walled Polygonal Structural Members under Impact Compressive Load.” Journal of Japan Institute of Light Metals, Vol.55, No.6, pp.252-258 (2005) (in Japanese).
- [1.45] Yasui, Y. and Fukatsu, T. “Impact Collapse Characteristics of Thin-Walled Structure Tubes for Automobile under Oblique Impact Loading.” at Proceeding of the School of Engineering of Tokai University, Vol.47, No.2, pp.109-114 (2007) (in Japanese).
- [1.46] Yasui, Y., Shigami, M. and Fukatsu, T. “Dynamic Collapse Characteristics of Thin-Walled Structural Members under Frontal and Oblique Impact Loading.” The Japan Society of Mechanical Engineers, No.854, pp.229-230 (2007) (in Japanese).
- [1.47] Yasui, Y., Imai, T. and Fukatsu, T. “Dynamic Collapse Characteristics of Straight and Tapered Polygonal Thin-Walled Structural Members under Frontal and Oblique Impact Loading.” The Japan Society of Mechanical Engineers, No.213, pp.57-58 (2006) (in Japanese).
- [1.48] Yasui, Y., Fukatsu, T. and Ishigami M., “Impact Collapse Characteristics of Rib Thin-Walled Structural Tubes under Oblique Impact Loading.” The Japan Society of Mechanical Engineers, No.1502, pp.225-226 (2007) (in Japanese).
- [1.49] Yasui, Y., Wada, S. and Imai, T., “Impact Collapse Characteristics of Thin-Walled Structural Tubes with Various Reinforce Ribs” The Japan Society of Mechanical Engineers, No.521, pp.217-218 (2005) (in Japanese).
- [1.50] Takatori O., “Analysis of Crashes Using FE Vehicle Models – Effects of Speed Dependency and Energy Absorption.” JARI Research Journal, Vol.21, No.1, pp.197-200 (1999) (in Japanese).
- [1.51] Takatori O., “Analysis of Crashes Using FE Vehicle Models – Deformation Characteristics of Tires and Their Application to Crash Simulation.” JARI Research Journal, Vol.20, No.5, pp.197-200 (1998) (in Japanese).

- [1.52] Takatori O., “Analysis of Crashes Using FE Vehicle Models – Effects of Energy Absorption by Variations of Material Properties.” JARI Research Journal, Vol.21, No.7, pp.367-370 (1999) (in Japanese).
- [1.53] Takatori O., “Analysis of Crashes Using FE Vehicle Models – Relations Between Vehicle Types and Crash Characteristics.” JARI Research Journal, Vol.22, No.1, pp.246-249 (2000) (in Japanese).
- [1.54] Kitagawa, Y., Hagiwara, I. and Torigaki T. “Development of A Sensitivity Analysis Method for Dynamic Nonlinear Problems (1st Report).” Transactions of the Japan Society of Mechanical Engineers A, Vol.57, No.542, pp.2581-2586 (1991) (in Japanese).
- [1.55] Kitagawa, Y., Hagiwara, I. and Torigaki T. “Development of A Sensitivity Analysis Method for Dynamic Nonlinear Problems (2nd Report).” Transactions of the Japan Society of Mechanical Engineers A, Vol.58, No.552, pp.1430-1437 (1992) (in Japanese).
- [1.56] Kitagawa, Y., Hagiwara, I. and Torigaki T. “Development of A Sensitivity Analysis Method for Dynamic Nonlinear Problems (3rd Report).” Transactions of the Japan Society of Mechanical Engineers A, Vol.58, No.554, pp.1817-1820 (1992) (in Japanese).
- [1.57] Obayashi, K., “Crash Safety and Optimization of Vehicles.” The Japan Society of Mechanical Engineers, No.F06(5), pp.215-216 (2006) (in Japanese).
- [1.58] Tsuganezawa, Y., Kobayashi, K. and Yuge, K. “Optimal Design of Thin Walled Steel Structures for Crashworthiness- Maximization of Energy Absorption Capability-.” Transactions of JSCES, Vol.2007, No.20070010 (2007) (in Japanese).
- [1.59] Kazuo, K. and Kohei, Y., “Optimal Design of Collision Energy Absorption Member.” at Proceedings of the Conference on Computational Engineering and Science, Vol.4, No.1, pp.511-514 (1999) (in Japanese).
- [1.60] Takahashi, N., Kodiyalam, S. and Iijima K., “Crash-NVH Multidisciplinary Design Optimization of a Car body structure.” JSME annual meeting, Vol.6, pp.5-6 (2003) (in Japanese).
- [1.61] Yamasaki, K. and Han, J., “A Study on Maximization of Dynamic Crushing Energy Absorption of Cylindrical and Square Tubular Structures.” Vol.3, pp.165-6 (1998) (in Japanese).
- [1.62] Han, J. and Yamazaki, K., “A Study on Maximization of Dynamic Crushing Energy Absorption of Square Tubes with and without Stiffener.” JSME International journal, Series I, Vol.43, No.2, pp.138-145 (2000).
- [1.63] Yamazaki, K., Han, J. and Ishikawa, H., “A Study on Maximization of Dynamic Crushing Energy Absorption of Cylindrical Shell Structures.” Transactions of the Japan Society of Mechanical Engineers A, Vol.64, No.620, pp.1077-1083 (1998) (in Japanese).
- [1.64] Han, J. and Yamazaki, K., “Maximization of the Absorbing Energy for Dynamic Crushing of Thin-Walled Curved Beam.” Transactions of the Japan Society of Mechanical Engineers A, Vol.66, No.651, pp.2001-2007 (2000) (in Japanese).

- [1.65] Han, J. and Yamazaki, K., "A Study on Maximization of Dynamic Crushing Energy Absorption of Square Tubes with and without Stiffener." Transactions of the Japan Society of Mechanical Engineers A, Vol.65, No.632, pp.887-893 (1999).
- [1.66] Yuge, K., Ejima, S. and Abe, J., "Design of Structural Members for Crashworthiness Using Three Dimensional Topology Optimization." Transactions of the Japan Society of Mechanical Engineers A, Vol.69, No.687, pp.1613-1620 (2003) (in Japanese).
- [1.67] Yuge, K., Ejima, S. and Fuji, D., "Optimal Design of Structure Members for Crash-worthiness Using Gravity Control" at Proceedings of the conference on computational engineering and science, Vol.7, No.2, pp.857-860 (2002) (in Japanese).
- [1.68] Tsuganezawa, Y., Kobayashi, K. and Yuge, K., "Optimal Design of Thin-walled Structures for Crashworthiness (second report) Optimization on Load-displacement Curves." at Proceedings of the conference on computational engineering and science, Vol.12, No.1, pp.185-188 (2007) (in Japanese).
- [1.69] Nakazato, K., Kobayashi, K. and Yuge, K., "Optimal Design of Thin-Walled Structures for Crashworthiness (Third Report) : Sizing and Topology Optimization." at Proceedings of the conference on computational engineering and science, Vol.13, No.1, pp.201-204 (2008) (in Japanese).
- [1.70] Kashiwamura T., Mori, T., Shiratori, M., Yu, Q. and Maruyama, O., "Optimum Design of Frame Column Subjected to Axial Crushing by Statistical Optimization Method." Transactions of the Japan Society of Mechanical Engineers A, Vol.62, No.603, pp.2422-2427 (1996) (in Japanese).
- [1.71] Kashiwamura, T., Shiratori, M., Yu, Q. and Kohda, I., "Structural Optimization Using the Design of Experiments and Mathematical Programming." Transactions of the Japan Society of Mechanical Engineers A, Vol.62, No.601, pp.2180-2185 (1996) (in Japanese).
- [1.72] Yu, Q., Shiratori, M., Yajima, H. and Yoshimoto, T., "Approach to System Optimum Design by Statistical Design Support System (SDSS)." at Proceedings of the conference on computational engineering and science, Vol.4, No.1, pp.551-554 (1999) (in Japanese).
- [1.73] Yu, Q., Nozaki, A., Kashiwamura, T. and Shiraori, M., "Robust Optimum Design by Statistical Design Support System." Transactions of the Japan Society of Mechanical Engineers A, Vol.66, No.650, pp.1827-1833 (2000) (in Japanese).
- [1.74] Shiratori, M., Yu, Q., Yajima, H., "Integrated Optimal Design Using Statistical Design Support System." at Proceedings of the conference on computational engineering and science, Vol.6, No.1, pp.51-54 (2001) (in Japanese).
- [1.75] Yu, Q., Yajima, H., Yoshimoto, T., Shiratori, M. and Motoyama, K., "Multi Objective Optimization of Reinforced Members for Crash Safety Design of Automobiles." Transactions of the Japan Society of Mechanical Engineers A, Vol.66, No.641, pp.1-6 (2000) (in Japanese).

- [1.76] Yu, Q., Fujinuma, S., Yajima, H. and Shiratori, M., “Buckling Mode Controlled Design for Side Member in car-to-car Frontal Crash.” at Proceedings of the annual meeting of JSME/ MMD, pp.693-694 (2000) (in Japanese).
- [1.77] Yu, Q., Ando, T., Yajima, H. and Shiratori, M., “Shape Optimization of Side Members according to Offset Crash Situation.” The Computational Mechanics Conference, No.13, pp.515-516 (2000) (in Japanese).
- [1.78] Yu, Q., Ando, T., Yajima, H. and Shiratori, M., “Shape Optimization of Reinforced Members by Mode Controlled Approaching.” at Proceedings of the conference on computational engineering and science, Vol.6, No.2, pp.669-672 (2001) (in Japanese).
- [1.79] Yu, Q., Koizumi, N., Yajima, H. and Shiratori, M., “Optimization of Vehicle Structure and Occupant Restraint System by Multilevel Approach.” at Proceedings of the conference on computational engineering and science, Vol.6, No.2, pp.665-668 (2001) (in Japanese).
- [1.80] Hagiwara, I., Masuda, T. and Kitagawa, Y., “Method of Determining Positions of Beads.” Japanese Patent No. 5048345 (1991) (in Japanese).
- [1.81] Nojima, T., “Modelling of Folding Patterns in Flat Membranes and Cylinders by Using Origami.” Transactions of the Japan Society of Mechanical Engineers C, Vol.66, No.643, pp.1050-1056 (2000) (in Japanese).
- [1.82] Nojima, T., “Analytical Modeling of Origami and Its Applications: Mainly for Engineering Applications.” The Japan Society for Industrial and Applied Mathematics, Vol.18, No.4, pp.271-284 (2008) (in Japanese).
- [1.83] Hagiwara, I., Yamamoto, C., Tao, X. and Nojima, T., “Optimization for Crush Characteristics of Cylindrical Origami Structure Using Reversed Spiral Model.” Transactions of the Japan Society of Mechanical Engineers A, Vol.70, No.689, pp.36-42 (2004) (in Japanese).
- [1.84] Hagiwara, I. and Nadayoshi, S., “Folding Process of Cylindrical Structures Using Origami Model.” International Journal of Automotive Engineering, Vol.34, No.4, pp.145-149 (2003) (in Japanese).
- [1.85] Hagiwara, I., Wu, Z., Tao, X. and Yamamoto, C., “Optimization for Crush Characteristics of Origami Structure.” OPTIS, Vol.4, pp.285-290 (2004) (in Japanese).
- [1.86] Oku, I. and Hagiwara, I., “Improvement in Crashworthiness of Origami Structure in case of Oblique Offset Impact.” Dynamics & Design Conference 2005, Vol.5, No.15, pp.361-365 (2005).
- [1.87] Zhao, X., Hu, Y. and Hagiwara, I., “Optimal Design for Crash Characteristics of Cylindrical Thin-walled Structure Using Origami Engineering.” Transactions of the Japan Society of Mechanical Engineers A, Vol.76, No.761, pp.10-17 (2010) (in Japanese).
- [1.88] Zhao, X., Hu, Y. and Hagiwara, I., “Robust Optimization of Energy Absorption Ability with Variance of Crash.” Journal of Computational Science and Technology, Vol.76, No.767, pp.868-875 (2010) (in Japanese).

[1.89] Zhao, X., Hu, Y. and Hagiwara, I., “Shape Optimization to Improve Energy Absorption Ability of Cylindrical Thin-walled Origami Structure.” *Journal of Computational Science and Technology*, Vol.5, No.3, pp.148-162 (2011).

[1.90] Wu, Z., Hagiwara, I. and Tao, X., “Optimization of Crush Characteristics of the Cylindrical Origami Structure.” *Int. J. Vehicle Design*, Vol.43, Nos.1-4, pp.66-81 (2007).

Chapter 2

[2.1] Shibukawa, T., “Weight reduction and miniaturization technology for green politics.” *Journal of the Japan Society of Mechanical Engineers*, Vol.112, No.1088, pp.535-563 (2009).

[2.2] Noor, A., Burton, W. S., and Bert, C. W., “Computational models for sandwich panels and shells.” *The American Society of Mechanical Engineers, Rev.*, 49(3), pp.155–199 (1996).

[2.3] Kaman, M., Solmaz, M., and Turan, K.. “Experimental and Numerical Analysis of Critical Buckling Load of Honeycomb Sandwich Panels.” *Journal of composite materials*, Vol.44, No.24, pp.2819-2831(2010).

[2.4] Qiao, P., and Wang, J., “Mechanics of Composite Sinusoidal Honeycomb Cores.” *Journal of Aerospace Engineering*, pp.42-50 (2005).

[2.5] Nilsson, E. and Nilsson, A.C.. “Prediction and Measurement of Some Dynamic Properties of Sandwich Structures with Honeycomb and Foam Cores.” *Journal of Sound and Vibration*, Vol.251, Issue 3, pp.409-430 (2001).

[2.6] Saito, K., and Nojima, T., “Development of Light-Weight Rigid Core Panels, *Journal of Solid Mechanics and Materials Engineering*.” Vol.1, No.9, pp.1097-1104 (2007).

[2.7] Nojima, T. and Hagiwara, I., “Mathematics of origami and its application.” Tokyo:Kyoritsu Shuppan, 2012.

[2.8] Nojima, T., “Panel and its manufacturing method.” Japanese Patent (2005-209031).

[2.9] Nojima, T., and Saito, K., “Plate and piece of plate.” Japanese Patent (2005-245045).

[2.10] Nojima, T., “Origami model for folding method of plate and cylinder.” *Transactions of the Japan Society of Mechanical Engineers C*, Vol.66, No.643, pp.1050-1056 (2000).

[2.11] Saito, K., Nojima, T., and Hagiwara, I., “Relation between geometrical patterns and mechanical properties in newly developed light-weight core panels.” *Transactions of the Japan Society of Mechanical Engineers A*, Vol.74, No.748, pp1580-1586 (2008).

[2.12] Tokura, S. and Hagiwara, I., “Forming process simulation of truss core panel.” *Transactions of the Japan Society of Mechanical Engineers A*, Vol.74, No.746, pp81-87 (2008).

[2.13] Tokura, S. and Hagiwara, I.. “Shape optimization to improve impact energy absorption ability of

truss core panel.” Transactions of the Japan Society of Mechanical Engineers A, Vol.76, No.765, pp564-572 (2010).

[2.14] LSDYNA KEYWORD USER'S MANUAL, 2007.

[2.15] Zhao, X., “Development of simple optimization system by using response surface method.” Proceedings of the conference on computational engineering and science, Vol.13, No.1, pp.101-104 (2008).

Chapter 3

[3.1] Miura K., Tachi T., “Synthesis of rigid-foldable cylindrical polyhedra.” in ISIS-Symmetry (International Society for the Interdisciplinary Study of Symmetry). Symmetry: Artand Science, pp.204-213 (2010).

[3.2] Tachi T., “One-DOF cylindrical deployable structures with rigid quadrilateral panels”, in IASS 2009, pp.2295-2305 (2010).

[3.3] Yasuda H., Yein T., Tachi T., “Folding behavior of Tachi-Miura polyhedron bellows.” Proceedings of the Royal Society A: Mathematical, Physical and Engineering Sciences, No.469, 20130351 (2013).

[3.4] Nojima T., “3D origami for monozukuri -- proposal of pairing origami.” Folding Model Creation Series, pp.33-35 (2015).

[3.5] Nojima T., “Formation of origami structure by rigid origami modeling and related problems.” Dynamics and Design Conference: D&D 2011. The Japan Society of Mechanical Engineers, No.41(2011).

[3.6] Tachi T., “Design method of rigid origami based on quadrilateral mesh.” Japan Society for Simulation Technology 2010, pp.24-29(2010).

[3.7] Miura K., Tachi T., “Foldable cylinder, the potential concept for actuators and bellows.” Dynamics and Design Conference: D&D 2011, The Japan Society of Mechanical Engineers, pp.11-16 (2011).

[3.8] Miura K., Tachi T., “Foldable cylinder, the potential concept for actuators and bellows.” Dynamics and Design Conference: D&D 2011, The Japan Society of Mechanical Engineers, pp.3-8 (2011).

[3.9] Yang Y., Zhao X., Tokura S., Hagiwara I., “Crash energy absorption improvement of lightweight structure by using truss core panel.” Transactions of the JSME, Vol.80, No.815, SMM0191 (2014).

[3.10] Zhao X., “Development of simple optimization system by using response surface method.” Proceedings of the Conference on Computational Engineering and science, Vol.13, No.1, pp.101-104 (2008).

[3.11] Hagiwara I., “Crash analysis by simulation.” Journal of Automotive Engineering, Vol.33, No.3, pp.154-159 (1979).

[3.12] Yang Y., Savchenko M., Nara C., Hagiwara I., “Investigation for industrialization of the Nojima’s pairing origami structure.” Proceedings of the ASME 2016 International Design Engineering Technical Conferences & Computers and Information in Engineering Conference, (2016).

[3.13] Kitagawa Y., Hagiwara I., Tsuda M., “Dynamic analysis of thin-walled columns with arbitrary section geometry subjected to axial crushing.” The Japan Society of Mechanical Engineers, Vol.57; No.537, pp.115-119 (1991).

[3.14] Nguyen N., Terada K., Tokura S., Hagiwara I., “Development of origami forming to improve the flexibility of truss core panel design.” Transactions of the JSME, Vol.80, No.819, SMM3014 (2014).

Chapter 4

[4.1] TOYO SAFETY. Inc., “Folding helmet.” Japanese Patent No.2012-34287 (2012) (in Japanese).

[4.2] TOYO SAFETY. Inc., “Folding helmet.” Japanese Patent No.2014-44497 (2014) (in Japanese).

[4.3] DIC PLASTICS Inc., “Folding helmet.” Japanese Patent No.2013-116316 (2013) (in Japanese).

[4.4] Hagiwara, I. and Nara, C., “Folding structure reference number: 2015-P14.” Japanese Patent No.2015-245594 (2015).

[4.5] Hagiwara, I., Nara, C. and Ozawa, N., “Helmet.” Utility Model Application No. 2016-000870 (2016).

[4.6] Hagiwara, I. and Nadayoshi, S., “Folding process of cylindrical structures using origami model.” International Journal of Automotive Engineering, Vol.34, No.4 (2003), pp.145-149 (in Japanese).

[4.7] Hagiwara, I., Yamamoto, C., Tao, X. and Nojima, T., “Optimization for crush characteristics of cylindrical origami structure using reversed spiral model.” Transactions of the Japan Society of Mechanical Engineers, Series A, Vol.70, No.689 (2004), pp.36-42 (in Japanese).

[4.8] Hagiwara, I., The development of mathematical and biomimetic origami and the industrial applications, Transactions of the Japan Society of Mechanical Engineers, Vol.119, No.1175 (2016), pp.539 (in Japanese).

[4.9] Kitagawa, Y., Hagiwara, I. and Tsuda, M., “Dynamic analysis of thin-walled columns with arbitrary section geometry subjected to axial crushing.” Transactions of the Japan Society of Mechanical Engineers, Series A, Vol.57, No.537 (1991), pp.1135-1139 (in Japanese).

[4.10] Zhao, X., Hu, Y. and Hagiwara, I., “Optimal design for crash characteristics of cylindrical thin-walled structure using origami engineering.” Transactions of the Japan Society of Mechanical Engineers, Series A, Vol.76, No.761 (2010), pp.10-17 (in Japanese).

[4.11] Yang, Y., Ishida, S., Zhao, X. and Hagiwara, I., “Vehicle energy absorbers consisting of foldable cylinders using response surface methodology.” Vol.3, No.4 (2017), Int. J. Vehicle Performance, pp.380-394.

- [4.12] Nara, C., “Continuous flattening of some pyramids.” *Element der Mathematic*, No.69 (2014), pp.45-56.
- [4.13] Itoh, J., Nara, C., “Continuous flattening of platonic polyhedra. . In: Akiyana, J., Bao, J., Kano, M., Tan, X. (eds.) *Computational Geometry.*” *Graphs and Applications. Lecture Notes in Computer Science*, vol.7033(2011), pp.108–121.
- [4.14] Demaine, E. D., Demaine, M. L., Itoh, J. and Nara, C., *Continuous flattening of orthogonal polyhedra*, LNCS, Springer International Publishing AG 2016 (2016).
- [4.15] Nojima, T., *Modelling of folding patterns in flat membranes and cylinders by using origami*, *Transactions of the Japan Society of Mechanical Engineers, Series C*, Vol.66, No.643 (2000), pp.1050-1056 (in Japanese).
- [4.16] Saito, K., Pellegrino, S. and Nojima, T., “Manufacture of arbitrary cross-section honeycomb cores based on origami techniques.” *ASME Journal of Mechanical Design*, Vol.136, No.051011(2014).
- [4.17] Zhao, X., Hu, Y. and Hagiwara, I., “Robust optimization of energy absorption ability with variance of crash, *Journal of Computational Science and Technology.*” Vol.76, No.767 (2010), pp.868-875(in Japanese).
- [4.18] Zhao, X., Hu, Y. and Hagiwara, I., “Shape optimization to improve energy absorption ability of cylindrical thin-walled origami structure.” *Journal of Computational Science and Technology*, Vol.5, No.3 (2011), pp.148-162.
- [4.19] Wu, Z., Hagiwara, I. and Tao, X., “Optimization of crush characteristics of the cylindrical origami structure.” *Int. J. Vehicle Design*, Vol.43, Nos.1-4 (2007), pp.66-81.

Chapter 5

- [5.1]
https://web.archive.org/web/20170903105244/https://www.sae.org/misc/pdfs/automated_driving.pdf
- [5.2] http://www.who.int/violence_injury_prevention/road_safety_status/2015/en/. Global status report on road safety 2015.
- [5.3] Hinton, G. and Osindero, S., “A Fast Learning Algorithm for Deep Belief Net.” *Neural Computation*, No.18, pp.1527-1554 (2006).
- [5.4] Haykin, S., “*Neural Networks: A Comprehensive Foundation.*” 2nded New York (1999).
- [5.5] Bengio, Y., “Learning Deep Architectures for AI.” *Foundations and Trends Machine Learning.*” Vol.2, No.1, pp.1-127 (2009).
- [5.6] Karpathy, A., “Convolutional Neural Networks: Architectures, Convolution / Pooling Layers.” Notes for CS231n Convolutional Neural Networks for Visual Recognition, Stanford University. <http://cs231n.github.io/convolutional-networks/>.

- [5.7] Hinton, G., Salakhutdinov, RR. "Reducing the Dimensionality of Data with Neural Networks." *Science*, Vol.313, No.5786, pp.504-507 (2006).
- [5.8] Bengio, Y., Lamblin, P., and Popovici, D. "Greedy Layer-wise Training of Deep Networks." at *Proceedings of the 2007 Advances in Neural Information Processing Systems*, pp.153-160 (2007).
- [5.9] Ranzato, M., Poultney, C. and Chopra, S., "Efficient Learning of Sparse Representations with An Energy-based Model." at *Proceedings of the 2007 Advances in Neural Information Processing Systems*, pp.1137-1144 (2007).
- [5.10] Erhan, D., Bengio, Y. and Courville, A., "Why Does Unsupervised Pre-training Help Deep Learning." *Journal of Machine Learning Research*, Vol.11, No.3, pp.625-660 (2010).
- [5.11] LeCun, Y., Bengio, Y. and Hinton, G., "Deep learning." *Nature*, Vol.521, No.7553, pp.436-444 (2015).
- [5.12] Lawrence, S., Giles, C. and Tsoi, A., "Face Recognition: A Convolutional Neural-network Approach." *IEEE Transactions on Neural Networks*, Vol.8, No.1, pp.98-113 (1997).
- [5.13] Neubauer, C., "Evaluation of Convolutional Neural Networks for Visual Recognition." *IEEE Transactions on Neural Networks*, Vol.9, No.4, pp.685-696 (1998).
- [5.14] Taigman, Y., Yang, M. and Ranzato, M., "DeepFace: Closing the Gap to Human-level Performance in Face Verification." at *Proceedings of the IEEE Conference on Computer Vision and Pattern Recognition (CVPR)*, pp.1701-1708 (2014).
- [5.15] Schroff, F., Kalenichenko, D. and Philbin, J., "FaceNet: A Unified Embedding for Face Recognition and Clustering." at *Proceedings of the IEEE Conference on Computer Vision and Pattern Recognition (CVPR)*, pp.815-823 (2015)
- [5.15] Abdel-Hamid, O., Mohamed, A. and Jiang, H., "Applying Convolutional Neural Networks Concepts to Hybrid NN-HMM Model for Speech Recognition." at *Proceedings of the IEEE International Conference on Acoustics, Speech and Signal Processing (ICASSP)*, pp.4277-4280 (2012).
- [5.16] Abdel-Hamid, O., Mohamed, A. and Jiang, H., "Convolutional Neural Networks for Speech Recognition." *IEEE/A CM Transactions on Audio, Speech, and Language Processing*, Vol.22, No.10, pp.1533-1545 (2014).
- [5.17] Kadi, I., Idri, A., J.L. Fernandez-Aleman, "Knowledge Discovery in Cardiology: A Systematic Literature Review." *International Journal of Medical Informatics*, No.97, pp.12-32 (2017).
- [5.18] Xu, J., Wang, P. and Tian, G., "Short Text Clustering via Convolutional Neural Networks." at *Proceedings of NAACL-HLT 2015*, pp.62-69 (2015).
- [5.19] Gao, J., Yang, X. and Zhang, T., "Robust Visual Tracking Method via Deep Learning." *Chinese Journal of Computers*, Vol.39, No.7, pp.1419-1434 (2016) (in Chinese).
- [5.20] Li, H., Liu, F. and Yang, S., "Remote Sensing Image Fusion based on Deep Support Value Learning Networks." *Chinese Journal of Computers*, Vol.39, No.8, pp.1583-1596 (2016) (in Chinese)

- [5.21] Diago, L., Kitaoka, T. and Hagiwara, I., “Development of A System for Automatic Facial Expression Analysis.” *Journal of Computational Science and Technology*, Vol.2, No.4, pp.401-412 (2008).
- [5.22] <https://developer.nvidia.com/digits>
- [5.23] Allison, G., “Digits Deep Learning GPU Training System. “
http://www.nvidia.com/content/events/geoInt2015/AGrey_Intro_DIGITS_GEOINT2015.pdf
- [5.24] Krizhevsky, A., Sutskever, I. and Hinton, G., “ImageNet Classification with Deep Convolutional Neural Networks.” at *Proceedings of Advances in Neural Information Processing Systems*, pp.1097-1105 (2012).
- [5.25] Christian, S., Liu, W. and Jia, Y., “Going Deeper with Convolutions.” at *Proceedings of the IEEE Conference on Computer Vision and Pattern Recognition (CVPR)*, pp.1-9 (2015).
- [5.26] Ekman, P. and Friesen, W. V. “Unmasking the Face. A guide to Recognizing Emotions from Facial Clues.” Palo Alto: Consulting Psychologists Press (1975).

Chapter 6

- [6.1] Fábio A.O. Fernandes and R.J. Alves de Sousa, “Finite Element Analysis of Helmeted Oblique Impacts and Head Injury Evaluation with A Commercial Road Helmet.” *Structural Engineering and Mechanics*, Vol.48, No.5, pp.661-679 (2013).
- [6.2] Kanade, T., Cohn, J. and Tian, Y., “Comprehensive Database for Facial Expression Analysis.” at *Proceedings of the International Conference on Automatic Face and Gesture Recognition*, pp.46–53, (2000).
- [6.3] Lucey, P., Cohn, J.F., Kanade, T., Saragih, J., Ambadar, Z. and Matthews, I., “The Extended Cohn-Kanade Dataset (CK+): A Complete Dataset for Action Unit and Emotion-Specified Expression.” In *Computer Vision and Pattern Recognition Workshop on Human-Communicative Behavior* (2010).
- [6.4] Kanbayashi, T., et al, “Examination of Correction Method to Shadow in Face Image for Iyashi Expression Recognition System.” *IIEEJ*, Vol.41, No.1 pp.28-35 (2012).
- [6.5] Diago, LA., Kitaoka, T., and Hagiwara, I., “Neuro-Fuzzy Quantification of Personal Perceptions of Facial Images based on a Limited Data Set.” *IEEE Transactions on Neural Networks* 2011.